

AD-A061 056

HUGHES RESEARCH LABS MALIBU CALIF
COMPONENTS FOR SINGLE-STRAND MULTIMODE FIBER SYSTEMS.(U)
AUG 78 M K BARNOSKI, B U CHEN, H R FRIEDRICH

F/G 20/6

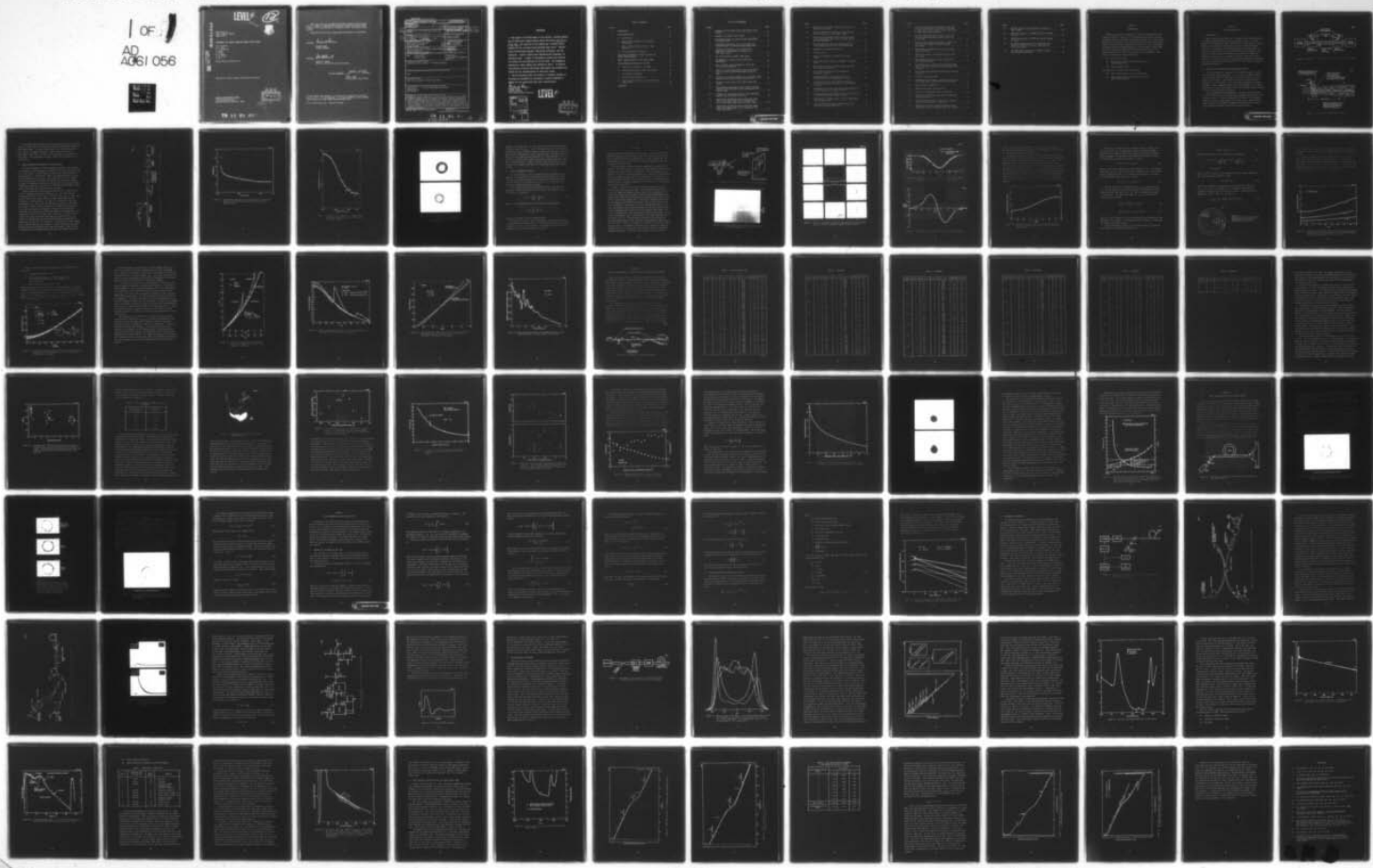
F19628-77-C-0103

UNCLASSIFIED

RADC-TR-78-179

NL

1 OF 1
AD
A061 056



LEVEL III

A047315

12 SC



AD A061056

RADC-TR-78-179
Final Technical Report
August 1978

COMPONENTS FOR SINGLE-STRAND MULTIMODE FIBER SYSTEMS

- M. K. Barnoski
- B. U. Chen
- H. R. Friedrich
- S. Jensen
- E. Marom
- O. G. Ramer
- M. D. Rourke
- H. Yen

Hughes Research Laboratories

DDC FILE COPY

Approved for public release; distribution unlimited.

ROME AIR DEVELOPMENT CENTER
Air Force Systems Command
Griffiss Air Force Base, New York 13441

DDC
RECEIVED
NOV 13 1978
RECEIVED

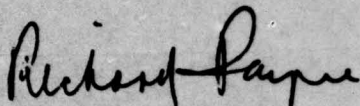
[Handwritten signature]
D

78 11 01 080

This report has been reviewed by the RADC Information Office (OI) and is releasable to the National Technical Information Service (NTIS). At NTIS it will be releasable to the general public, including foreign nations.

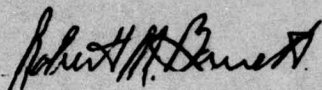
RADC-TR-78-179 has been reviewed and is approved for publication.

APPROVED:



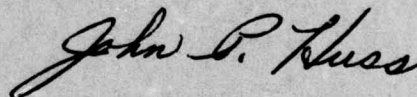
RICHARD PAYNE
Project Engineer

APPROVED:



ROBERT M. BARRETT
Director, Solid State Sciences Division

FOR THE COMMANDER:



JOHN P. HUSS
Acting Chief, Plans Office

If your address has changed or if you wish to be removed from the RADC mailing list, or if the addressee is no longer employed by your organization, please notify RADC (ESO) Hanscom AFB MA 01730.

Do not return this copy. Retain or destroy.

UNCLASSIFIED

SECURITY CLASSIFICATION OF THIS PAGE (When Data Entered)

18 19 REPORT DOCUMENTATION PAGE		READ INSTRUCTIONS BEFORE COMPLETING FORM	
1. REPORT NUMBER RADC TR-78-179		2. GOVT ACCESSION NO.	3. RECIPIENT'S CATALOG NUMBER N/A
4. TITLE (and Subtitle) COMPONENTS FOR SINGLE-STRAND MULTIMODE FIBER SYSTEMS		5. TYPE OF REPORT & PERIOD COVERED Final Technical Report, 4 Jan 77 - 31 Mar 78	
7. AUTHOR(s) M. K. Barnoski, S. Jensen, M. D. Rourke B. U. Chen, E. Marom, H. Yen H. R. Friedrich, O. G. Ramer		6. CONTRACT OR GRANT NUMBER(s) F19628-77-C-0103	
8. PERFORMING ORGANIZATION NAME AND ADDRESS Hughes Research Laboratories 3011 Malibu Canyon Road Malibu CA 90265		10. PROGRAM ELEMENT, PROJECT, TASK AREA & WORK UNIT NUMBERS 61102F 23060221	
11. CONTROLLING OFFICE NAME AND ADDRESS Deputy for Electronic Technology (RADC/ESO) Hanscom AFB MA 01731 Monitor/Richard Payne/ESO		12. REPORT DATE August 1978	
14. MONITORING AGENCY NAME & ADDRESS (if different from Controlling Office) Same		13. NUMBER OF PAGES 99	
		15. SECURITY CLASS. (of this report) UNCLASSIFIED	
		15a. DECLASSIFICATION/DOWNGRADING SCHEDULE N/A	
16. DISTRIBUTION STATEMENT (of this Report) Approved for public release; distribution unlimited.			
17. DISTRIBUTION STATEMENT (of the abstract entered in Block 20, if different from Report) Same			
18. SUPPLEMENTARY NOTES RADC Project Engineer: Richard Payne (ESO)			
19. KEY WORDS (Continue on reverse side if necessary and identify by block number) Fiber Optics Optical Time Domain Reflectometer Access Couplers Mode Mixing			
20. ABSTRACT (Continue on reverse side if necessary and identify by block number) During this program, "Components for Single Strand Multimode Fiber Systems" (F19628-77-C-0103), we (1) investigated input-output coupling techniques capable of providing full duplex operation on a single strand, multimode fiber waveguide; (2) used the optical time domain reflectometer (OTDR) to determine fiber attenuation characteristics; (3) investigated the steady-state mode-mixing phenomena of a 4-km length of graded-index fiber; (4) improved the OTDR; and (5) developed low-insertion-loss bi-directional access couplers for multimode fiber waveguides.			

6

10

9

15

16

11

12 97p.

Jan 77 - 31 Mar 78

17 J2

DD FORM 1 JAN 73 1473

EDITION OF 1 NOV 65 IS OBSOLETE

UNCLASSIFIED

SECURITY CLASSIFICATION OF THIS PAGE (When Data Entered)

78 11 01 080 LB
172 600

EVALUATION

1. This report is the Final Report on the contract, covering research done on fiber optic coupling devices during the period 4 Jan 1977 to 31 Mar 1978. The objective of the research was to develop access couplers for use in single-strand multimode fiber optics. Specific tasks involved design approach, fabrication techniques, test and evaluation. Access T couplers were fabricated with acceptably low insertion losses. A number of experimental couplers were supplied for further test and evaluation by the Air Force. The propagation properties of taper couplers were examined in detail. In addition, the technique of optical time-domain reflectometry was developed and refined for the characterization of fiber optic cables.
2. The work performed under this contract is extremely valuable in providing the groundwork for development of passive compounds in general for use in multimode fiber optic communications.

Richard Payne
RICHARD PAYNE,
Contract Monitor
Solid State Sciences Division

LEVEL II

ACCESSION for	
NTIS	Write Section <input checked="" type="checkbox"/>
DDC	Diff Section <input type="checkbox"/>
ANNOUNCED	<input type="checkbox"/>
JUSTIFICATION.....	
BY.....	
DISTRIBUTION/AVAILABILITY CODES	
SPEC. AVAIL. ORG./W/ SPECIAL	
A	

DDC
RECEIVED
NOV 13 1978
RECEIVED
D

TABLE OF CONTENTS

Section		Page
1	INTRODUCTION	9
2	TAPER COUPLER STUDY	11
	A. Introduction	11
	B. Prism Coupler Technique for Launching Mode Groups	11
	C. Modal Transmission Properties of Taper Couplers	13
	D. Taper Measurement Techniques	18
3	STUDY AND DEVELOPMENT OF ACCESS COUPLERS FOR SINGLE STRAND SYSTEMS	33
4	MODAL CHARACTERISTICS OF STEP INDEX FIBERS	53
5	FIBER PARAMETER STUDIES WITH THE OTDR	59
	A. Theoretical Treatment of the OTDR	59
	B. Detected Backscattered Power Calculations	63
	C. Experimental Techniques	66
	D. Backscattering Experiments	75
	E. Fiber Parameter Studies on the 4-km Graded- Index Fiber	88
	REFERENCES	97

LIST OF ILLUSTRATIONS

Figure		Page
1	Schematic of full duplex link using tapered fiber couplers	12
2	Schematic of tapered fiber coupler	12
3	Experimental setup for insertion-loss measurement of tapered fibers	14
4	Transmission efficiency of a taper coupler for different modes in a multimode step-index fiber	15
5	Transmission efficiency of a tapered fiber immersed in diiodemethane as a function of fiber modal index	16
6	Far field pattern of higher order modes	17
7	Arrangement for tapered filter diffraction measurements	20
8	View of tapered fiber displayed on the screen of an optical comparator	20
9	View of the diffraction pattern and the deflected beam for various illuminated regions along the taper	21
10	Variation of the fiber diameter in the tapered region measured from diffraction and refraction data	22
11	Variation of the slope of the taper along fiber length	22
12	Experimentally determined lateral deflection angle versus the azimuth angle of the outgoing beam for a tapered fiber	23
13	Schematic of the normalized fiber shell dimensions and the ray definitions of the text	25
14	Analytically determined lateral deflection angle versus the azimuth angle of the outgoing ray for a solid single index fiber and taper angles	26
15	Analytically determined lateral deflection angle versus the azimuth angle of the outgoing ray for three clad fibers	27

Figure		Page
16	Analytically determined azimuth angle versus the incident ray position	29
17	Relative geometrical intensity of the deflected beam as a function of the azimuth angle	30
18	Analytically determined lateral deflection angle versus the azimuth angle of the outgoing ray for the case indicated	31
19	Measured intensity versus the azimuth angle for a step index fiber with clad core radius ratio	32
20	Equipment for coupling evaluation	33
21	T-coupler data	41
22	Fixture for holding the lapped and polished fibers	43
23	The coupled power versus the alignment of lapped fibers	44
24	The projected trend in coupling versus lap depth with a 100 cm lap radius	45
25	The excess loss and tap ratio measured for fabricated couplers	46
26	Coupling and loss versus length of pull to establish taper for a single pair of fibers	47
27	Theoretical curve for the coupling versus the cross-sectional area reduction in a fused tapered T coupler	49
28	Photographs of the far field pattern obtained with a low loss twisted and tapered T coupler	50
29	The measured loss and coupling versus mode index for a typical twisted and tapered T coupler	52
30	Experimental arrangement used to detect mode-mixing in step-index fibers	53
31	Far-field radiation pattern observed from 1-km cabled Corning step index fiber	54

Section	Page	
32	Far field radiation pattern observed from short piece of fiber without a connector, short piece of fiber with a good connector, and a short piece of fiber with a poor connector	55
33	Far field radiation pattern observed from 1-km cabled Corning fiber with a splice connection at the input	56
34	Detected signal levels versus fiber length, loss, and probe pulse length for backscattering experiments	65
35	Experimental arrangement used to record return optical waveform	67
36	Optical time domain reflectometer using a fiber "T" coupler	68
37	OTDR assembled using an external beamsplitter and crossed polarizers	70
38	Oscillograms of the deflected backscattered light from a 4-km fiber using the external beamsplitter technique	71
39	Laser diode pulse generator employing an avalanche transistor	73
40	Collector current waveform	74
41	Experimental set-up used to investigate the effect of the mode mixer on the backscatter experiment	76
42	Modal content of CGW 491352	77
43	Backscattering data from CGW 491352	79
44	Spectral loss measurement data on CGW 491352	81
45	Backscatter data from Corning fiber G-1000 using 10-nsec-wide pulse	83
46	A semi-logarithmic plot of the detected waveform from the center section of HAC fiber	84
47	Backscatter data from a HRL developmental fiber showing the effect of wrapping fibers on a mandrel	87

Figure		Page
48	Spectral insertion loss measurement obtained on fiber G-4000	89
49	OTDR characteristic of G-4000 with pulse launched in end I	90
50	OTDR characteristic of G-4000 with pulse launched in end II	91
51	The OTDR characterizations of G-4000 made under identical conditions to ensure repeatability of the new system	94
52	Two OTDR characterizations of G-4000 resulting from different launch NAs	95

SECTION 1

INTRODUCTION

During this program, "Components for Single Strand Multimode Fiber Systems" (F19628-77-C-0103), we (1) investigated input-output coupling techniques capable of providing full duplex operation on a single strand, multimode fiber waveguide; (2) used the optical time domain reflectometer (OTDR) to determine fiber attenuation characteristics; (3) investigated the steady-state mode-mixing phenomena of a 4-km length of graded-index fiber; (4) improved the OTDR, and (5) developed low-insertion-loss bi-directional access couplers for multimode fiber waveguides. This report is divided into three major topics:

- Taper Coupler Study
- Study and Development of Access Couplers for Single-Strand Systems
- Fiber Parameter Study.

The final topic is divided into two sections:

- Modal Characteristics of Step Index Fibers
- Fiber Parameter Studies with the Optical Time Domain Reflectometer.

SECTION 2

TAPER COUPLER STUDY

A. INTRODUCTION

Taper couplers can provide input coupling for full duplex operation on a single-strand multimode fiber (see Figures 1 and 2). In this study, we investigated the modal properties of a taper coupler in transmission using a prism to launch mode groups into a multimode fiber, developed a technique for measuring the geometrical characteristics of fibers and tapered fibers, and we optimized the input coupling of taper couplers so that backscattered light was observed in the OTDR over a distance of 1.8 km in the 4-cm graded index fiber purchased on this contract. This section considers prism coupler techniques for launching mode groups, modal transmission properties of taper couplers, and taper measurement techniques.

B. PRISM COUPLER TECHNIQUE FOR LAUNCHING MODE GROUPS

The prism coupler is a powerful tool for modal studies of single-mode integrated optics structures. As a result of an IR&D effort, we have successfully used a prism coupler to excite selectively certain groups of fiber modes. The ultimate resolution of prism couplers is determined by the divergence of the input laser beam and the coupling strength. Using a commercial He-Ne laser with divergence of 1.0 mrad, we were able to excite fiber modes in 10 to 20 different groups according to their effective refractive indices.

In the prism-coupling configuration, the glass prism is pressed on an optical fiber with its cladding nearly completely polished off at the region of contact. Properly aligning the direction of the impinging radiation on the prism hypotenuse, the energy can be coupled into the fiber core when the condition of momentum conservation is satisfied. Input coupling efficiency of 10% can be readily obtained.

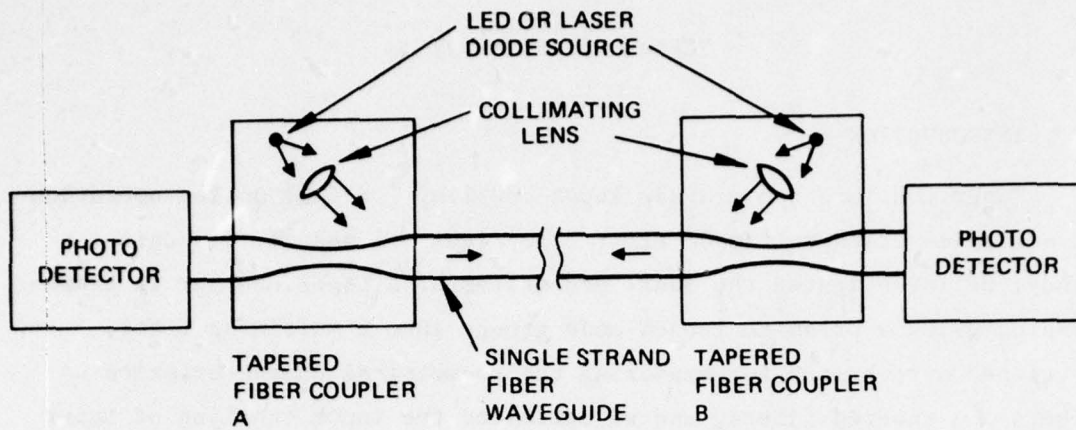


Figure 1. Schematic of full duplex link using tapered fiber couplers.

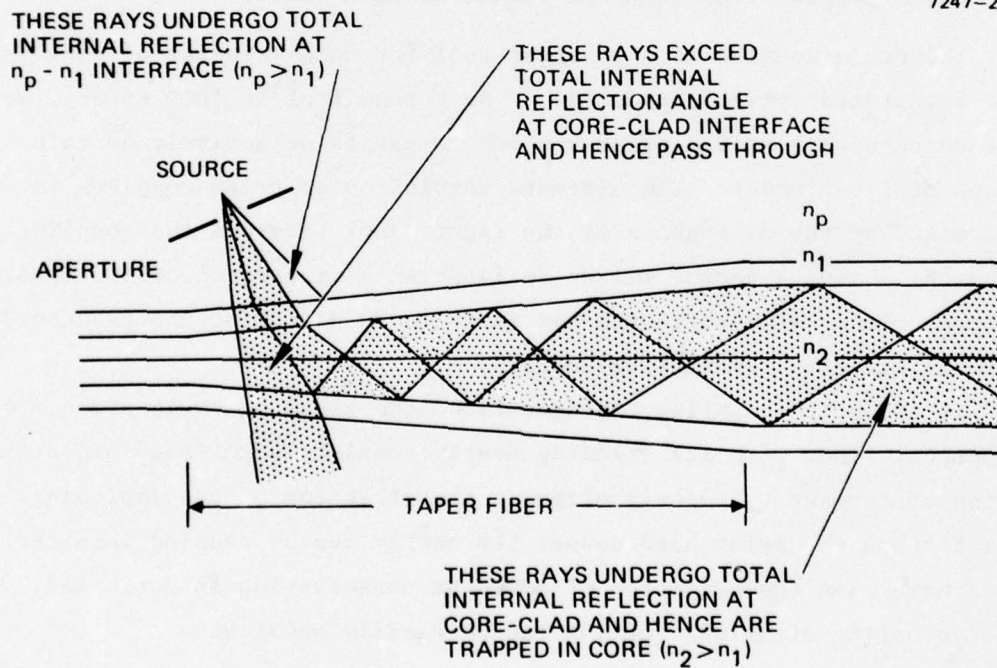


Figure 2. Schematic of tapered fiber coupler.

The work on modal properties of fibers showed that a good fiber butt coupler or splice does not introduce any serious mode mixing in identical step index fibers. By using a prism coupler on a short pigtail and a butt coupler, the modal properties of fiber components are easily measurable. The results for several such experiments are discussed in this report. The measurements on taper couplers are described in the next section.

C. MODAL TRANSMISSION PROPERTIES OF TAPER COUPLERS

The modal dependence of light transmission through a taper coupler was measured. In the experiment, a tapered optical fiber was butt coupled to a short pigtail of fiber on which a glass coupling prism had been pressed (Figure 3). When the two fibers are aligned properly, there is no mode mixing at the butt joint. The output power after the tapered section was measured as different mode groups were excited by changing the angle of incidence on the prism. The input power was measured after cleaning the fiber near the butt joint. The ratio of the output to input power is defined as the insertion loss of the taper.

Figure 4 shows the insertion loss measurement for a tapered fiber (25 mil elongation) when it was exposed to air. The insertion loss increases from about 1 dB for $n_{\text{eff}} \sim 1.47$ to 6 dB for $n_{\text{eff}} \sim 1.458$. This general behavior was expected since the higher order modes are more susceptible to radiation loss. The effect of covering the taper with diiodomethane ($n = 1.74$) is to increase the out coupling of the higher order modes. Figure 5 shows the results of insertion loss measurement for another taper with an elongation of 20 mil. The measurement was taken when the tapered fiber section was immersed in diiodomethane. The transmission efficiency for higher order modes ($n_{\text{eff}} < 1.460$) is less than 6% (-12.2 dB). The lower order modes are less affected by the presence of diiodomethane because the modal intensity distribution is peaked near the center of the fiber core. In addition, the fiber elongation is shorter than the one in Figure 4. Hence, relatively high transmission efficiency was measured for lower order modes. Figure 6 shows the output power distribution before and after the tapered section was

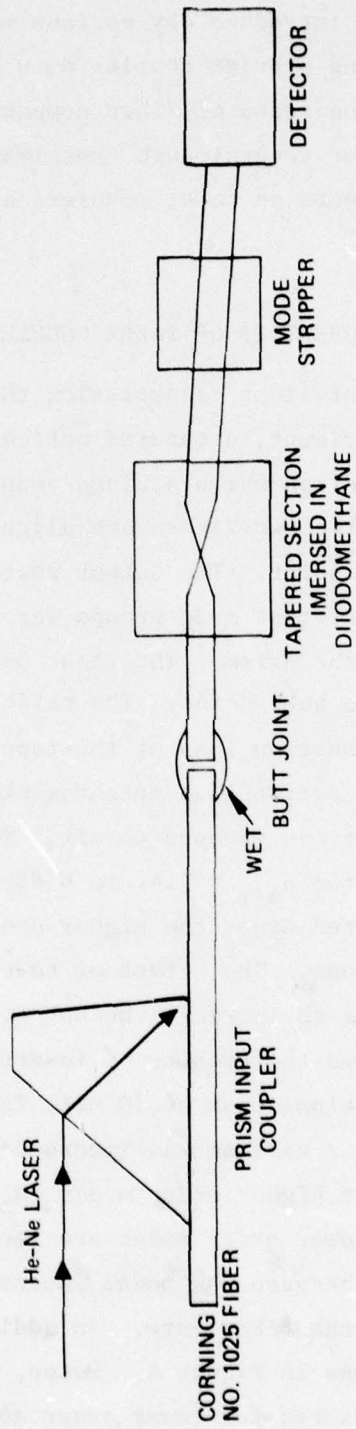


Figure 3. Experimental setup for insertion-loss measurement of tapered fibers.

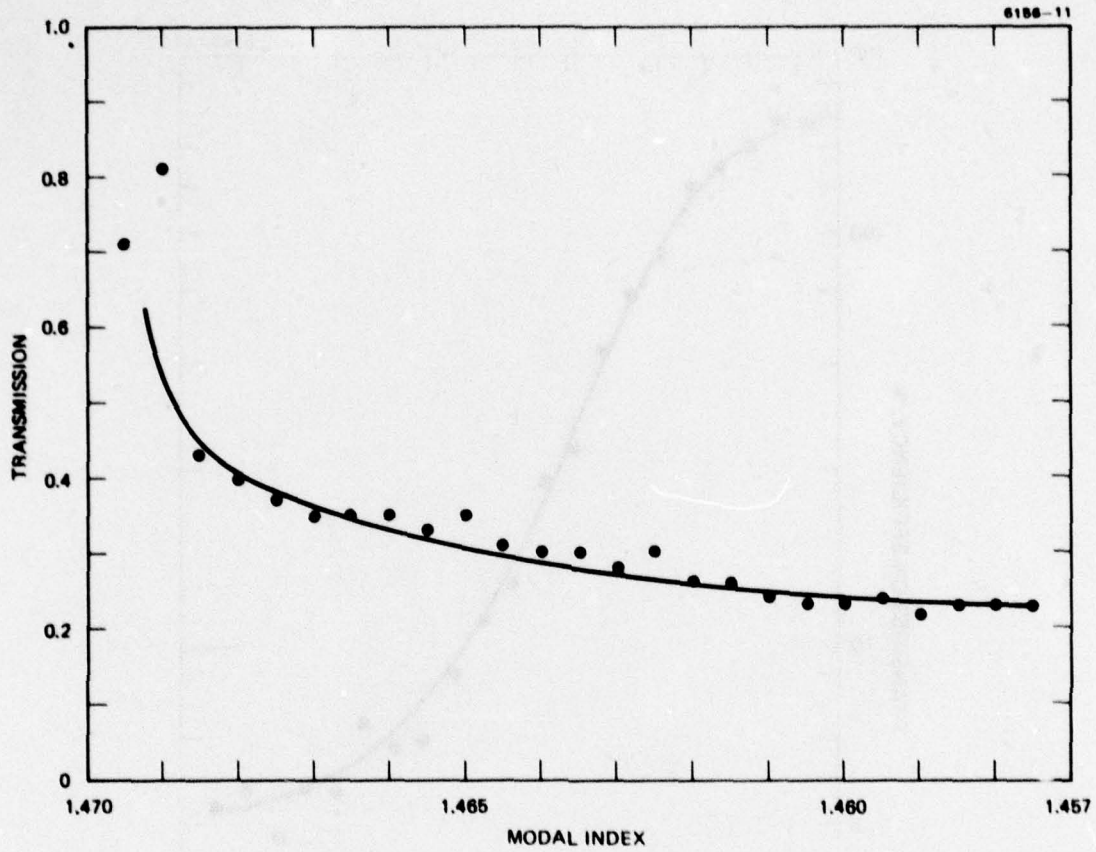


Figure 4. Transmission efficiency of a taper coupler for different modes in a multimode step-index fiber; the taper was exposed to air.

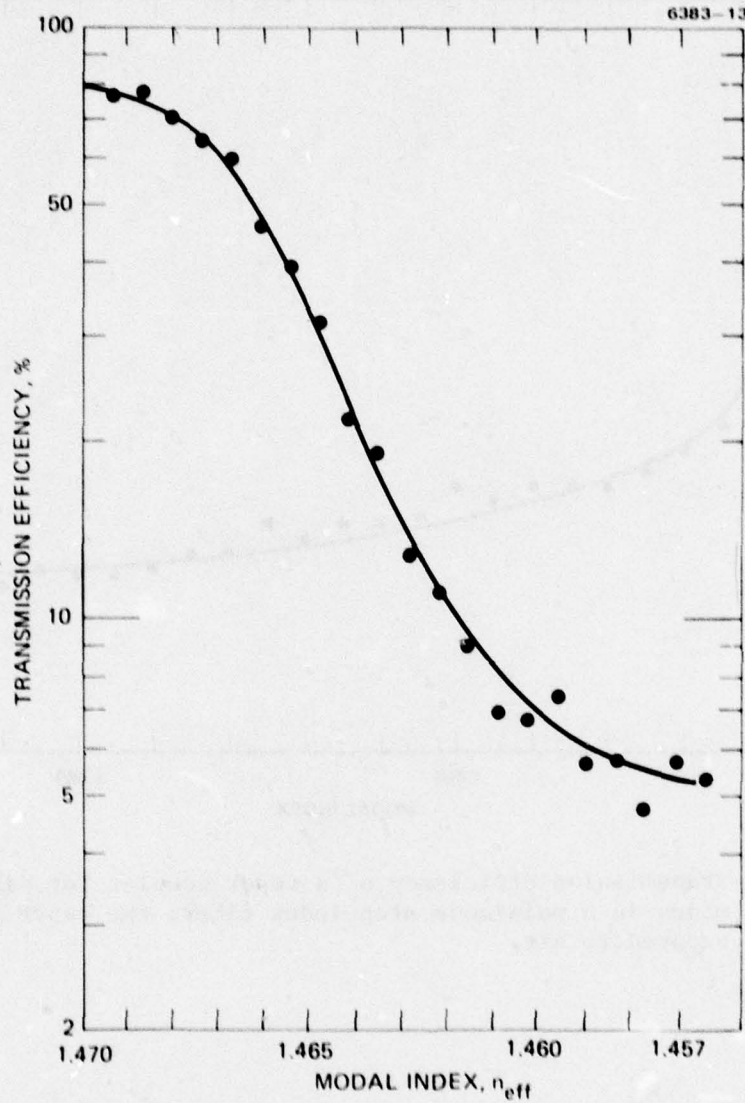


Figure 5. Transmission efficiency of a tapered fiber immersed in diiodomethane as a function of fiber modal index.

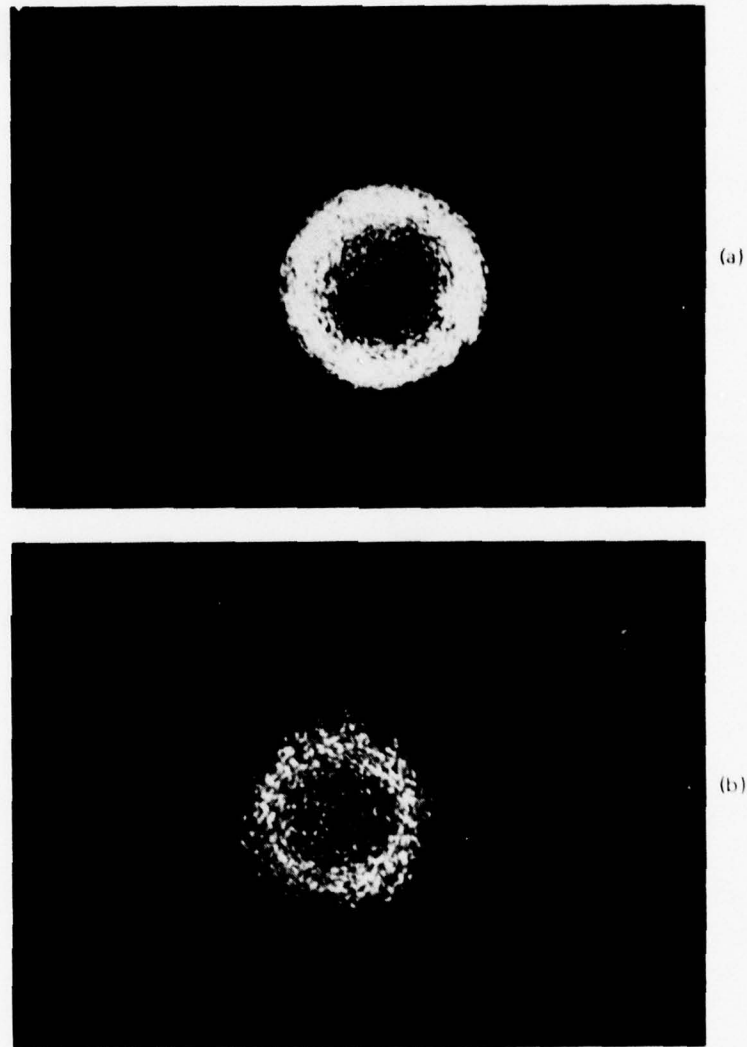


Figure 6. Far field pattern of higher order modes ($n_{\text{eff}} \approx 1.460$) when the tapered fiber was (a) exposed to air, (b) immersed in diiodomethane.

immersed in diiodomethane. The input modal distribution corresponded to a group of modes with $n_{\text{eff}} = 1.460$. When compared with the input power distribution, these far-field pictures indicate that the taper causes some mode mixing as evidenced by a wider ring structure. The ring pattern in Figure 6(a) has almost uniform intensity for a taper exposed to air; all the modes in the ring were equally attenuated. However, the ring structure in Figure 6(b) has a higher intensity around the inner edge, indicating that the higher order modes are coupled out more in the tapered section.

D. TAPER MEASUREMENT TECHNIQUES

The low-loss fiber is very transparent and is cylindrical, which makes it very difficult to accurately determine dimensions of tapered sections in the fiber with an optical microscope. During this study, a novel technique for determining the geometrical characteristics of fibers and tapered fibers was developed.

If a narrow beam of light illuminates the taper, the light that propagates through the fiber will be deflected. The paraxial angle of deflection, μ , is given by

$$\sin \mu = 2 \left(\frac{\bar{n}}{n_o} - 1 \right) \tan \alpha \quad , \quad (1)$$

where α is the taper-angle, \bar{n} is the average refractive index

$$\bar{n} = \frac{1}{2r} \int_{-r}^r n(\rho) \, d\rho \quad , \quad (2)$$

and n_o is the index of the surrounding medium.

The deflection angle μ can be determined by measuring the position of the deflected beam with respect to the diffraction pattern of the beam entrance slit. For a slit of width b , the angular position of the zeros (minima) of the diffraction pattern is given by

$$\mu = N \lambda / b \quad , \quad (3)$$

where the integer N is the order of the minima. On the other hand, the light that passes around the fiber is not deflected, and the classical case of diffraction from a rectangular stop is again encountered. The fiber diameter can be calculated from the measured minima position and the distance from the fiber.

The setup used for these diffraction measurements is sketched in Figure 7. The taper itself can be observed and measured microscopically, although with some difficulty. Figure 8 is a view of the taper as displayed on the screen of an optical comparator. Besides the inconvenience of using a large instrument such as the comparator, the accuracy of a slope measurement made from this photograph is poor. Measurement of the diameter and the subsequent computation of the slope can be reliably done only with great difficulty.

Figure 9 consists of a series of photographs taken at different points along a tapered optical fiber. One can easily determine the location of the taper as evidenced by the change in the complicated light transmission pattern observed when light traverses the undeformed fiber (Figure 9(a)) to the pattern obtained in the tapered region (Figures 9(b) through 9(e) and 9(g) through 9(j)). The point of inflexion corresponds to the maximum slope (deflection) (Figures 9(d) and 9(e)) which can be easily determined. The center of the taper (Figure 9(f)) has no curvature, and therefore the diffraction pattern is similar to that obtained from the undeformed fiber outside the taper (Figure 9(a)) scaled by the ratio of the diameters. The pattern repeats itself on the other side of center with opposite slope. Data measured on one taper have been plotted in Figures 10 and 11. The data given in Figure 10 were obtained by deflection measurements, which are directly proportional to the slope of the taper (Eq. 1); Figure 11 displays the variation of the fiber diameter along the taper. The diameter variations can be computed by numerical integration of the slope data once the outside diameter has been independently determined. The dotted line in Figure 11 was obtained by

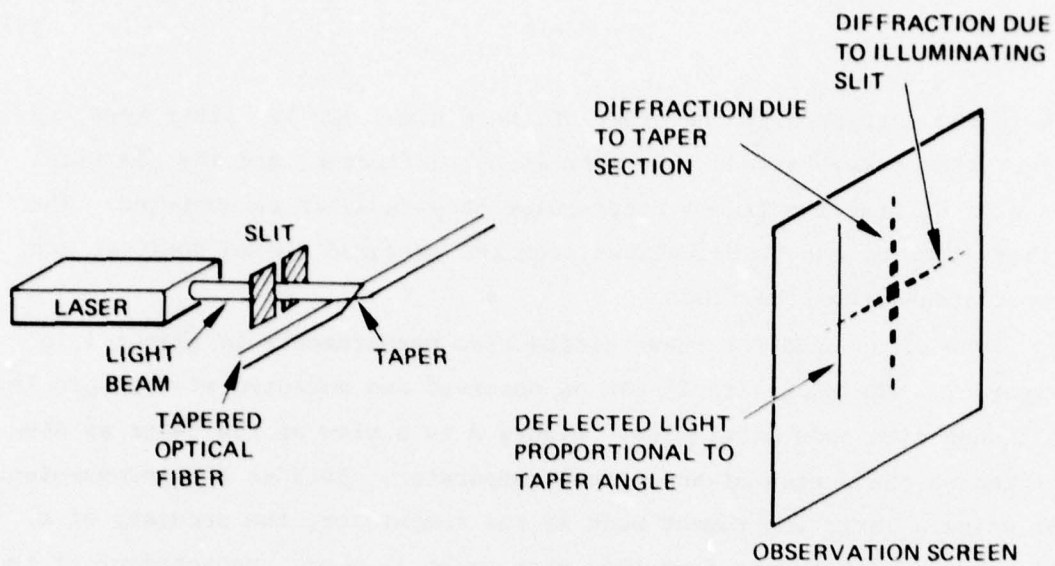


Figure 7. Arrangement for tapered filter diffraction measurements.

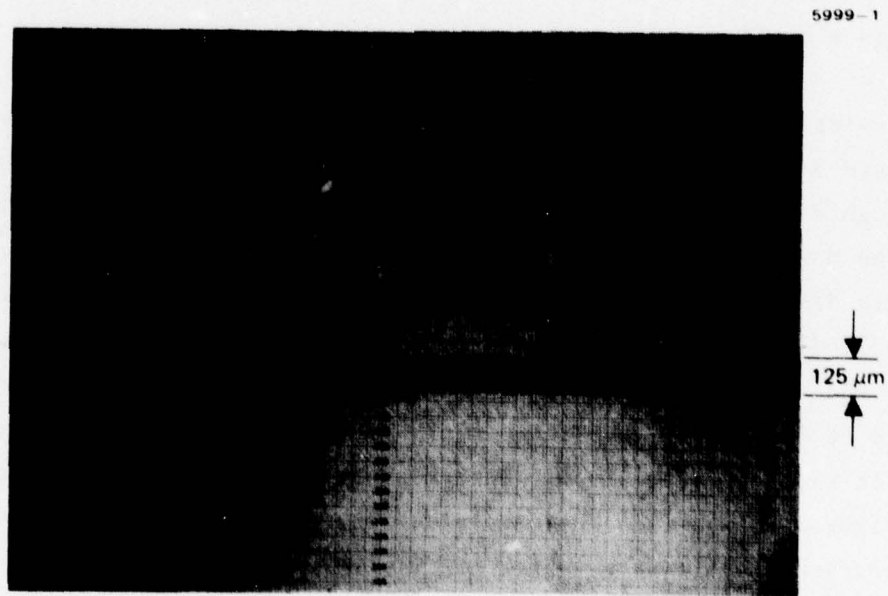


Figure 8. View of tapered fiber displayed on the screen of an optical comparator.

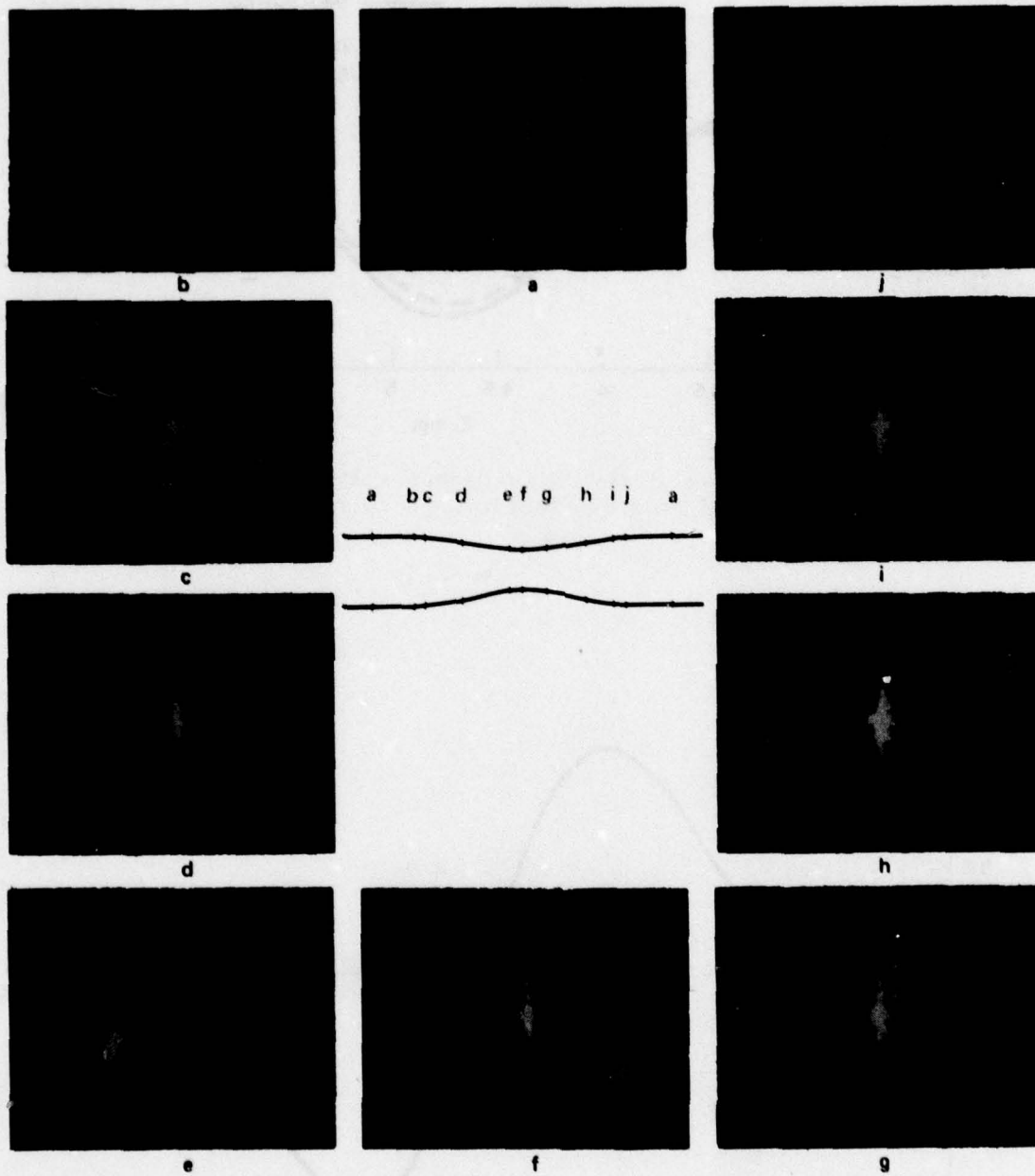


Figure 9. View of the diffraction pattern and the deflected (refracted) beam for various illuminated regions along the taper.

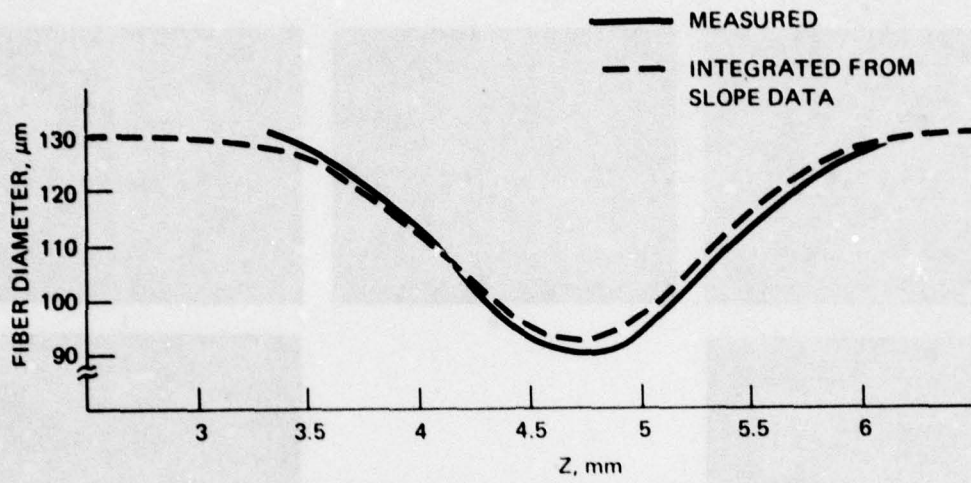


Figure 10. Variation of the fiber diameter in the tapered region measured from diffraction and refraction data.

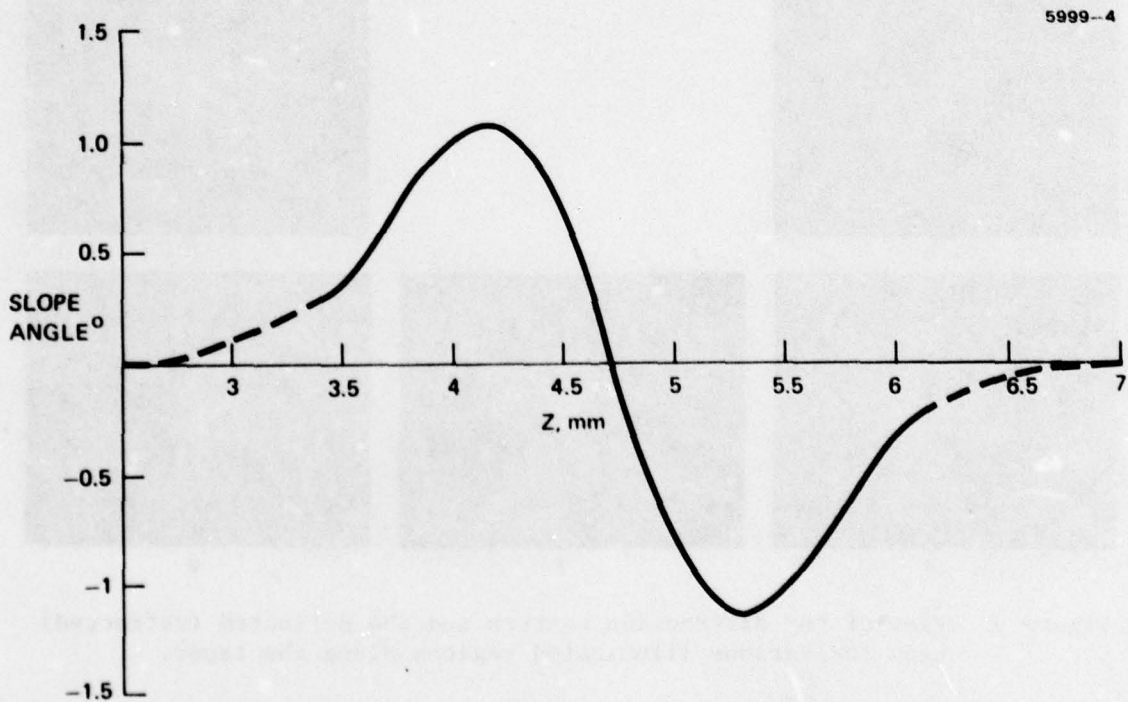


Figure 11. Variation of the slope of the taper along fiber length.

numerical integration of the data in Figure 10 after the fiber was measured with a micrometer and found to have a diameter of 130 μm . The two sets of data differ by less than 2.5%.

In addition, the optical analysis of the tapered section has been extended to other than the paraxial region. The analytical results suggest a technique for probing the internal structure of a fiber. This technique involves measurement of the intensity distribution of the deflected beam. The initial motivation for extending these calculations was that the experimental evidence (Figure 12) showed the deflection to be a function of the azimuth angle of the outgoing beam; this angle was measured with respect to the direction of the original incident light beam direction. Since ray trace analysis gives accurate results for fiber scattering problems,¹⁻⁴ the evaluation was performed using the ray approach.

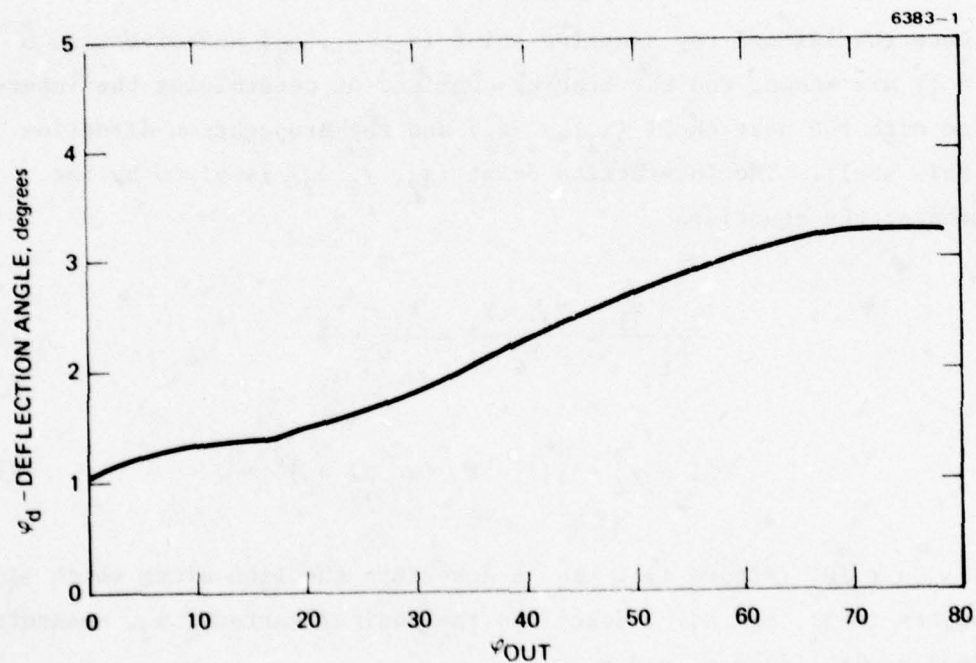


Figure 12. Experimentally determined lateral deflection angle versus the azimuth angle of the outgoing beam for a tapered fiber.

Consider the original fiber as concentric shells of radii r_m and refractive indices n_m . On generating a taper, all cross-sectional dimensions scale linearly, while the values of the refractive indices remain unchanged. The envelope of the tapered section (near the point of inflection) is given by the equation of a cone:

$$\tilde{x}^2 + \tilde{y}^2 = (R - \tilde{z} \tan \alpha)^2, \quad (4)$$

where R is the outer radius of the cross section at $\tilde{z} = 0$; α is half the apex angle; and \tilde{x} , \tilde{y} , and \tilde{z} are the three orthogonal axes of the tapered region. Normalizing the \tilde{x} , \tilde{y} , \tilde{z} coordinates with respect to R yields for the envelope of the taper (i.e., a cone)

$$x^2 + y^2 = (1 - z \tan \alpha)^2. \quad (5)$$

Once the initial ray starting point (x_1, y_1, z_1) and direction \vec{b} ($|\vec{b}| = 1$) are known, the ray tracing consists of determining the intersection with the next shell (x_2, y_2, z_2) and the propagation direction \vec{c} in this shell. The interaction point (x_2, y_2, z_2) is given by the solution of the equations

$$\frac{x_2 - x_1}{b_1} = \frac{y_2 - y_1}{b_2} = \frac{z_2 - z_1}{b_3} \quad (6)$$

$$x_2^2 + y_2^2 = [(1 - z_2 \tan \alpha) a_2]^2, \quad (7)$$

where $a_2 = r_2/R_0$ (Figure 13). Eq. 6 describes the line along which light propagates in n_1 , and Eq. 7 describes the conical surface, s_2 , separating the shells with index n_1 and n_2 .

The ray direction, \vec{c} ($|\vec{c}| = 1$) in the shell beyond s_2 is given by the solution of the generalized Snell's law

$$(n_1 \vec{b} - n_2 \vec{c}) \times \vec{p} = 0 \quad , \quad (8)$$

where \vec{p} is the normal to s_2 at the point of intersection,

$$\vec{p} = \cos(\delta) \frac{x_2}{\sqrt{x_2^2 + y_2^2}} \vec{i} + \cos(\delta) \frac{y_2}{\sqrt{x_2^2 + y_2^2}} \vec{j} + \sin(\delta) \vec{k} \quad (9)$$

with $\delta = \tan^{-1}(a_2 \tan \alpha)$. Eq. 9 indicates that the linear combination $n_1 \vec{b} - n_2 \vec{c}$ is along the normal \vec{p} or that

$$n_2 \vec{c} = n_1 \vec{b} + \Gamma \vec{p} \quad , \quad (10)$$

where Γ is a constant. By squaring Eq. 10 and using the condition $|\vec{c}| = |\vec{b}| = |\vec{p}| = 1$, a quadratic in Γ is obtained. The physically realizable solution for \vec{c} is given by the value of Γ with the smallest magnitude. The two values of Γ are given by

$$\Gamma = -n_1 \vec{b} \cdot \vec{p} \pm \sqrt{(n_1 \vec{b} \cdot \vec{p})^2 - n_1^2 + n_2^2} \quad . \quad (11)$$

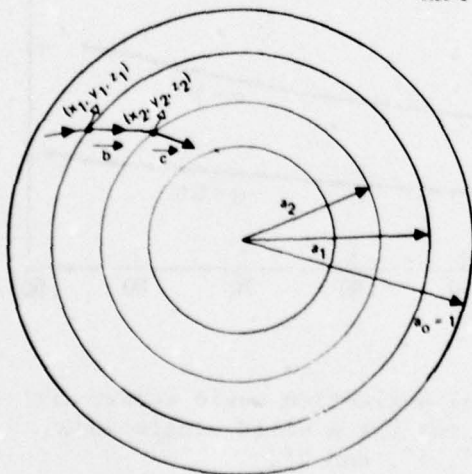


Figure 13.
Schematic of the normalized fiber shell dimensions and the ray definitions of the text.

The solution of Eqs. 6 and 7 and of 10 and 11 determines the ray after the surface s_2 ; the procedure can be repeated until the ray emerges from the fiber.

A computer program based on the above analysis has been used to analyze the optical properties of tapered fibers. The results for a solid single index fiber (no cladding) with index $n = 1.46$ (silica) and taper angles 0.5° , 1° , and 2° are shown in Figure 14. These curves confirm the experimental data in Figure 12. Since the curves are identical in shape, only data for a 1° taper is presented below.

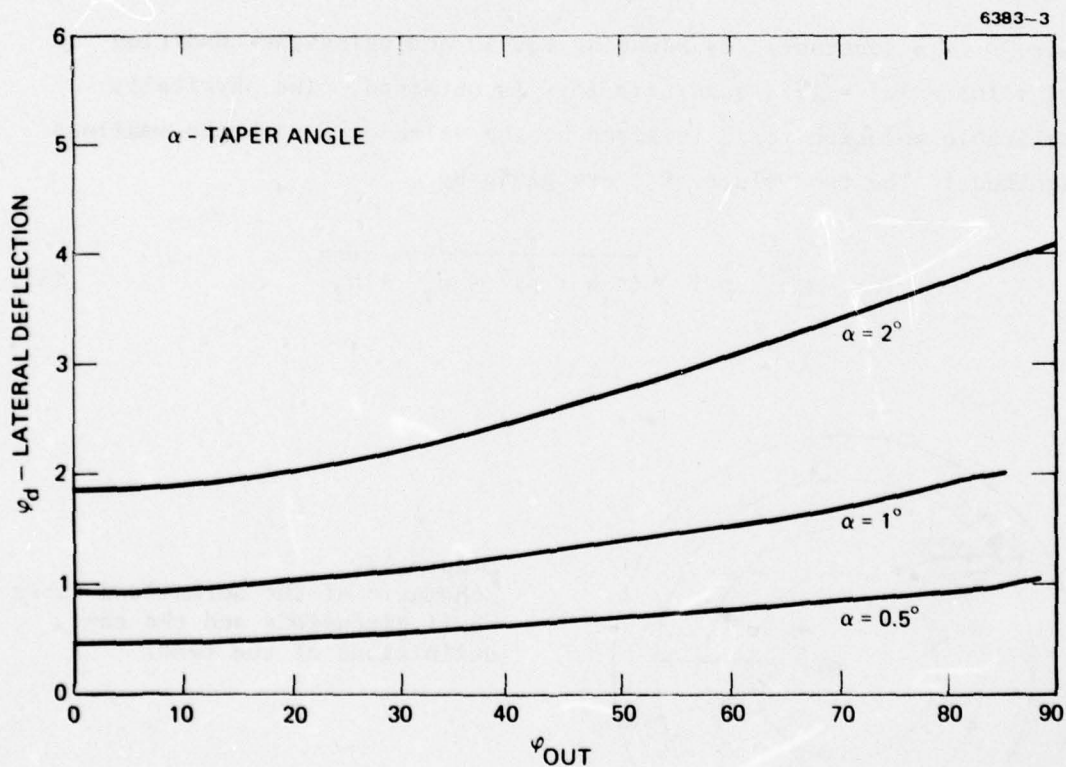


Figure 14. Analytically determined lateral deflection angle versus the azimuth angle of the outgoing ray for a solid single index fiber and taper angles of 0.5° , 1° , and 2° .

Figure 15 shows the deflection angle versus the azimuth angle for three cases:

- A uniform fiber with $n = 1.46$
- A clad fiber with $n_{\text{core}} = 1.50$ and $n_{\text{clad}} = 1.46$ (2.7% difference between core and cladding) and $r_{\text{core}}/r_{\text{clad}} = 0.5$
- Same as b except $r_{\text{core}}/r_{\text{clad}} = 0.667$.

The deflection angle does not give an easy identification of the fiber's internal structure. The paraxial deflection angle is the one predicted by Eq. 1 in conjunction with Eq. 2. For the uniform fiber (with $n = 1.46$ and $\alpha = 1^\circ$), $\mu = 0.920^\circ$; for the $r_{\text{core}}/r_{\text{clad}} = 0.5$, $n = 1.48$ and $\mu = 0.960^\circ$; and for $r_{\text{core}}/r_{\text{clad}} = 0.667$, $\bar{n} = 1.4866$ and $\mu = 0.973^\circ$.

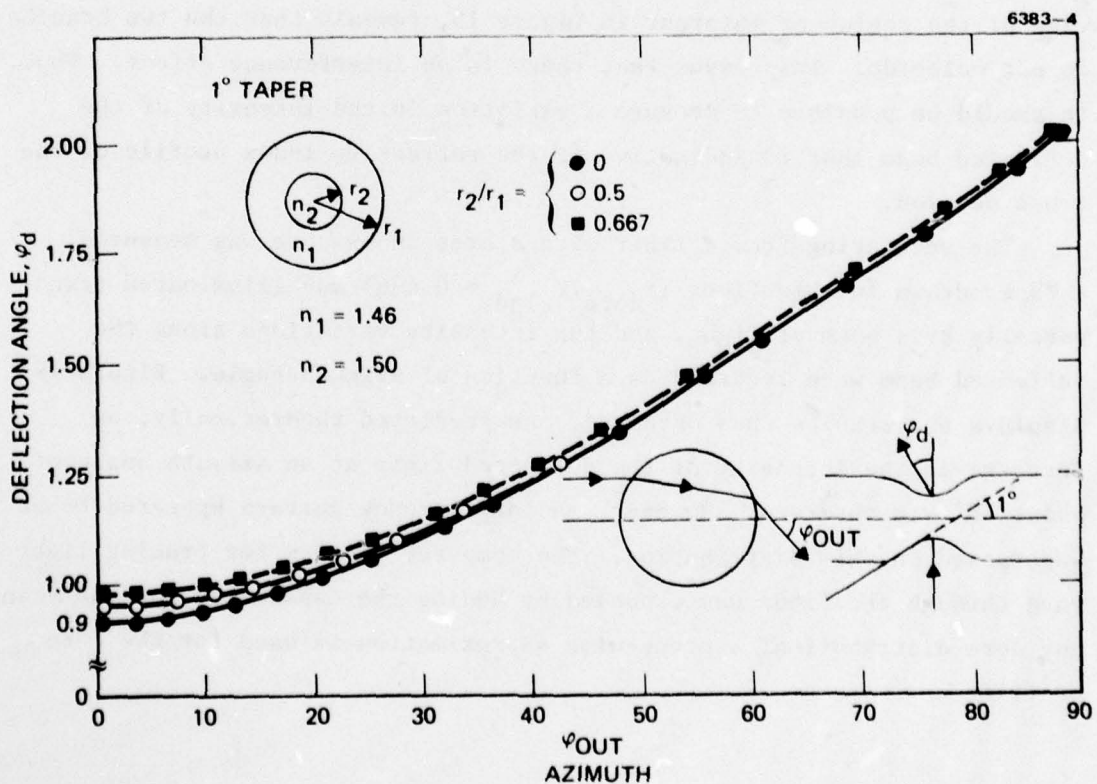


Figure 15. Analytically determined lateral deflection angle versus the azimuth angle of the outgoing ray for three clad fibers. All angles are in degrees.

On the other hand, a plot (Figure 15) of the azimuth angle, ϕ_{out} , versus the incident ray position (identified by the polar coordinate, ϕ_{in} , of input ray intersection), shows that for clad fibers this function is double valued for a range of angles, ϕ_{out} . The reason for this is that some of the rays penetrating both the core and cladding exit at the same angle as other rays penetrating only through the cladding.

It is instructive to plot the relative geometrical intensity of the deflected beam as a function of azimuth angle (Figure 17). The region of overlap exhibits a locally increased intensity, due to the superposition of the two beams. This intensity increase is more detectable for the $r_{\text{core}}/r_{\text{clad}} = 0.5$ case since the geometrical intensity is more localized at the lower azimuth angles. Because interference effects are possible, the dependence of the deflection angles, ϕ_{d} , with the azimuth angle, ϕ_{out} , should be examined in detail for the two branches. Figure 18, an expanded view of the region of interest in Figure 15, reveals that the two branches do not coincide. This means that there is no interference effect. Thus, it should be possible to measure a variation in the intensity of the deflected beam that is indicative of the refractive index profile of the cross section.

The scattering from a fiber with a step index core was measured. A taper drawn in this fiber ($r_{\text{core}}/r_{\text{clad}} = 0.436$) was illuminated transversally by a beam of light, and the intensity variations along the deflected beam were recorded as a function of azimuth angle. Figure 19 displays the results thus obtained. As predicted theoretically, an increase in the intensity of the deflected light at an azimuth angle of about 18° was observed. However, an interference pattern appeared to be superposed on this distribution. The computer program for tracing light rays through the fiber was expanded by adding the capability for analyzing any core distribution; a piece-wise approximation is used for the core profile.

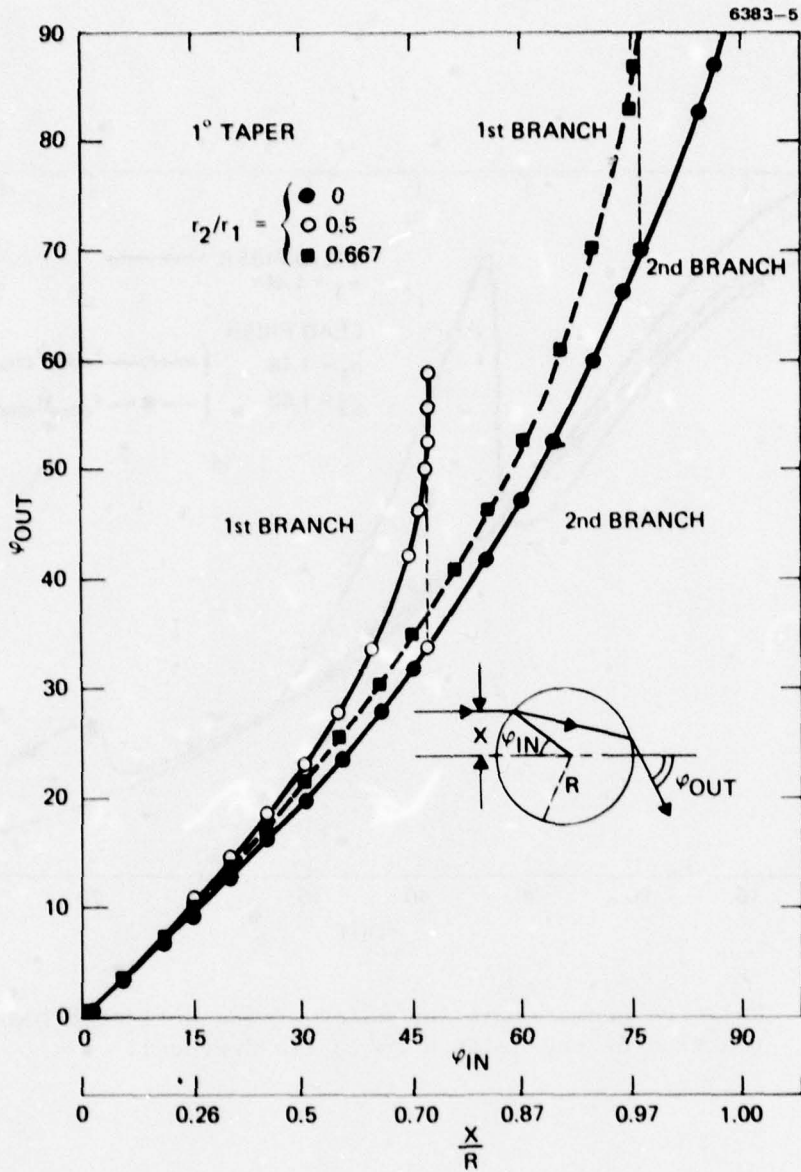


Figure 16. Analytically determined azimuth angle versus the incident ray position. All angles are in degrees.

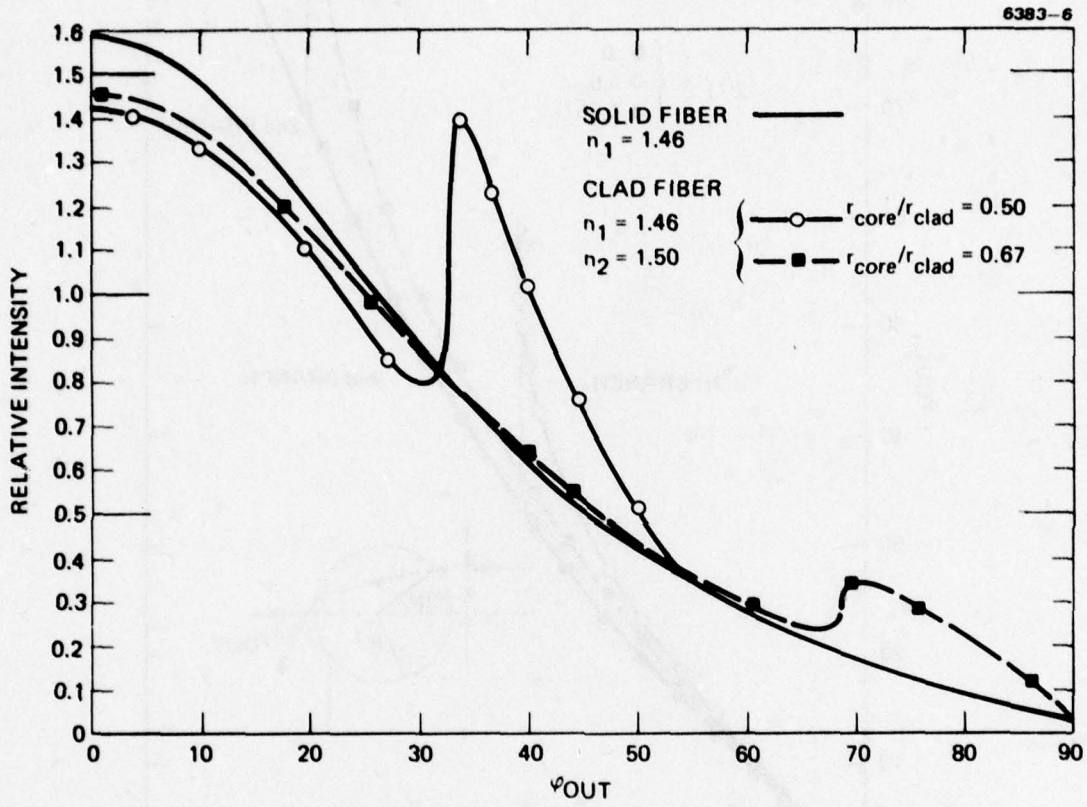


Figure 17. Relative geometrical intensity of the deflected beam as a function of the azimuth angle (in degrees).

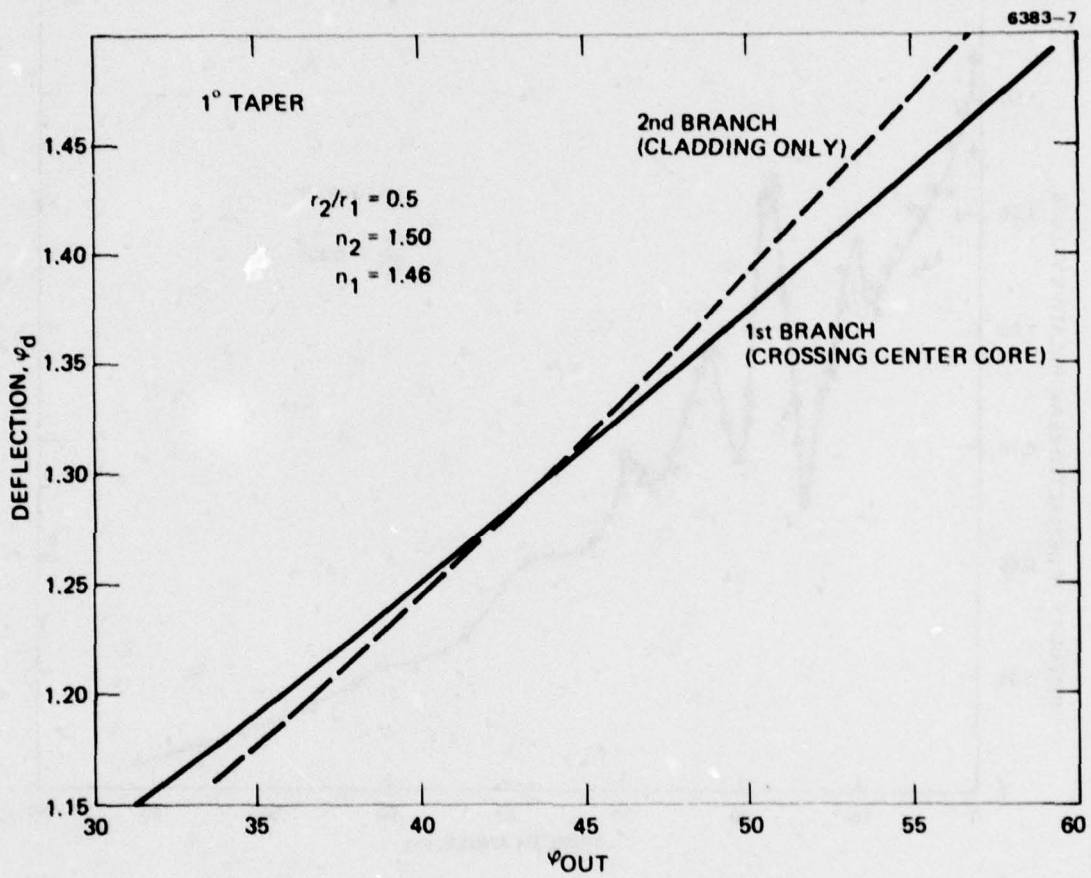


Figure 18. Analytically determined lateral deflection angle versus the azimuth angle of the outgoing ray for the case indicated. All angles are in degrees.

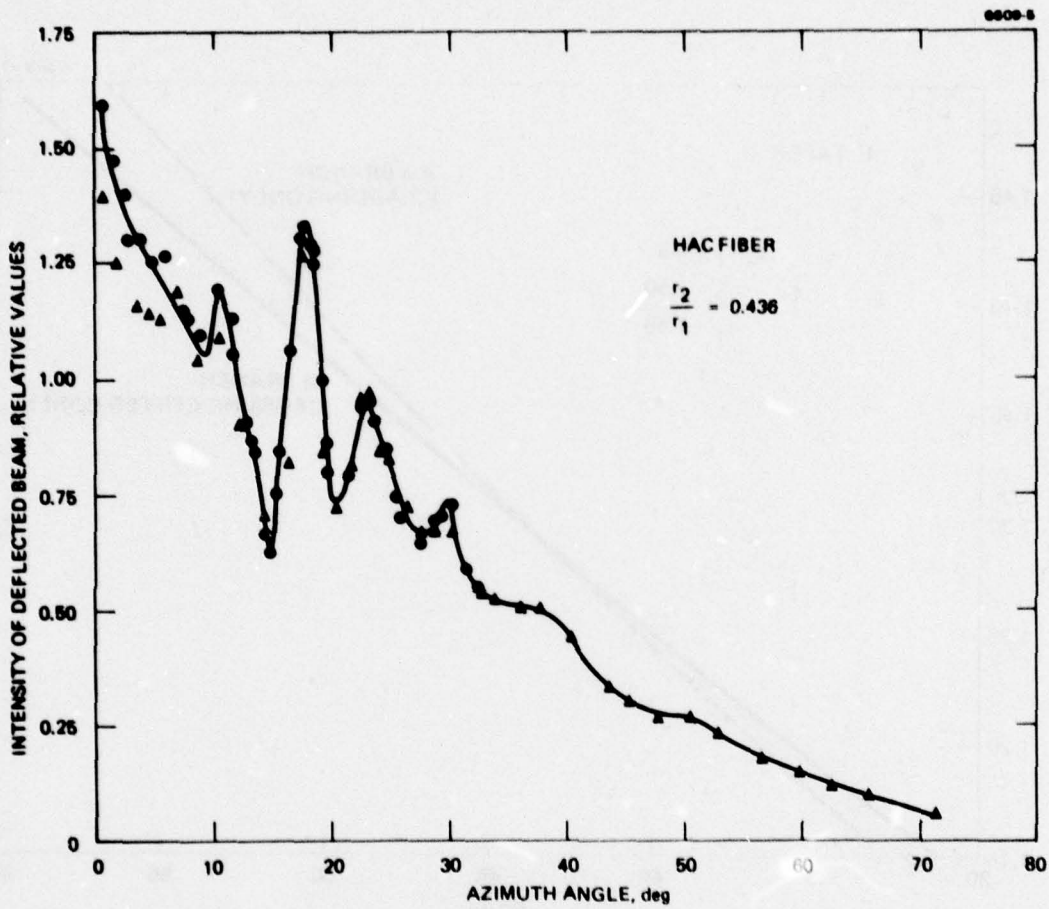


Figure 19. Measured intensity versus the azimuth angle for a step index fiber with clad core radius ratio of 0.426.

SECTION 3

STUDY AND DEVELOPMENT OF ACCESS COUPLERS FOR SINGLE STRAND SYSTEMS

There are strong trends in military system design (particularly shipboard and airborne) toward microminiaturization, digital processing, and system-level integration to reduce size, weight, and power consumption; lower cost; and improve reliability. Since these trends naturally point to data bus multiplexing, we have developed low-insertion-loss (about 1 dB) optical access couplers for interconnecting, by fiber optic waveguide cables, several spatially distributed terminals. The primary fabrication techniques investigated during this study are discussed in this section. In addition, the modal properties of the optimized couplers are discussed.

The equipment setup for evaluating the couplers is shown in Figure 20. Both the input and the output fibers are mode stripped. The input fiber is held rigid during the measurements by waxing it to a post. Light power measurements are made using a power meter. After the power has been measured at the output ends of the coupler, the input fiber is cleaved, and the input power is measured. Light from the HeNe laser is launched into the fiber using an 80X microscope objective with numerical aperture of 0.8. The light throughput in the input fiber is maximized

7247-1

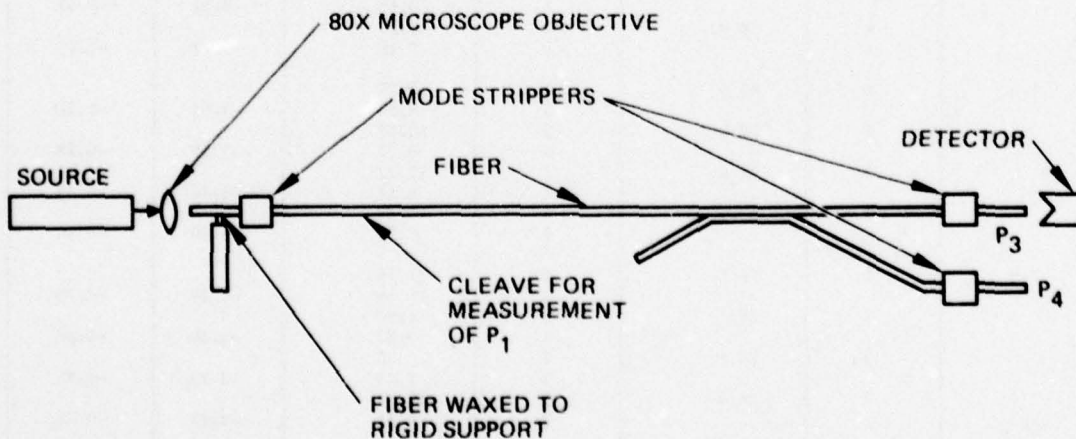


Figure 20. Equipment for coupling evaluation.

Table 1. Fused T-Coupler Data

Coupler No.	Input Port	Input Power, μW	Output Port	Output Power, μW	Coupling Ratio, dB	Excess Loss, dB
1-3	1	29.0	4	15.41	-3.9	-0.47
			3	10.58		
	2	29.0	3	11.50	-3.4	-1.36
			4	9.66		
	3	29.0	2	13.13	-3.4	-0.79
			1	11.04		
	4	28.0	1	13.06	-3.64	-0.85
			2	9.95		
2-3	1	29.5	4	12.45	-3.45	-1.13
			3	10.24		
	2	29.7	3	14.70	-3.71	-0.64
			4	10.88		
	3	30.2	2	13.40	-3.40	-0.88
			1	11.25		
	4	28.8	1	13.42	-3.65	-0.87
			2	10.15		
3-3	1	28.5	3	13.00	-3.54	-0.87
			4	10.30		
	2	27.7	4	11.04	-3.02	-0.99
			3	10.97		
	3	28.2	1	13.58	-3.60	-0.68
			2	10.48		
	4	30.3	2	11.26	-3.50	-0.79
			1	11.26		
4-3	1	30.8	3	14.40	-3.48	-0.72
			4	11.69		
	2	28.6	4	12.39	-3.37	-0.95
			3	10.54		
	3	26.9	1	11.50	-3.31	-0.96
			2	10.02		
	4	26.7	2	11.36	-3.42	-1.14
			1	9.45		
5-3	1	27.5	4	12.80	-3.50	-0.75
			3	10.33		
	2	26.0	3	12.10	-3.52	-0.85
			4	9.26		
	3	26.7	2	13.28	-3.51	-0.47
			1	10.65		
	4	18.82	1	8.27	-3.72	-1.17
			2	6.10		
6-3	1	25.5	4	9.70	-3.03	-1.21
			3	9.57		
	2	24.1	3	10.58	-3.19	-0.73
			4	9.76		
	3	23.4	2	11.22	-3.46	-0.59
			1	9.18		
	4	23.2	1	10.34	-3.50	-0.94
			2	8.34		
7-3	1	26.3	4	11.68	-3.29	-0.78
			3	10.29		
	2	26.1	3	11.60	-3.38	-0.85
			4	9.82		
	3	23.1	2	10.35	-3.29	-0.74
			1	9.10		
	4	26.4	1	12.81	-3.62	-0.66
			2	9.84		

6115

Table 1. Continued

Coupler No.	Input Port	Input Power, μW	Output Port	Output Power, μW	Coupling Ratio, dB	Excess Loss, dB
8-3	1	25.0	3	10.97	-3.20	-0.75
			4	10.04		
	2	26.0	4	12.90	-3.65	-0.59
			3	9.76		
	3	26.0	1	12.56	-3.79	-0.81
2			9.01			
4	24.0	2	11.60	-3.61	-0.68	
		1	8.92			
9-3	1	25.2	4	13.6	-3.8	-0.34
			3	9.7		
	2	23.0	3	11.0	-3.60	-0.71
			4	8.5		
	3	27.2	2	13.9	-3.79	-0.56
1			9.96			
4	26.8	1	13.4	-3.71	-0.52	
		2	9.9			
103	1	27.0	4	12.54	-3.39	-0.67
			3	10.58		
	2	25.0	3	10.16	-3.38	-1.24
			4	8.61		
	3	25.0	2	11.3	-3.37	-0.77
1			9.6			
4	27.0	1	13.7	-3.87	-0.65	
		2	9.5			
11-3	1	27.0	3	12.8	-3.63	-0.77
			4	9.8		
	2	27.4	4	12.4	-3.48	-0.86
			3	10.1		
	3	27.4	1	12.3	-3.32	-0.76
2			10.7			
4	26.8	2	12.9	-3.55	-0.63	
		1	10.2			
12-3	1	28.0	4	12.1	-3.37	-0.97
			3	10.3		
	2	24.0	3	12.1	-3.44	-0.36
			4	10.0		
	3	27.4	2	12.3	-3.37	-0.80
1			10.5			
4	25.0	1	12.0	-3.31	-0.46	
		2	10.5			
1-6	1	27.7	3	18.93	-6.69	-0.60
			4	5.15		
	2	23.7	4	14.15	-6.14	-1.03
			3	4.54		
	3	24.1	1	14.75	-6.11	-0.91
2			4.77			
4	24.9	2	16.56	-6.64	-0.71	
		1	4.58			
2-6	1	26.0	3	19.15	-7.11	-0.38
			4	4.62		
	2	25.0	4	16.02	-5.85	-0.62
			3	5.62		
	3	27.0	1	18.75	-6.48	-0.47
2			5.44			
4	27.0	2	16.87	-6.09	-0.81	
		1	5.50			

Table 1. Continued

Coupler No.	Input Port	Input Power, μW	Output Port	Output Power, μW	Coupling Ratio, dB	Excess Loss, dB
3-6	1	27.0	3	17.50	-5.62	-0.49
			4	6.60		
	2	28.0	4	19.15	-6.42	-0.52
			3	5.64		
4-6	3	26.0	1	16.71	-6.10	-0.69
			2	5.43		
	4	26.0	2	16.43	-5.89	-0.70
			1	5.69		
5-6	1	25.0	4	17.4	-6.95	-0.60
			3	4.4		
	2	25.0	3	17.0	-6.79	-0.66
			4	4.5		
6-6	3	25.5	2	18.7	-6.9	-0.35
			1	4.8		
	4	27.0	1	19.0	-6.68	-0.48
			2	5.2		
7-6	1	27.0	3	19.0	-6.61	-0.46
			4	5.3		
	2	24.0	4	16.2	-5.79	-0.38
			3	5.8		
8-6	3	27.0	1	18.4	-5.99	-0.44
			2	6.2		
	4	24.5	2	16.0	-5.39	-0.37
			1	6.5		
9-6	1	24.0	3	16.00	-6.22	-0.57
			4	5.01		
	2	27.0	4	18.53	-6.54	-0.54
			3	5.27		
10-6	3	30.0	1	16.90	-5.98	-1.23
			2	5.70		
	4	26.0	2	17.04	-6.06	-0.60
			1	5.60		
11-6	1	25.0	3	14.45	-5.24	-0.83
			4	6.17		
	2	25.0	4	14.13	-5.51	-1.04
			3	5.51		
12-6	3	27.0	1	17.75	-6.02	-0.57
			2	5.90		
	4	27.0	2	17.69	-5.80	-0.51
			1	6.31		
13-6	1	29.0	3	19.25	-6.41	-0.65
			4	5.69		
	2	29.0	4	19.94	-6.49	-0.52
			3	5.76		
14-6	3	28.0	1	19.97	-6.43	-0.34
			2	5.87		
	4	26.0	2	16.03	-5.64	-0.71
			1	6.01		
15-6	1	26.0	3	16.91	-6.30	-0.70
			4	5.17		
	2	24.0	4	17.47	-6.42	-0.25
			3	5.15		
16-6	3	25.0	1	16.60	-5.85	-0.47
			2	5.82		
	4	27.0	2	18.78	-7.10	-0.63
			1	4.54		

Table 1. Continued

Coupler No.	Input Port	Input Power, μW	Output Port	Output Power, μW	Coupling Ratio, dB	Excess Loss, dB
10-6	1	27.0	4	18.56	-6.34	-0.48
			3	5.61		
	2	28.0	3	19.64	-6.81	-0.52
			4	5.16		
	3	25.0	2	15.51	-5.71	-0.71
			1	5.68		
4	28.0	1	18.78	-6.03	-0.48	
		2	6.24			
11-6	1	23.0	4	16.00	-6.07	-0.34
			3	5.24		
	2	28.0	3	16.06	-5.53	-0.99
			4	6.23		
	3	27.0	2	16.12	-5.71	-0.88
			1	5.91		
4	23.0	1	16.41	-6.86	-0.46	
		2	4.25			
12-6	1	25.0	4	16.13	-5.64	-0.51
			3	6.05		
	2	25.0	3	16.03	-5.08	-0.31
			4	7.20		
	3	29.0	2	19.90	-6.74	-0.60
			1	5.34		
4	24.0	1	16.30	-5.91	-0.39	
		2	5.62			
1-10	1	27.5	4	24.6	-11.3	-0.15
			3	1.95		
	2	26.0	3	20.0	-10.22	-0.70
			4	2.1		
	3	28.0	2	23.0	-10.77	-0.50
			1	2.1		
4	28.0	1	23.0	-10.77	-0.50	
		2	2.1			
2-10	1	24.5	3	29.0	-10.2	-0.45
			4	2.1		
	2	30.0	4	22.0	-10.2	-0.92
			3	2.3		
	3	26.0	1	21.0	-9.6	-0.42
			2	2.6		
4	26.0	2	22.0	-10.8	-0.35	
		1	2.0			
3-10	1	26.0	3	20.0	-10.0	-0.69
			4	2.2		
	2	24.5	4	20.0	-10.4	-0.47
			3	2.0		
	3	25.0	1	20.0	-9.54	-0.46
			2	2.5		
4	28.0	2	22.2	-9.0	-0.49	
		1	2.8			
4-10	1	25.0	3	22.0	-10.15	-0.10
			4	2.35		
	2	27.5	4	22.0	-9.76	-0.48
			3	2.6		
	3	26.6	1	21.0	-10.4	-0.61
			2	2.1		
4	26.0	2	21.0	-9.3	-0.38	
		1	2.8			

Table 1. Continued

Coupler No.	Input Port	Input Power, μ W	Output Port	Output Power, μ W	Coupling Ratio, dB	Excess Loss, dB
5-10	1	25.0	3	19.2	-9.6	-0.70
			4	2.37		
	2	26.6	4	20.0	-9.6	-0.73
			3	2.46		
	3	23.8	1	18.0	-8.87	-0.61
2	2.7					
4	27.4	2	22.7	-10.7	-0.43	
		1	2.1			
6-10	1	23.9	3	21.0	-11.4	-0.24
			4	1.6		
	2	24.3	4	20.0	-9.54	-0.33
			3	2.5		
	3	25.9	1	20.0	-9.89	-0.65
2	2.28					
4	24.0	2	20.0	-10.22	-0.35	
		1	2.1			
7-10	1	27.0	3	21.0	-9.58	-0.58
			4	2.6		
	2	27.0	4	20.8	-9.4	-0.6
			3	2.7		
	3	28.0	1	23.0	-9.93	-0.39
2	2.6					
4	28.0	2	22.5	-9.17	-0.39	
		1	3.10			
8-10	1	27.0	3	22.0	-10.8	-0.51
			4	2.0		
	2	25.0	4	20.0	-9.87	-0.5
			3	2.3		
	3	27.0	1	22.8	-10.38	-0.32
2	2.3					
4	28.8	2	22.5	-10.0	-0.61	
		1	2.5			
9-10	1	28.0	3	20.5	-9.8	-0.87
			4	2.40		
	2	28.0	4	21.5	-9.67	-0.65
			3	2.6		
	3	26.5	1	21.0	-9.16	-0.45
2	2.9					
4	26.0	2	21.0	-9.3	-0.38	
		1	2.8			
10-10	1	26.6	3	21.0	-9.58	-0.52
			4	2.6		
	2	26.3	4	21.5	-9.38	-0.34
			3	2.8		
	3	25.5	1	20.0	-9.54	-0.5
2	2.5					
4	26.5	2	21.0	-9.29	-0.47	
		1	2.8			
11-10	1	27.0	3	21.0	-9.6	-0.58
			4	2.6		
	2	24.3	4	23.8	-10.6	-0.47
			3	2.25		
	3	29.0	1	23.3	-10.6	-0.56
2	2.2					
4	27.5	2	20.0	-9.4	-0.83	
		1	2.6			

Table 1. Continued

Coupler No.	Input Port	Input Power, μW	Output Port	Output Power, μW	Coupling Ratio, dB	Excess Loss, dB
12-10	1	27.5	3	21.0	-9.6	-0.66
			4	2.6		
	2	25.1	4	21.2	-10.7	-0.16
			3	1.98		
	3	28.0	1	22.0	-10.6	-0.68
			2	2.1		
	4	25.0	2	20.0	-9.85	-0.34
			1	2.31		

before the measurements are made. The primary disadvantage of this measurement apparatus is that only the "meridional" modes of the fiber are fully excited. Limited measurements have been made with sources (LEDs) that excite the full mode spectrum; the results of these measurements are discussed in the text.

As part of this contract, 36 couplers (12 each of 3, 6, and 10 dB) were delivered. A copy of the measured coupling ratios and insertion losses are given in Table 1. The coupling ratio is defined as the coupled power divided by the total output power; the coupled power is the smaller of the two output powers. The excess loss is defined as the total output power divided by the total input power. The data given in Table 1 are summarized in Figure 21, where the average loss is plotted versus the average coupling ratio for each of the 36 couplers.

Couplers were fabricated using several methods; the three primary ones are discussed. In the fabrication Corning No. 1025 fiber with the protective coating removed, was used throughout. The three primary methods of fabrication were: (1) a 50 W CO₂ laser was used to fuse fibers in a curved fixture, (2) fibers that had a portion of the cladding and core removed by lapping and polishing were either epoxied or cemented together using an index-matching adhesive, and (3), the 50-W laser and a torch were used to fuse twisted pairs of fiber; a taper was pulled during fusing. The twisted-pair approach solved two problems: (1) the two fibers stayed in intimate contact during the fusion process without having to be in contact with a fixture, and (2) the twisted and tapered configuration facilitates better coupling.

The junctions made with the curved welding fixture were not satisfactory. The basic problem arose in the following manner. At the position where the weld was desired, the fibers were pressed against the fixture to ensure that the fibers were in contact. This produced a very efficient and localized heat sink. However, a short distance away the fibers were not pressed against the fixture and on heating distorted, pulled away from the fixture, and moved together. This motion was due to the stresses in the fibers. The end result was a distorted contact with little hope of being controlled. Another problem with this technique was the low

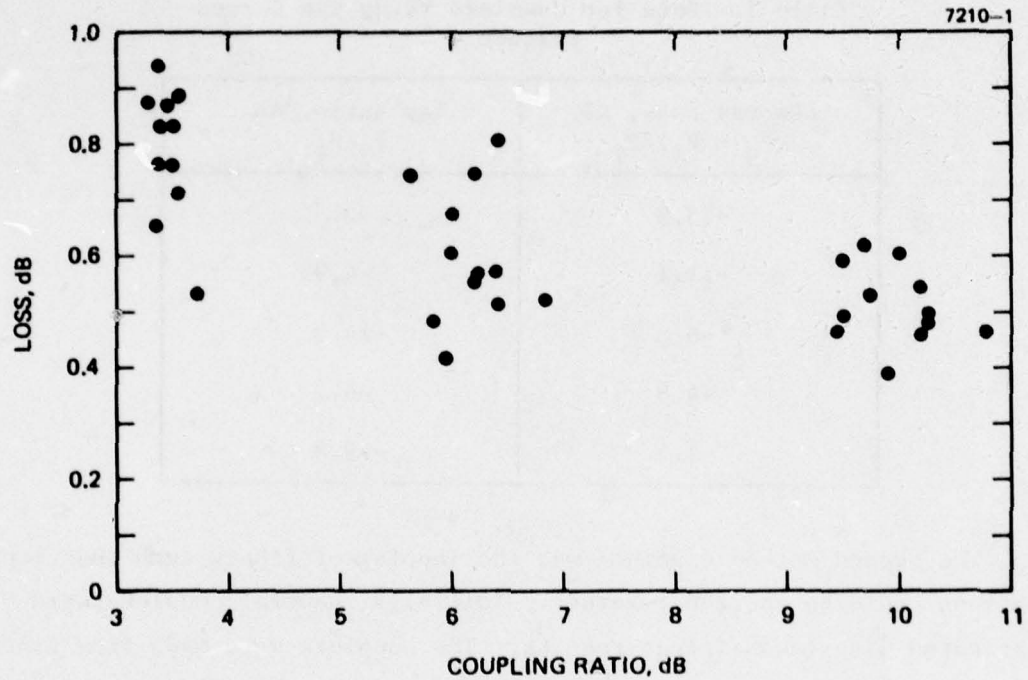


Figure 21. T-coupler data. Each point on the graph represents the average excess loss and coupling ratio for a single couple. Each coupler has four measured excess losses and coupling ratios, one pair for each (input) part (see Table 1).

yield of usable junctions (<10% of attempts). A spectrum of the typical values for excess loss and tap ratio is shown in Table 2. In general, a low tap ratio coupler had a high excess loss. The power levels P_1 , etc. are indicated in Figure 20.

Table 2. Data for Couplers Using the Curved Fixture

Excess Loss, dB $(P_3 + P_4)/P_1$	Tap Ratio, dB P_3/P_4
-13.2	-5
-11.1	-4.92
-8	-14.5
-4.9	-6.7
-1.5	-19.3

The second method examined was the lapping of fibers such that lapped sections could be epoxied together. Initially, several couplers were fabricated with inconsistent results. The couplers were made from fibers lapped on a 25 cm radius to a depth of 24 μm (4 μm into the core). The lapped region was 7 mm long and the core was exposed over a length of approximately 1 mm. Experiments initiated to determine the source of inconsistency involved mounting lapped fibers in the holder for epoxying (Figure 22) and then substituting glycerol for epoxy. This allowed adjusting the fibers in the holder. The alignment of the exposed core regions for fibers lapped on a 25 cm radius was found to be critical. Figure 23 shows the coupled power versus the longitudinal alignment along the fibers. Fibers were then lapped on a 100 cm radius and the above experiment repeated. The result was that the alignment was much less critical. Next the hypothesis that the epoxy and glycerol produce the same effect was tested by removing the glycerol after alignment and applying epoxy. The effects of the glycerol and the epoxy were similar, and a trend in the coupling versus depth of lap was established (Figure 24)



Figure 22. Fixture for holding the lapped and polished fibers.

for the 100 cm radius. In an attempt to make a 3-dB coupler (0-dB tap) using this method, fibers were lapped halfway into the core using a 10-cm radius. This increased the loss and produced a coupling that was much lower than expected. After the fibers were lapped, the excess loss of the fiber itself was in excess of 2 dB; this was due to radiation in the lapped section. It was expected that this radiation would be captured by the adjacent fiber after application of index matching fluid or epoxy. The most disturbing results from this experiment was that, both before and after the application of the index matching material or epoxy, the excess loss was constant; the loss was independent of the coupling, and the radiated light was not captured by the adjacent fiber. This phenomena had occurred during previous experiments but had not been noticed.

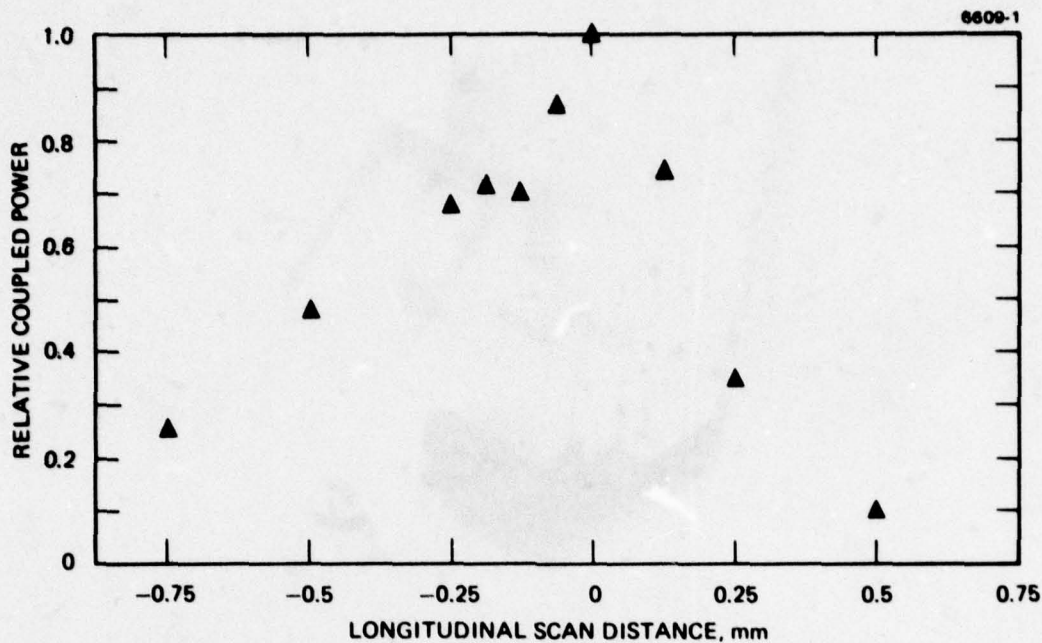


Figure 23. The coupled power versus the alignment of lapped fibers. The alignment was varied longitudinally along the length of the lapped region. Fibers were lapped on a 25 cm radius.

The welding or fusing of twisted fibers with a flame in a fixture designed for taper pulling has proven to have the lowest loss and be the most reproducible. The fibers are twisted to ensure contact at the desired weld position; after a weld is established, a taper is pulled. In initial experiments where a CO_2 laser was used to fuse the fibers, we were unable to establish reproducibility in the coupling efficiency and loss. One difficulty was isolated to be the inconsistency of the laser mode and energy distribution. The installation of an aperture in the laser cavity forced the laser to oscillate in a single mode. Many couplers ("identical" except for the taper length) were made and the insertion loss and tap ratio were measured. This experiment indicated that there is an increased coupling at larger taper lengths. However, the insertion loss data were scattered. These data are plotted in Figure 25.

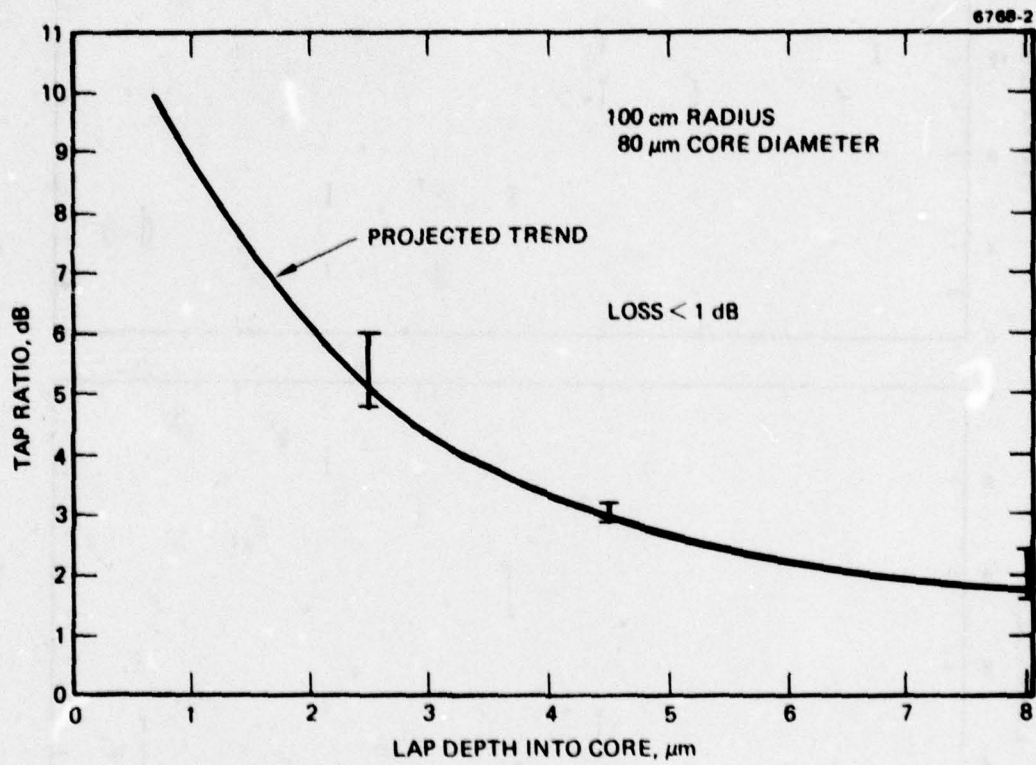


Figure 24. The projected (from experimental data) trend in coupling versus lap depth with a 100 cm lap radius.

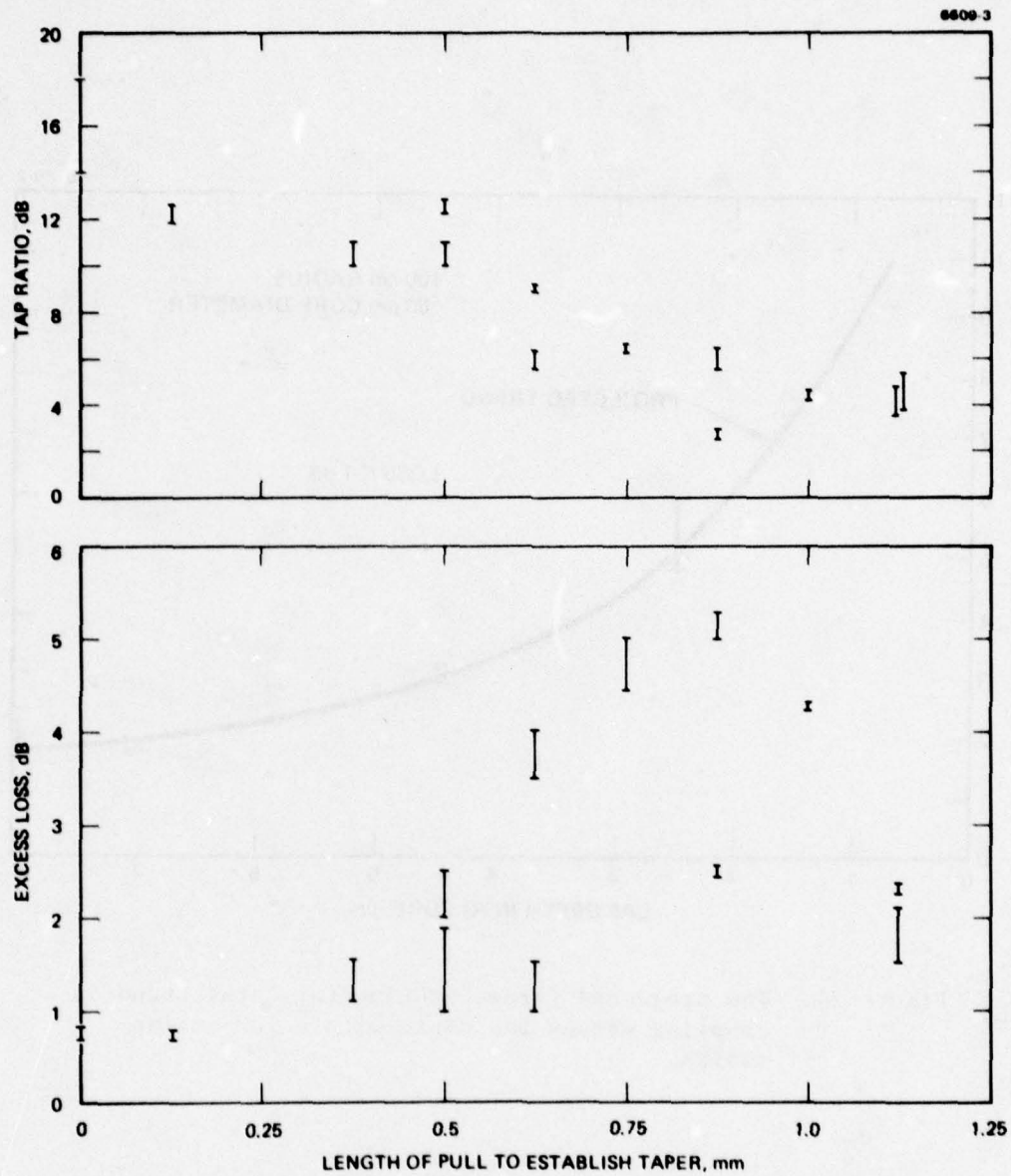


Figure 25. The excess loss and tap ratio measured for fabricated couplers. The error bars indicate the spread of the data for a single coupler but different input ports. The initial weld length was 3.5 mm.

A measurement apparatus was incorporated into the actual welding and taper pulling setup to monitor loss and coupling during the coupler fabrication. Figure 26 shows that the coupling and loss increase with the length of a single taper. However, an initial 2.3 dB loss cannot be attributed to pulling the taper; the loss due to the taper is less than 1 dB (the initial weld length was 9 mm). The scatter in the loss data in Figure 25 is believed due to a variation in this initial loss. Various attempts to eliminate the initial loss were made. The best approach was to use a flame instead of the CO₂ laser.

The more efficient coupling action of the tapered weld can be understood by considering how the coupler works.⁵ As the light enters the narrowing tapered section, the higher order modes are forced to radiate out of the core area to be guided as cladding modes. The light can cross the fused boundary between the two bi-conical sections and is, therefore, guided in the overall structure. As the light propagates to the region

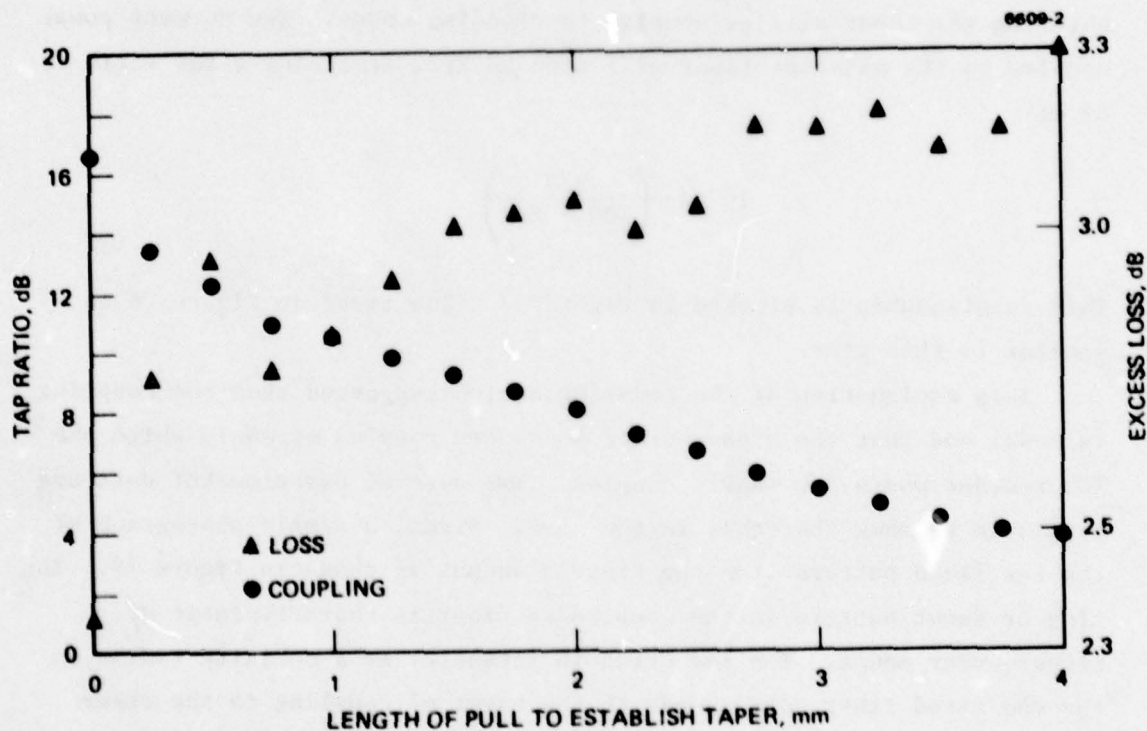


Figure 26. Coupling and loss versus length of pull to establish taper for a single pair of fibers.

of increasing tapers, the cladding modes propagate at gradually decreasing angles to the fiber axis and are recaptured by the tapered core section to again become core modes. Experimental data supporting this description is discussed in Section 1 of this report. In summary, the modal and total loss of a tapered fiber are dependent on the refractive index of the medium surrounding the taper. When a taper was surrounded by diiodomethane ($n = 1.74$), the losses were substantially higher than when the taper was exposed to air. When the taper was exposed to air, the cladding modes that propagate to the region of increasing taper were recoupled into the core. However, when the surrounding medium has a higher index, the condition that supports the cladding modes no longer exists, and the energy was radiated.

Consider a T coupler with a taper reducing the cross-sectional area of the fibers by X percent, equal recoupling to the initial and adjacent fibers, and no loss. Under these conditions, X percent of the power entering the taper will be coupled to cladding modes. The percent power coupled to the adjacent fiber will then be X/2, producing a tap ratio in dB of

$$10 \log \left(\frac{X/2}{100 - X/2} \right) .$$

This relationship is plotted in Figure 27. The trend in Figure 26 is similar to this plot.

This explanation of the coupling action suggested that the coupling is modal and that the higher-order modes are coupled strongly while the lower-order modes are weakly coupled. Two sets of experimental data are available to show that this is the case. First, a simple photograph of the far field pattern from the fiber's output is shown in Figure 28. The ring or donut pattern in the coupled to fiber is characteristic of higher-order modes. The reduction in intensity at a definite radius in the end fired fiber corresponds to the onset of coupling to the other fiber; the intensity near the edge of the rings appears to be decreasing,

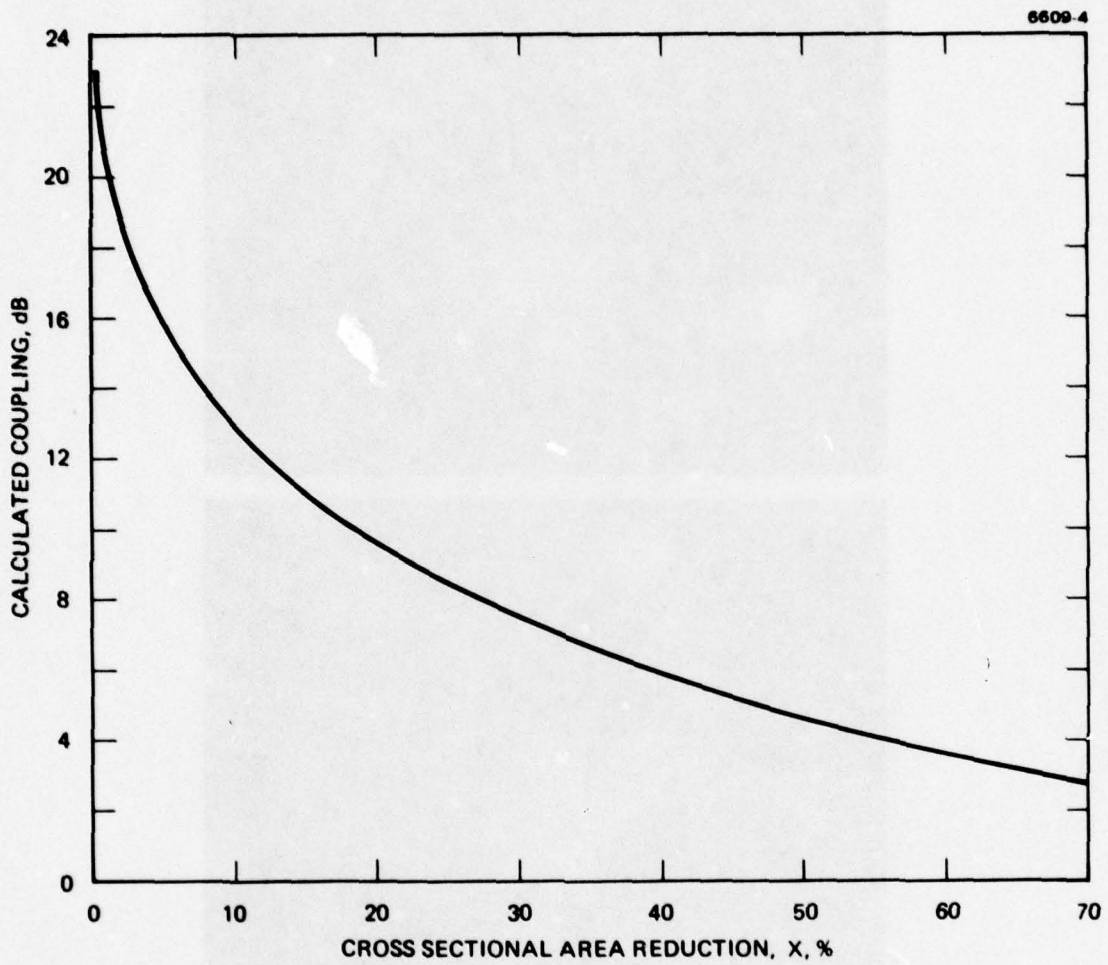


Figure 27. Theoretical curve for the coupling versus the cross-sectional area reduction in a fused tapered T coupler.

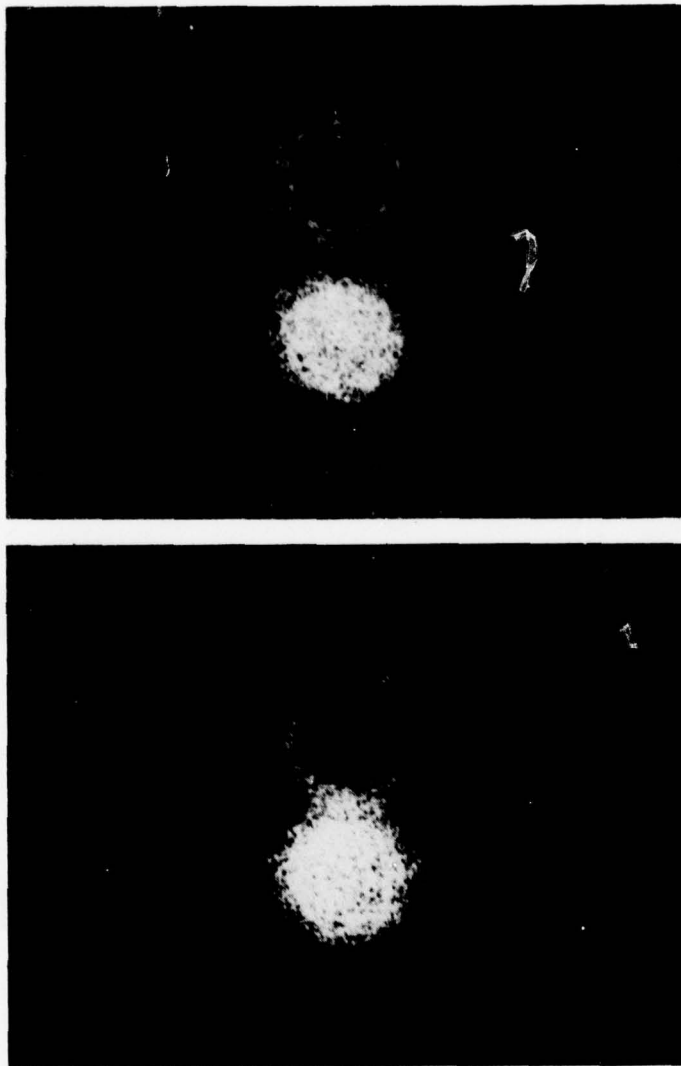


Figure 28. Photograph of the far field pattern obtained with a low loss twisted and tapered T coupler. The measured excess loss is 0.4 dB and the tap ratio is 9.5 dB.

indicating increased loss for the highest order modes; and the sum of the intensity in the two fibers is approximately constant.

The second set of data presents measurements made by butt coupling the T coupler to a fiber attached to a prism coupler. This T coupler had a tap ratio of -3.5 dB and excess loss of 1 dB measured in the end fire test arrangement which excites the full N.A. of "meridional" modes. The prism coupler allows the excitation of mode groups in the fiber that are not necessarily "meridional" in nature; previous data indicated that there is little if any mode mixing at the butt coupler between fibers. Figure 29 shows the coupling and loss (including the loss at the butt coupler) for 13 distinct mode groups (13 different angles of incidence on the prism coupler). The lowest order modes (highest modal index) has very low coupling and low loss (the 0.7 dB loss is typical of a good butt coupler). The *step-function-like* behavior for both the coupling and loss occurring at a modal index of about 1.465 corresponds to the onset of significant coupling to the clad at the tapered weld. The highest order modes have significant coupling, but are 1 dB short of the 0 dB desired ratio. However, this is only a 6% difference in overall power to the two branches, which is within experimental error. At first sight, one might expect that the modal average of the coupling and loss would equal the measured loss and coupling with full N.A. excited. This does not occur, however, because of the differences in modal excitation. To prove this point, would require exciting the coupler with an LED source. Before this could be done, however, the coupler was broken. Similar measurements on different couplers have shown an increased coupling and increased loss with LED sources. For example, with another coupler and the HeNe end fire arrangement we measured a tap ratio of 7.5 dB and loss of 0.2 dB. With the GaAlAs LED and the same input port, the tap ratio was 5.2 dB and loss 0.7 dB.

We are now able to maintain the loss for the 3-dB couplers to approximately 1 dB. For 6- and 10-dB couplers, we are able to maintain the losses substantially below 1 dB. The best results we have obtained to date for 3-, 6-, and 10-dB couplers are 0.6, 0.4, and 0.3 dB, respectively.

In addition to the above, we have been investigating the feasibility of making a field usable device by placing a fused T with attached connectors in a box. In the initial design, a coupler was mounted in a box 7 x 2.5 x 0.5 in. This allowed adequate room for attaching connectors to the four ends of fused T. The final assembled device had an excess loss of 6 to 7 dB (approximately 3 dB/connector) and a coupling ratio of 3 dB. The connectors are in a developmental production stage at Hughes Connecting Devices Division at Irvine; connectors of the present design when made individually have losses less than 1 dB.

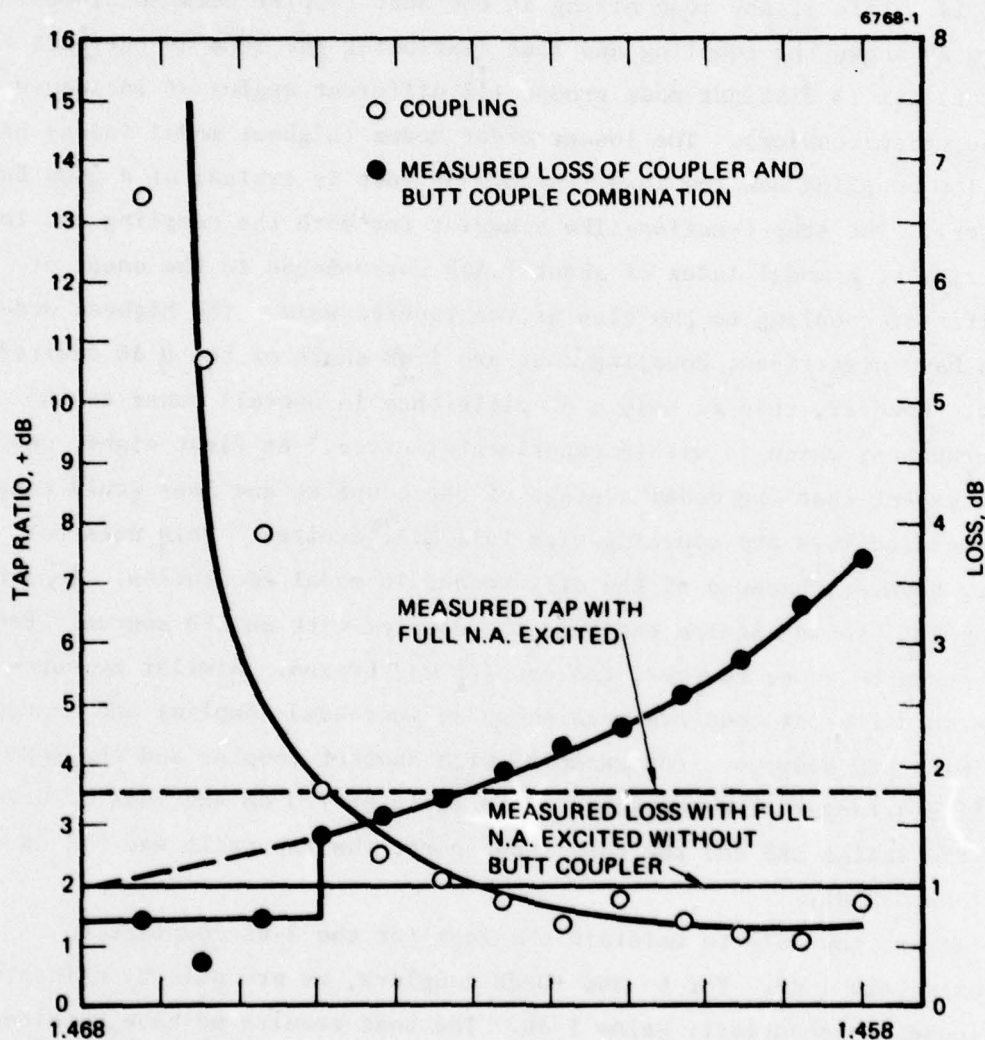


Figure 29. The measured loss and coupling versus mode index for a typical twisted and tapered T coupler. The measured loss with full NA excited was 1 dB; the measured tap ratio with full NA excited was 3.5 dB.

SECTION 4

MODAL CHARACTERISTICS OF STEP INDEX FIBERS

Modes in step index fibers may be selectively coupled to by varying the angle of incidence of the optical beam. Plane waves incident at large angles with respect to the fiber axis will excite high-order modes, while plane waves incident at small angles will excite low-order modes. Mode mixing will ultimately limit the distance over which these signals will remain in the modes in which they were launched. Experiments have shown that mode mixing in some commercially available step index fibers is very small and does not severely limit the length of a modally dependent communication system.

The experimental arrangement used to detect mode mixing in step index fibers is shown in Figure 30. A HeNe laser is used to launch plane waves into the fiber at a given angle θ with respect to the fiber axis. In a step index fiber with no mode mixing, the radiation should emanate from the far end of the fiber at the same angle θ . A camera is used to record the angular distribution of power emanating from the fiber end.

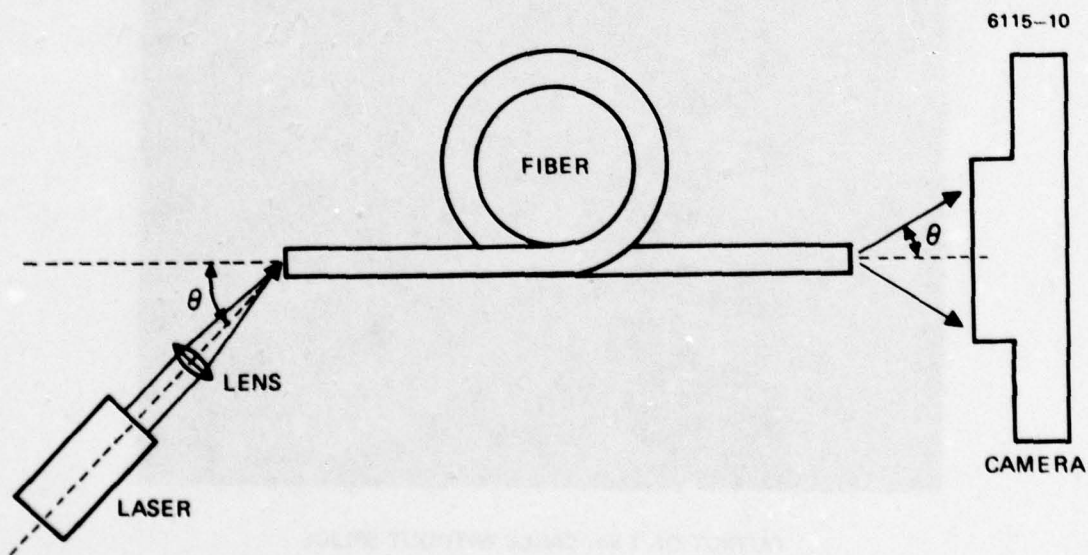
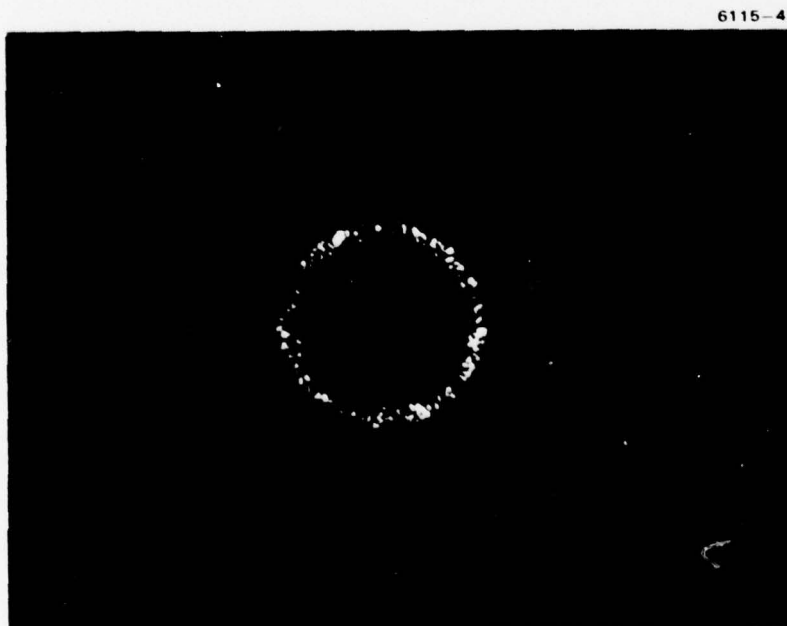


Figure 30. Experimental arrangement used to detect mode-mixing in step-index fibers.

Experiments have been done on a 1-km section of off-the-shelf cabled step index fiber produced by Corning Glass Works. The far-field radiation pattern observed when this fiber is illuminated at high angles is shown in Figure 31. Very little mode mixing is noted between these high-order (large angle) and low-order (small angle) modes in this 1 km long cabled fiber.

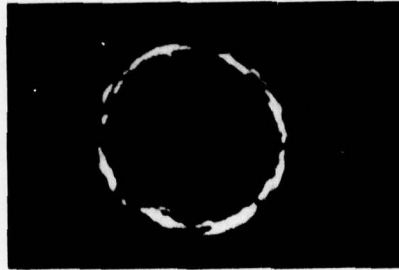
This fiber was also used to study the effect of a fiber splice on mode mixing. First, energy was launched into high-order modes of a short section of the fiber. The output is shown in Figure 32(a). Then another short section of fiber was spliced by butting it against the first in an embossed groove connector. If the fiber connection was carefully aligned, then the pattern coming out of the combined fiber is as shown in Figure 32(b). This illustrates that a good fiber connector need not introduce any serious mode mixing in step-index fibers. However, a poor splice will result in a large amount of mode mixing, as is evident in Figure 32(c), where the two fibers were slightly misaligned.



OUTPUT OF 1 km CABLE WITHOUT SPLICE

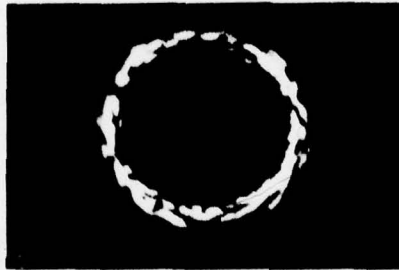
Figure 31. Far-field radiation pattern observed from 1-km cabled Corning step index fiber when the high-order modes are excited at the input.

6115.38



OUTPUT OF
SHORT PIECE
OF FIBER

6115.39



GOOD
SPLICE

6115.40



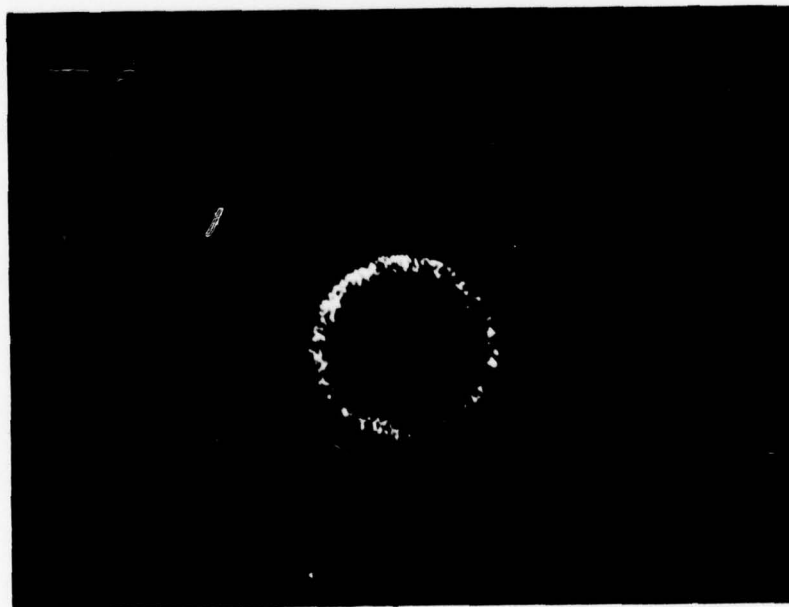
POOR
SPLICE

Figure 32.
Far field radiation pattern observed from (a) short piece of fiber without a connector, (b) short piece of fiber with a good connector, (c) short piece of fiber with a poor connector. In all cases, the high-order modes of the fiber are excited at the input.

In Figure 33, the output from the 1-km cabled fiber is shown with a splice connection at the input end. Some mode mixing is seen, but overall the ring-shaped pattern is preserved.

A simple technique for the determination of mode conversion coefficients in multimode step index fibers was recently described.⁶ In the experiment, a collimated input beam is incident on the fiber at an angle θ . For an ideal fiber of no mode mixing, the far-field pattern of the light emanating from the fiber output will be a ring with the cone angle equal to the incident angle. The width of the ring is then determined by the divergence of the input beam. If there is mode mixing in the fiber, the ring pattern will become blurred, and the intensity distribution will peak at an angle smaller than the incident angle. As the incident angle is decreased, the power in the center begins to increase as a result of the intermode coupling, so that eventually the ring pattern disappears and the intensity distribution peaks at the center.

6115-42



OUTPUT OF 1 km FIBER WITH SPLICE

Figure 33. Far-field radiation pattern observed from 1-km cabled Corning fiber with a splice connection at the input.

The relation between the mixing coefficient D and the fiber length z needed for the transformation of the ring distribution, due to a mode propagating at an angle θ_m with respect to the fiber axis, into a solid circle intensity peaked at the center is given by⁶

$$\log \theta_m = \frac{1}{2} \log z + \log 2D^{1/2} \quad (12)$$

This relation can be rewritten in a simpler form:

$$\theta_m^2 = 4D z \quad (13)$$

The relation was derived for fibers exhibiting weak mode mixing, with the assumption that the mode spectrum is continuous and that mode coupling occurs only between nearest neighboring modes. Using this technique, the normalized mode coupling efficiency D for the 1 km long cabled fiber was calculated. A value of

$$D = 5.6 \times 10^{-7} \frac{\text{rad}^2}{\text{m}} \quad (14)$$

was found. From this value, the minimal fiber length necessary for complete mode mixing can be computed. This case will be calculated for the largest possible incident mode (i.e., that corresponding to an off axis angle given by the numerical aperture of the fiber). Thus, substituting

$$\theta_m = \text{N.A.} \approx 0.2 \text{ rad} \quad (15)$$

and Eq. 14 into Eq. 13 yields

$$(z)_{\min} \approx 18 \text{ km} \quad (16)$$

Therefore, fiber longer than 18 km is necessary for complete mode mixing. Thus, in properly fabricated and cabled fibers, mode mixing need not limit short and medium length modally multiplexed systems.

SECTION 5

FIBER PARAMETER STUDIES WITH THE OTDR

In principle, the OTDR allows one to study mode coupling lengths, total attenuation coefficients, and both discrete and distributed scattering. If, for example, the fiber contains an imperfection that results in a localized attenuation, this technique allows determining both the magnitude and position of the discontinuity. The technique also provides an easy way to check both cable length and insertion loss. This section presents a theoretical treatment of the OTDR, summarizes the changes made to the original instrument, discusses different techniques that were investigated, and summarizes the experimental data gathered during the contract.

A. THEORETICAL TREATMENT OF THE OTDR

This discussion of the OTDR, which is included for completeness, describes work performed on Hughes IR&D funds and published before the start of this contract. This work is the theoretical basis on which this technique relies.

The optical power at a propagation distance X in a fiber waveguide can be expressed as

$$\begin{aligned} P(X) &= P(X_1) \exp \left[- \int_{X_1}^X \alpha(x) dx \right] \\ &= P(X_1) \exp [-\bar{\alpha}(X - X_1)] \quad , \end{aligned} \quad (17)$$

where $\alpha(x)$ is the loss coefficient (which, in general, may be position-dependent), and $P(X_1)$ is the power in the fiber at position X_1 . If the loss coefficient is constant, the above expression reduces to Beer's law. The conventional technique for determining the attenuation of an optical fiber is to measure the optical power emanating from the end of a fiber

of length X_2 , cut the fiber, and measure the power at length X_1 . The attenuation coefficient measured in this fashion is

$$\bar{\alpha} = \frac{1}{X_2 - X_1} \int_{X_1}^{X_2} \alpha(x) dx \quad . \quad (18)$$

The average attenuation coefficient $\bar{\alpha}$ is, therefore, dependent on the measurement length $X_2 - X_1$. The loss coefficient dependence on propagation length is a result of differential modal attenuation and modal mixing.

The optical power at a distance X from the fiber end can be written as

$$P(X) = P(0) \exp \left[- \int_0^X \alpha'(x) dx \right] \quad , \quad (19)$$

where $\alpha'(x)$ may differ from $\alpha(x)$ because launched modes are different from those launched in the conventional insertion loss technique. $P(0)$ is the power launched into the fiber. Assuming that the scattering is independent of the modal characteristics of the light and is constant at all points along the fiber, the power scattered in the reverse direction at X is given by $P_R(X) = SP(X)$, where S is the fractional part of light scattered and trapped in the fiber going in the reverse direction. The power backscattered at X , and detected at the detector, can be expressed as

$$P_d(X) = P_R(X) \exp \left[- \int_0^X \alpha''(x) dx \right] \quad , \quad (20)$$

where $\alpha''(x)$ is the loss coefficient for the backscattered light. By making the appropriate substitution for $P_R(X)$, the detected backscattered power is

$$P_d(X) = SP(0) \exp \left\{ - \int_0^X [\alpha'(x) + \alpha''(x)] dx \right\} . \quad (21)$$

The data obtained from the OTDR waveform can be used to determine an average attenuation coefficient, defined as

$$\bar{\alpha} \equiv \frac{-[\ln P_d(X) - \ln P_d(X_1)]}{2(X - X_1)} , \quad (22)$$

where $P_d(X)$ is the detected backscattered power from point X in the fiber. Substituting the proper expression for $P_d(X)$ into the above definition results in

$$\bar{\alpha} = \frac{\int_{X_1}^X [\alpha'(x) + \alpha''(x)] dx}{2(X - X_1)} . \quad (23)$$

The scattering function S can also be determined from first principles. The predominant scattering mechanism in glass fibers is Rayleigh scattering from microscopic variations in the local dielectric constant associated with the frozen thermal fluctuations of the constituent atoms.⁷ This coefficient is

$$\alpha_s = \frac{8\pi^3}{3\lambda^4} (n_{\text{core}}^2 - 1) kT\beta , \quad (24)$$

where k is Boltzmann's constant, T is the transition temperature at which the fluctuations are frozen into the glass, and β is the isothermal compressibility of the material at that temperature.⁷ At $\lambda = 0.9 \mu\text{m}$, α_s is 1.2 dB/km for fused silica.

The light intensity remaining in a beam of initial intensity I_0 at any point x along the fiber is

$$\begin{aligned} I_s(x) &= I_0 e^{-\alpha_t x} \\ &= I_0 e^{-\alpha_s x} e^{-\alpha_a x}, \end{aligned} \quad (25)$$

where α_t , the total fiber attenuation coefficient, is composed of α_s (the scattering coefficient), and α_a (the absorption coefficient). The light intensity scattered from the beam as it travels along the fiber from x to $x + dx$ is given by

$$dI_s(x) = I_0 \alpha_s e^{-\alpha_t x} dx. \quad (26)$$

This equation can be used to calculate the light intensity backscattered from a beam in a highly multimode fiber, provided that an additional geometrical factor is used to account for light trapped in the fiber. The distribution of the Rayleigh scattered light is isotropic. The portion of this light trapped by the fiber is given by the geometrical factor

$$G = \frac{1}{2} (1 - \cos \theta), \quad (27)$$

where θ is the angle corresponding to the numerical aperture (NA) inside the fiber. For small NA fibers, the geometrical factor becomes

$$G \approx \frac{NA^2}{2n_1^2}. \quad (28)$$

The intensity I_B backscattered from a beam of light of length L within a fiber is given by

$$\begin{aligned}
 I_B &= \int_0^L I_o G \alpha_s e^{-\alpha_t x} dx \\
 &= I_o G \frac{\alpha_s}{\alpha_t} \left(1 - e^{-\alpha_t L} \right) .
 \end{aligned} \tag{29}$$

The scattering fraction S is the ratio of I_B to I_o :

$$S = G \frac{\alpha_s}{\alpha_t} \left(1 - e^{-\alpha_t L} \right) . \tag{30}$$

If the probe pulse length within the fiber is small compared to the total absorption coefficient we may approximate the scattering fraction as

$$S \approx \left(\frac{NA}{2n_1} \right)^2 \alpha_s L . \tag{31}$$

This same result was obtained in a more general way by Kapron et al.⁸ We have also verified this theory in the laboratory.

B. DETECTED BACKSCATTERED POWER CALCULATIONS

The previous section describes the theoretical basis used to analyze waveforms using the OTDR. This section is intended to provide an indication of the absolute power levels backscattered into the OTDR detector. We begin by considering the following equation for the detected power $P_d(z)$:

$$P_d(z) = C_{in} C_o k S e^{-2\bar{\alpha}_T z} P_o , \tag{32}$$

where

C_{in} = input coupling efficiency

C_o = output coupling efficiency

k = insertion loss of the directional coupler

P_o = peak laser power

$\bar{\alpha}_T$ = mean total attenuation = $\alpha_s + \alpha_a$

α_s = scattering loss

α_a = absorption loss

z = position of the pulse within the fiber

$$S = \left(\frac{NA}{2n} \right)^2 \alpha_s \frac{c}{n} \tau$$

τ = pulsewidth .

If a taper is used to couple light into the fiber typical values for the various parameters are

$$C_{in} = -26 \text{ dB}$$

$$C_o = 0 \text{ dB}$$

$$k = -1.5 \text{ dB}$$

$$P_o = +33 \text{ dBm}$$

(33)

$$\alpha_s = 1.22 \text{ dB/km}$$

$$NA = 0.16$$

$$n = 1.48 .$$

Then in units of dBm

$$P_d(z) = 34.4 + 10 \log \tau - 2 \bar{\alpha}_T z . \quad (34)$$

This result is plotted in Figure 34 as a function of pulsewidth τ and total attenuation coefficient $\bar{\alpha}_T$. As an example of the use of this figure, we consider the particular case of 10 nsec pulses. These pulses require about 100 MHz of detection bandwidth. For a S/N of 2 dB, an optimized avalanche photodiode receiver requires about -60 dBm of signal power. Figure 34 shows that the present technique will allow us to measure approximately 700 m of low-loss (10 dB/km) fiber, but only 400 m of medium loss (20 dB/km) fiber.

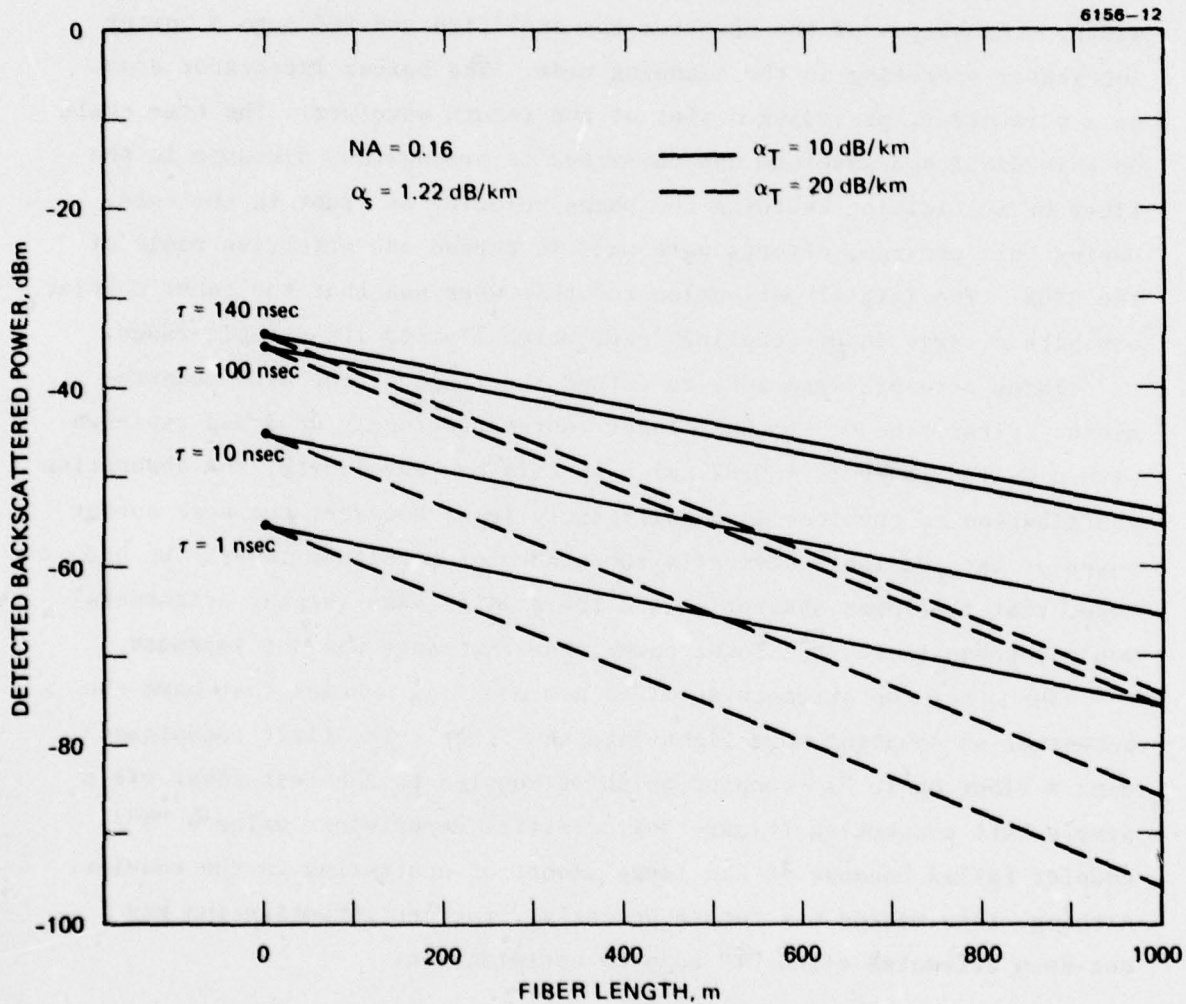


Figure 34. Detected signal levels versus fiber length, loss, and probe pulse length for backscattering experiments.

C. EXPERIMENTAL TECHNIQUES

The OTDR experimental arrangement used at the beginning of this contract is shown in Figure 35. A 130-nsec wide pulse of light from a GaAs injection laser was coupled into the fiber using a tapered fiber coupler.⁹ (Typical tapered fiber couplers have taper angles less than 1° and are approximately 2 mm long.) Light traveled down the fiber and was scattered from every point along the fiber. Some of this scattered light was trapped within the fiber and guided toward the detector. The scattered waveform was detected by a photodetector with a 50-MHz bandwidth. The output of the detector was amplified and fed into a boxcar integrator operating in the scanning mode. The boxcar integrator drove an x-y recorder, providing a plot of the return waveform. The time scale on this displayed waveform was converted to propagation distance in the fiber by multiplying by twice the phase velocity of light in the core. During this program, efforts were made to extend the effective range of the OTDR. The initial motivation for this work was that the taper coupler exhibits a large input coupling loss, which limited its dynamic range.

Three attempts were made to extend the range of the OTDR measurements. First, the 0.9- μm GaAs laser source previously used was replaced with a GaAlAs laser ($\lambda = 0.82 \mu\text{m}$). At this new wavelength, the absorptive contribution to the loss is significantly less; however, the peak output power of the available device is two orders of magnitude lower. We had hoped that the lower absorption and the smaller size (higher brightness) would compensate for the lower power, but the range was not improved.

The other two attempts involved new coupling schemes that have the potential of coupling more light into the fiber. The first technique uses a fiber optic "T" coupler which is coupled to the test fiber via a simple butt connection (Figure 36). Initial experiments using a "T" coupler failed because of the large amount of scattering in the coupler. Although this method has future potential, further investigation has not been attempted since "T" coupler optimization.

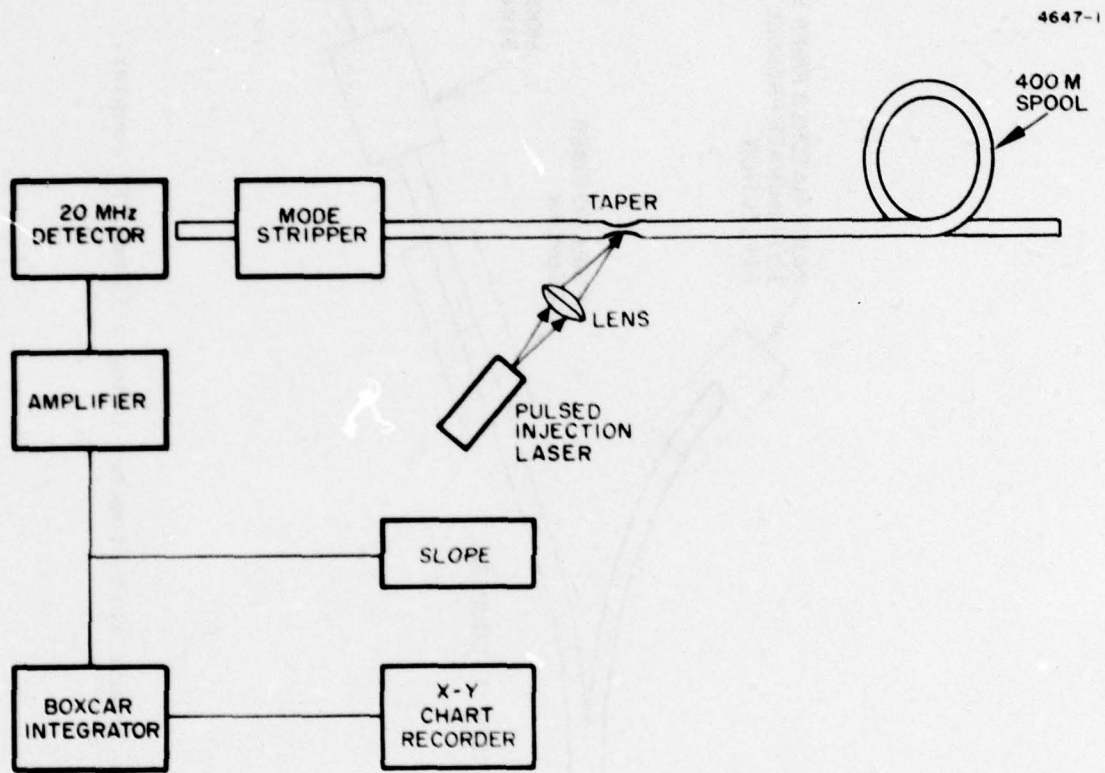


Figure 35. Experimental arrangement used to record return optical waveform is shown here.

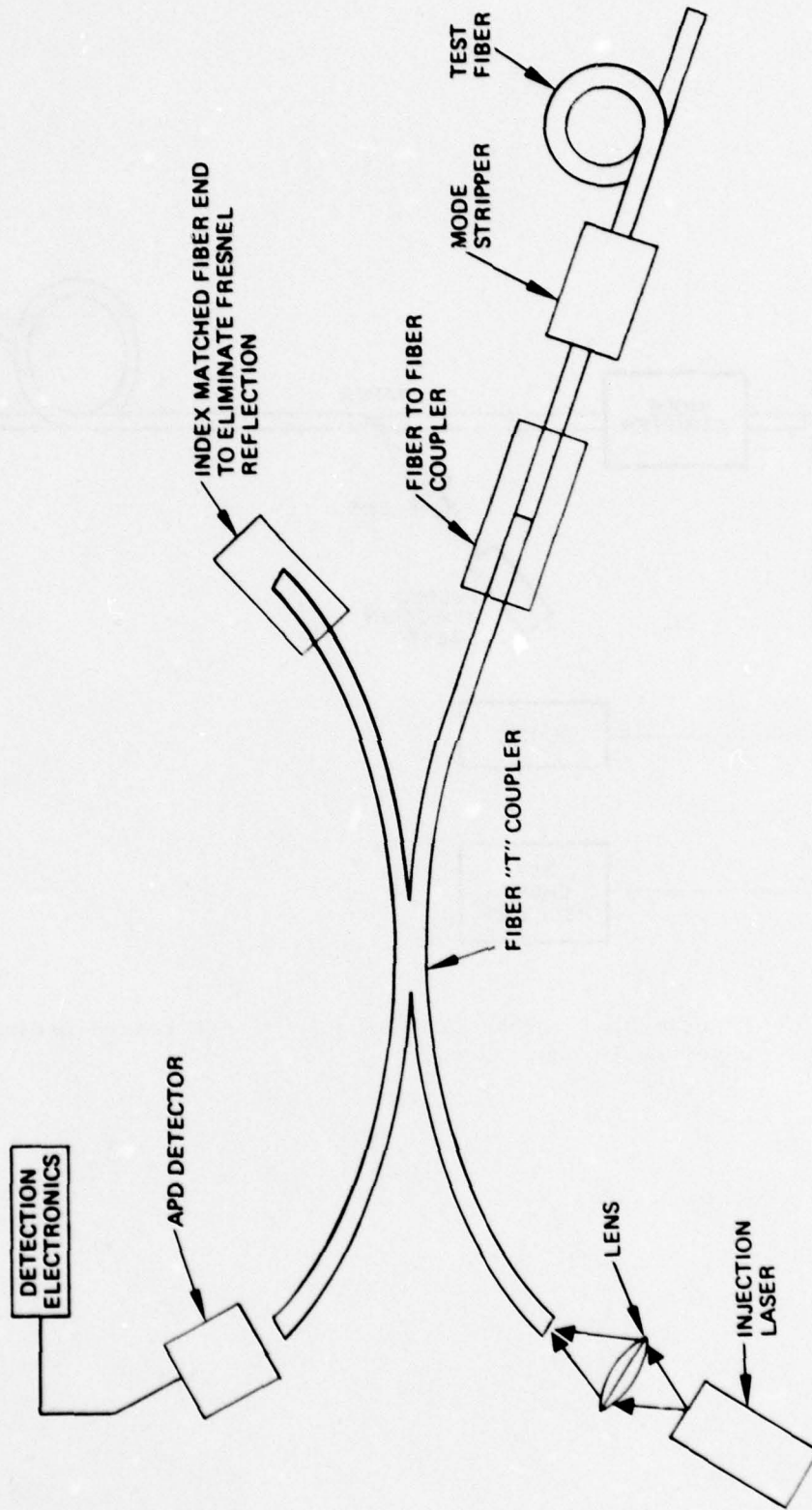


Figure 36. Optical time domain reflectometer using a fiber "T" coupler.

The third technique was more successful; it is the present sampling arrangement used in the OTDR. This technique is illustrated in Figure 37. An injection laser is collimated with a high NA microscope objective. This light is then polarized, parallel to the plane of incidence of the beam splitter by a Glan-prism polarizer. The beam splitter is an ordinary 225- μm -thick pellicle. The angle of the pellicle is chosen so that it optimizes the throughput of the p polarization and the reflection of the s polarization. This light is then focused on the fiber end with another microscope objective. The numerical aperture and focal length of this lens are chosen to match the fiber. The fiber itself is precisely located using a trumpet alignment tube, thus giving a quick and convenient way to exchange fibers. The optical power backscattered within the fiber is recollimated and reflected off the beam splitter. A crossed Glan-prism polarizer is used to select the s polarization to the block's spurious reflections (such as the 4% Fresnel reflection from the fiber end), which are p polarized. Finally, the backscattered light from the fiber is focused on an avalanche photodiode, which is used to detect the signal. Calculations have shown that the transmission and reflection losses of the beam splitter are less than -3 dB when compared to the optimal case where the input laser beam is totally transmitted and backscattered beam totally reflected.

We are detecting a polarization rotated by 90° from the input polarization. Since, in multimode glass fibers, the input light is depolarized within a short distance, much less than the present resolution of the OTDR (≈ 26 m), the OTDR measurements are unaffected by the polarization-sensitive detection. Also, because the Rayleigh-scattered light is itself depolarized, this measurement technique will be useful, even in single mode¹⁰ or liquid core¹¹ fibers when the polarization is preserved over long lengths.

Figure 38 shows the backscattered signal from a 4-km long graded-index multimode silica fiber obtained using this crossed polarizer technique. The entire return signal can be seen in Figure 38(a). The Fresnel reflection from the launch end of the fiber has been reduced to within 5.5 dB of the Rayleigh scattered return. This demonstrates the

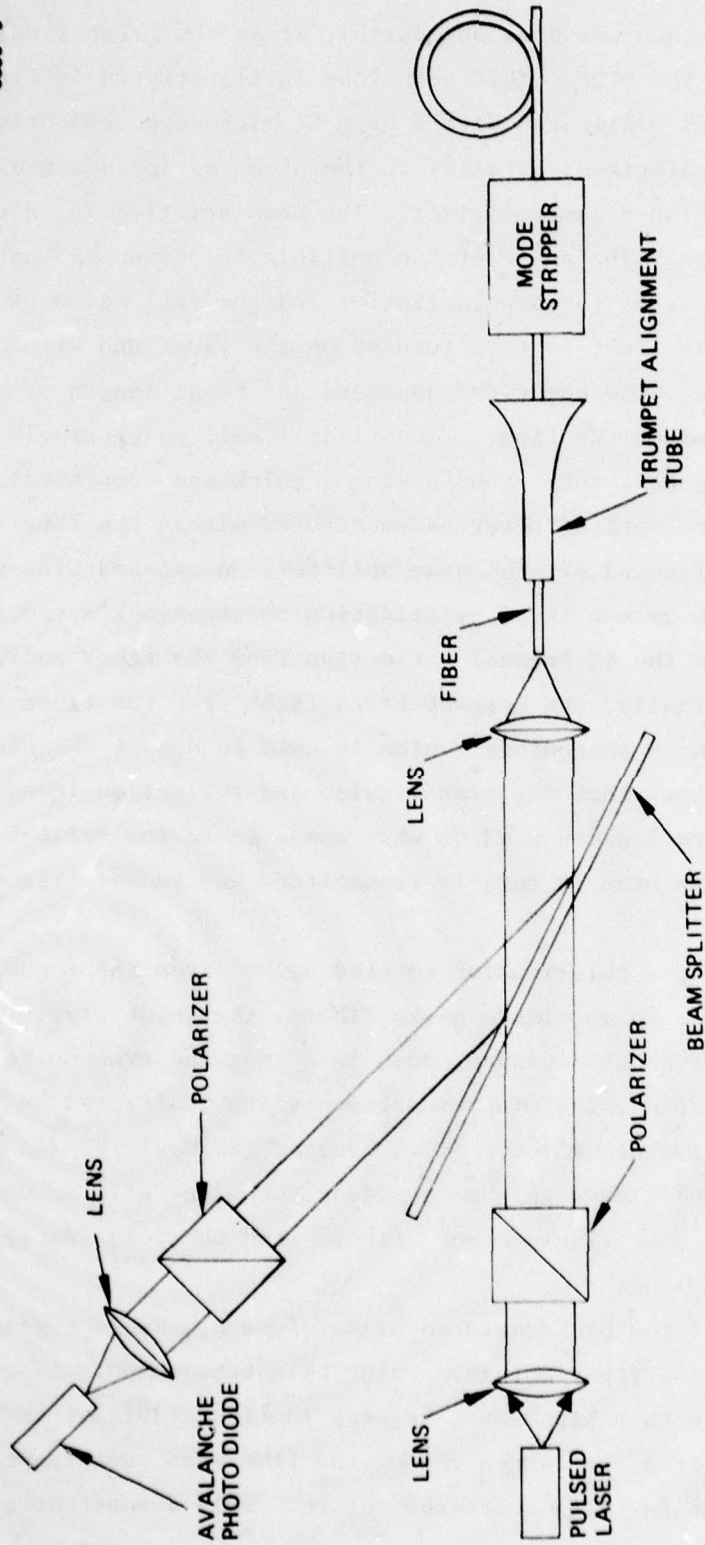


Figure 37. OTDR assembled using an external beamsplitter and crossed polarizers.

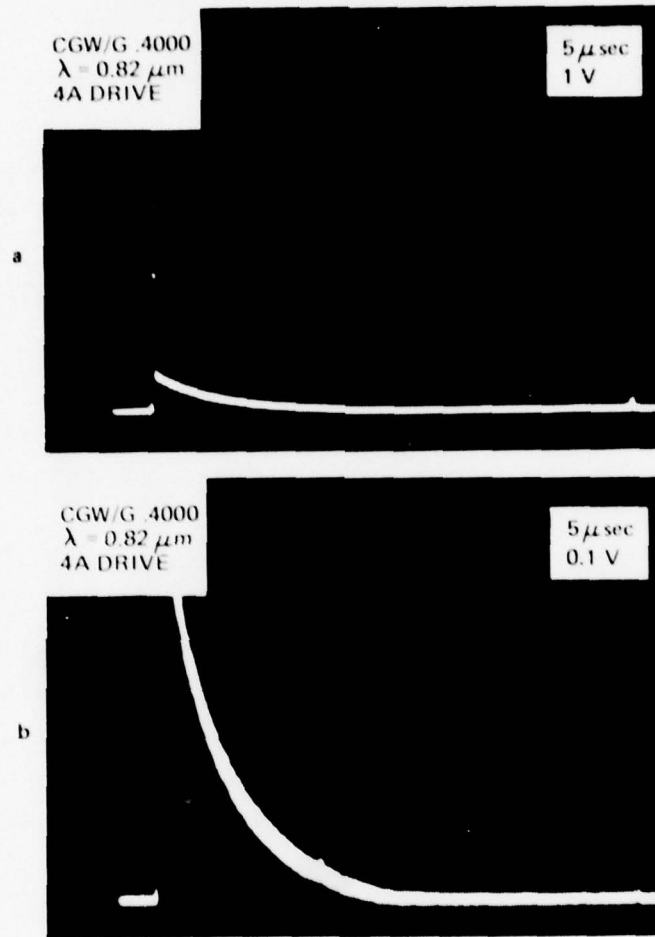


Figure 38. Oscillograms of the deflected back-scattered light from a 4-km fiber using the external beamsplitter technique.

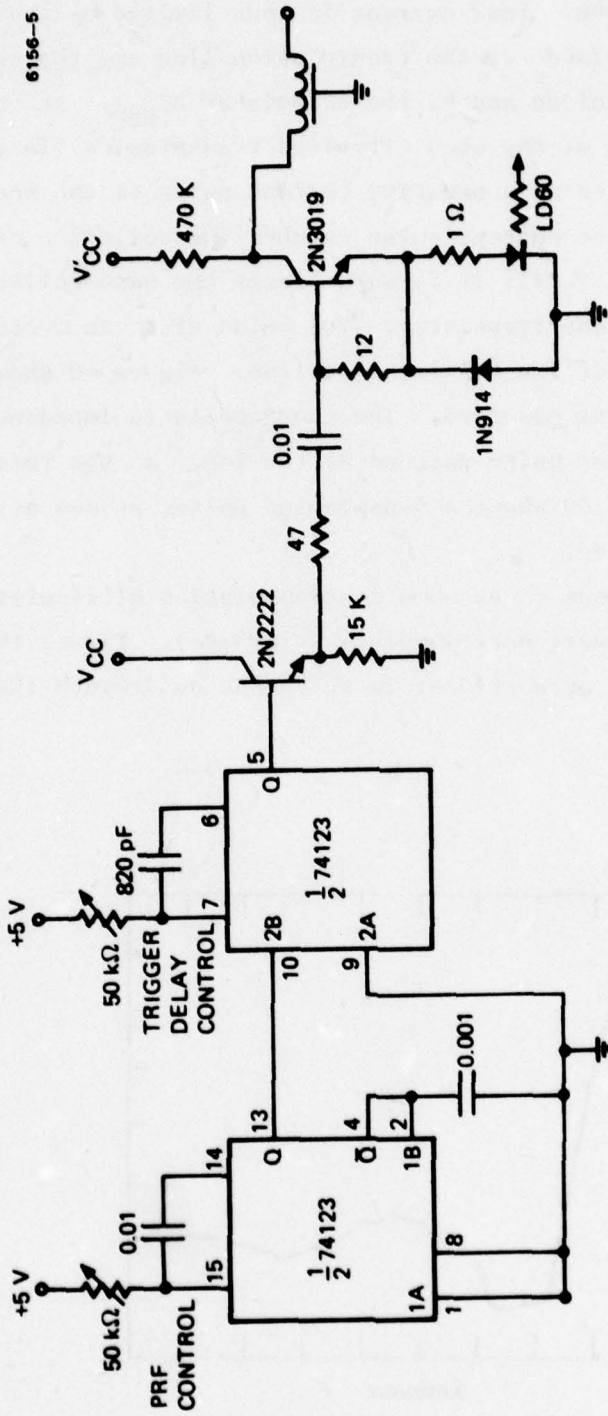
effectiveness of the crossed polarizer technique for blocking reflections in the launching apparatus. Also evident in Figure 38(a) is the Fresnel reflection from the fiber end (4.2 km away). Figure 38(b) is a 10x enlargement of Figure 38(a). The exponential decay of the Rayleigh light is clearly visible in Figure 38(b). A small imperfection in the fiber is also visible in Figure 38(b). This is evident by the small blip in the Rayleigh return approximately 1/3 of the way to the fiber end (≈ 1.5 km down the fiber). Unfortunately, we are still only able to see a Rayleigh return from slightly over 2 km of fiber using the 0.82- μm OTDR. Although this work was successful in coupling additional light into the fiber, it was still not possible to measure the total length of the 4-km fiber using semiconductor lasers. To overcome this problem, an OTDR was built that used a Nd:YAG laser. The coupling technique illustrated in Figure 37 was modified by using a single Glan-prism polarizer to replace the two polarizers and the beam splitter.

A high-speed, high-peak-current pulse generator for use as a laser diode driver was developed. With this device incorporated into the TDR, pulses as narrow as 1 nsec are available to probe the test fiber. The avalanche transistor technique is used for generating these high current, very short pulses.^{12,13} Figure 39 is a schematic of the pulse generator. The 74123 dual one shot multivibrator is used to control the pulse repetition frequency and to provide a variable trigger delay for synchronizing the experiment. An emitter follower (2N2222) amplifies the trigger current and drives the avalanche transistor (2N3019). When the triggering signal reaches the avalanche transistor, it breaks down, placing a negative voltage step of amplitude

$$V = V'_{CC} - BV_{CER} \quad (35)$$

on the transmission line. BV_{CER} is the collector-to-emitter breakdown voltage when the base is returned to the emitter through a resistance R . Since the initial current in the transmission line is zero, this voltage step is accompanied by a current step of amplitude

$$I = V/(Z_0 + Z_L) \quad , \quad (36)$$



6156-5

Figure 39. Laser diode pulse generator employing an avalanche transistor.

where Z_0 is the characteristic impedance of the transmission, and Z_L is the impedance of the load. Peak current is thus limited by the sum of the characteristic impedance of the transmission line and the series impedance of the laser diode and by the transistor BV_{CER} . At the time τ , when it reaches the end of the open circuited transmission line, this current step is reflected as a negative current pulse of the same amplitude. When this negative current pulse reaches the collector of the avalanche transistor ($t = 2\tau$), it forward biases the base-collector junction, shutting off the transistor. The pulse width is controllable by changing the length of the transmission line. Figure 40 shows a typical collector current waveform. The characteristic impedance of the transmission line was not quite matched by the load, as the reflection shows. Although Figure 40 shows a 5-nsec-wide pulse, pulses as short as 1 nsec have been obtained.

Two related phenomena cause some instrumentation difficulties when probing the fiber with very narrow pulses (~10 nsec). First, the scattered detected power is proportional to the probe pulsewidth (Eq. 32).

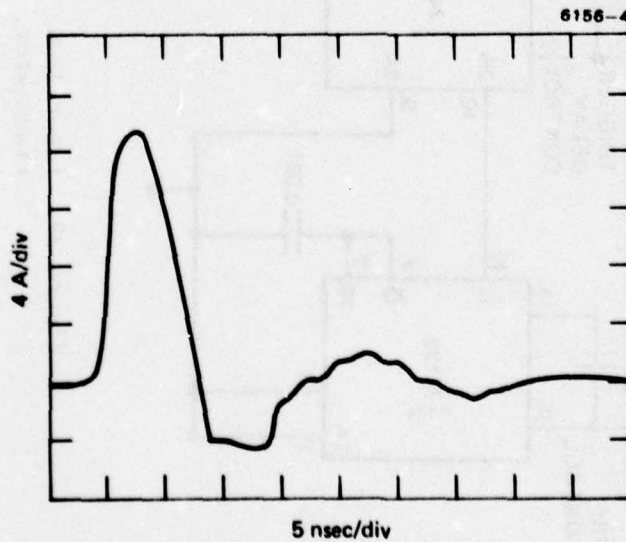


Figure 40. Collector current waveform.

Consequently, a higher power source must be used in these experiments to preserve the same system dynamic range (i.e., so that we can see through the same length of fiber). Second, the peak amplitude of the Fresnel reflections that occur in the experiment depends only on the peak power of the source. Hence, the increase in source power required to maintain system dynamic range incurs the penalty of increased Fresnel reflection, which can cause detector-preamplifier saturation.

D. BACKSCATTERING EXPERIMENTS

The taper coupler initially used in the backscattering experiments¹⁴ provided sufficient directionality to eliminate the need for either electrical¹⁵ or optical gating to prevent detector saturation. However, a rather complex modal distribution, which affects the measured attenuation coefficient in fibers with little mode mixing, was launched. This problem was circumvented by incorporating a mode scrambler, which converts the input distribution into a distribution more closely approximating the steady-state distribution. An experiment was performed to investigate the launch characteristics of the backscattering measurement apparatus. The experimental arrangement used is shown in Figure 41. A 130-nsec laser pulse was launched into the taper coupler fabricated in a short length of fiber. The short fiber was then connected using an embossed groove coupler to a 1-km section of cabled step-index fiber purchased from Corning. Since a good embossed groove coupler does not cause mode mixing, the modal distribution launched into the taper coupler was that launched into the 1-km long cable. A radial scan, of the angular radiation pattern emanating from the far end of the 1-km fiber with no mode mixer is shown in Figure 42 (Trace A). Trace B in Figure 42 is a scan obtained at the far end of the 1-km fiber after the modes were intentionally mixed at the input with a mode mixer. The mode mixer consists of an array of No. 18 gauge lacquer-coated wires placed adjacent to each other. The total length of this periodic array was 2.5 cm. After placing the fiber on the array, a rubber pad was placed over the fiber and a 200 g weight placed on top of it.

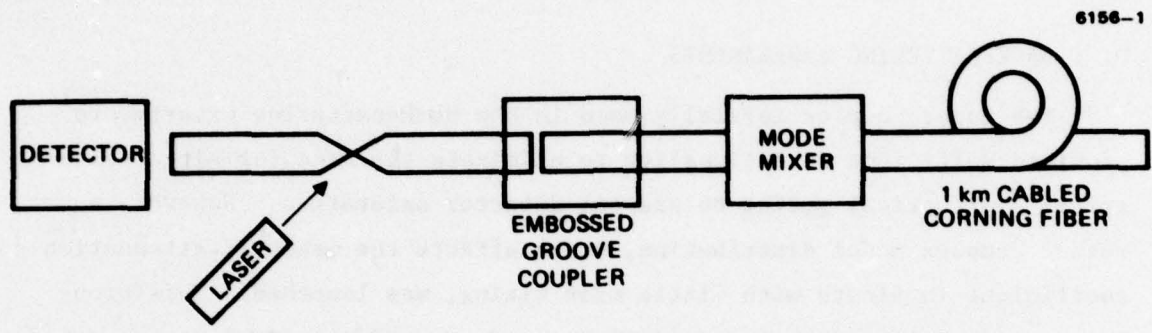


Figure 41. Experimental set-up used to investigate the effect of the mode mixer on the backscatter experiments.

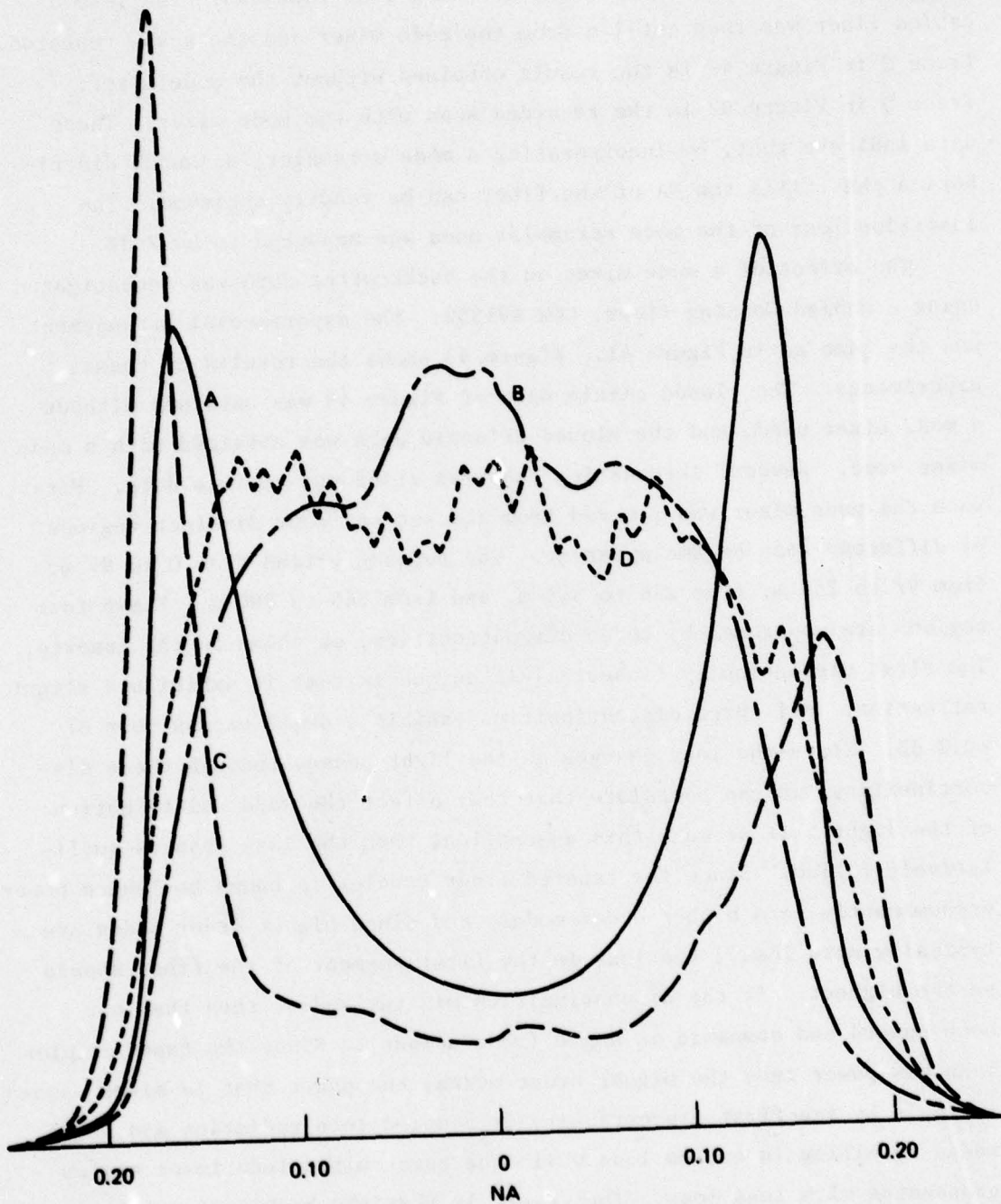


Figure 42. Modal content of CGW 491352. Power distributions were measured at a distance of 30 cm from the cleaved end of the fiber. (A. 1 km no mode mixer, B. 1 km with mode mixer, C. 1/2 m no mode mixer, D. 1/2 m mode mixer.)

Mode mixing was caused by the microbending that resulted. The 1-km cabled fiber was then cut 1 m from the mode mixer and the scans repeated. Trace C in Figure 42 is the result obtained without the mode mixer; Trace D in Figure 42 is the recorded scan with the mode mixer. These data indicate that, by incorporating a mode scrambler, a launch distribution that fills the NA of the fiber can be readily achieved. The insertion loss of the mode scrambler used was measured to be 2 dB.

The effect of a mode mixer on the backscatter data was investigated using a cabled Corning fiber, CGW 491352. The experimental arrangement was the same as in Figure 41. Figure 43 shows the results of these experiments. The closed circle data of Figure 43 was obtained without a mode mixer used, and the closed triangle data was obtained with a mode mixer used. Several interesting features stand out in this data. First, when the mode mixer was removed from the set-up, four distinct regions of different loss became apparent. The regions extend from 0 to 97 m, from 97 to 256 m, from 256 to 345 m, and from 345 to 980 m. These four regions are separated by three discontinuities, as shown in the inserts. The first discontinuity (insert A) is unique in that it exhibits a slight reflection. All three discontinuities exhibit a small excess loss of ~ 0.2 dB. Since the loss changes as the light passes through these discontinuities, we can postulate that they affect the modal distribution of the light. If we make this assumption, then the loss changes qualitatively follow. Since the tapered fiber coupler is known to launch power predominantly into higher order modes, and since higher order modes are typically more lossy, the loss in the first segment of the fiber should be the highest. If the discontinuities mix the modes, then they mix both upward and downward in angle (mode number). Since the taper coupler launches power into the higher order modes, the power that is mixed upward in angle by the first discontinuity is coupled into radiation and leaky modes resulting in excess loss while the power mixed into lower angles propagates with less loss. The result is that the backscatter data in the second region is expected to exhibit excess loss at the discontinuity followed by a region of lower loss. A second mode-mixing discontinuity is again expected to couple the new lower order mode distribution

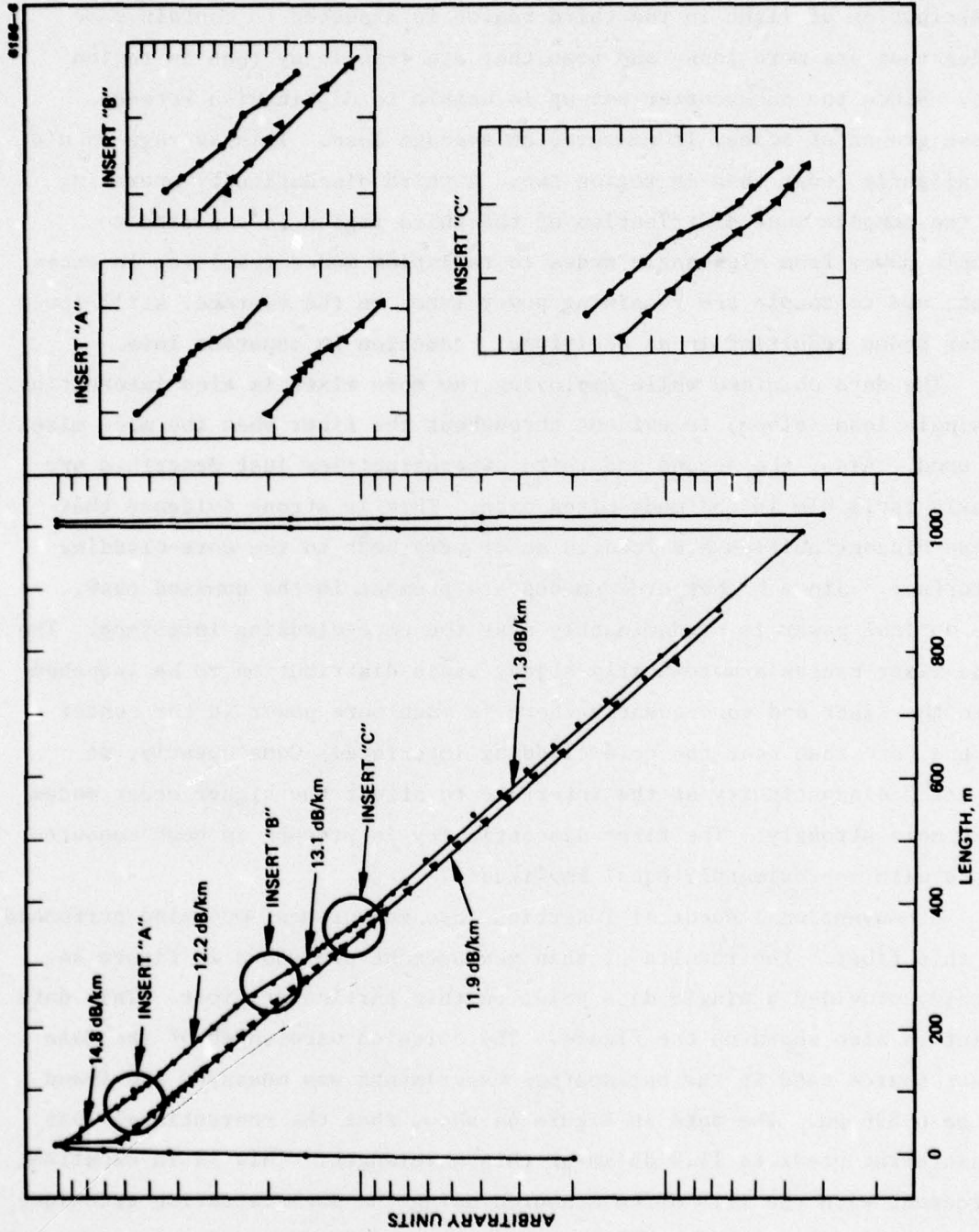


Figure 43. Backscattering data from CGW 491352.

of the second region into higher and lower order modes. Some power is lost due to coupling to radiation modes (excess loss) and the resulting distribution of light in the third region is expected to contain some modes that are more lossy and some that are less lossy than in region two. Since the backscatter set-up is unable to distinguish between these groups of modes, it measures an average loss. This average should be slightly lower than in region two. A third discontinuity operating on the complex mode distribution of the third region is expected to couple power from high-angle modes to radiation modes resulting in excess loss, and to couple the remaining power into, on the average, still lower order modes resulting in an additional reduction in apparent loss.

The data obtained while employing the mode mixer is also interesting. A single loss (slope) is evident throughout the fiber when the mode mixer is used. Also, the second and third discontinuities just described are nearly invisible in the mode-mixed case. This is strong evidence that these discontinuities are located at or very near to the core-cladding interface. Since higher order modes are present in the unmixed case, the optical power is predominantly near the core-cladding interface. The mode mixer causes a more nearly steady state distribution to be launched into the fiber and consequently there is much more power in the center of the core than near the core-cladding interface. Consequently, we expect a discontinuity at the interface to affect the higher order modes much more strongly. The first discontinuity is present in both measurements with approximately equal amplitude.

A conventional spectral insertion loss measurement was also performed on this fiber. The results of this measurement are shown in Figure 44. Corning provided a single data point on this particular fiber. This data point is also shown on the figure. The emission wavelength of the GaAs laser source used in the backscatter experiments was measured and found to be 0.896 μm . The data in Figure 44 shows that the conventional loss measurement predicts 11.8 dB/km at this wavelength. This is in excellent agreement with the 11.9 dB/km measured using the backscattering technique and a mode mixer. These experimental results reconfirm the measurement accuracy of this technique.

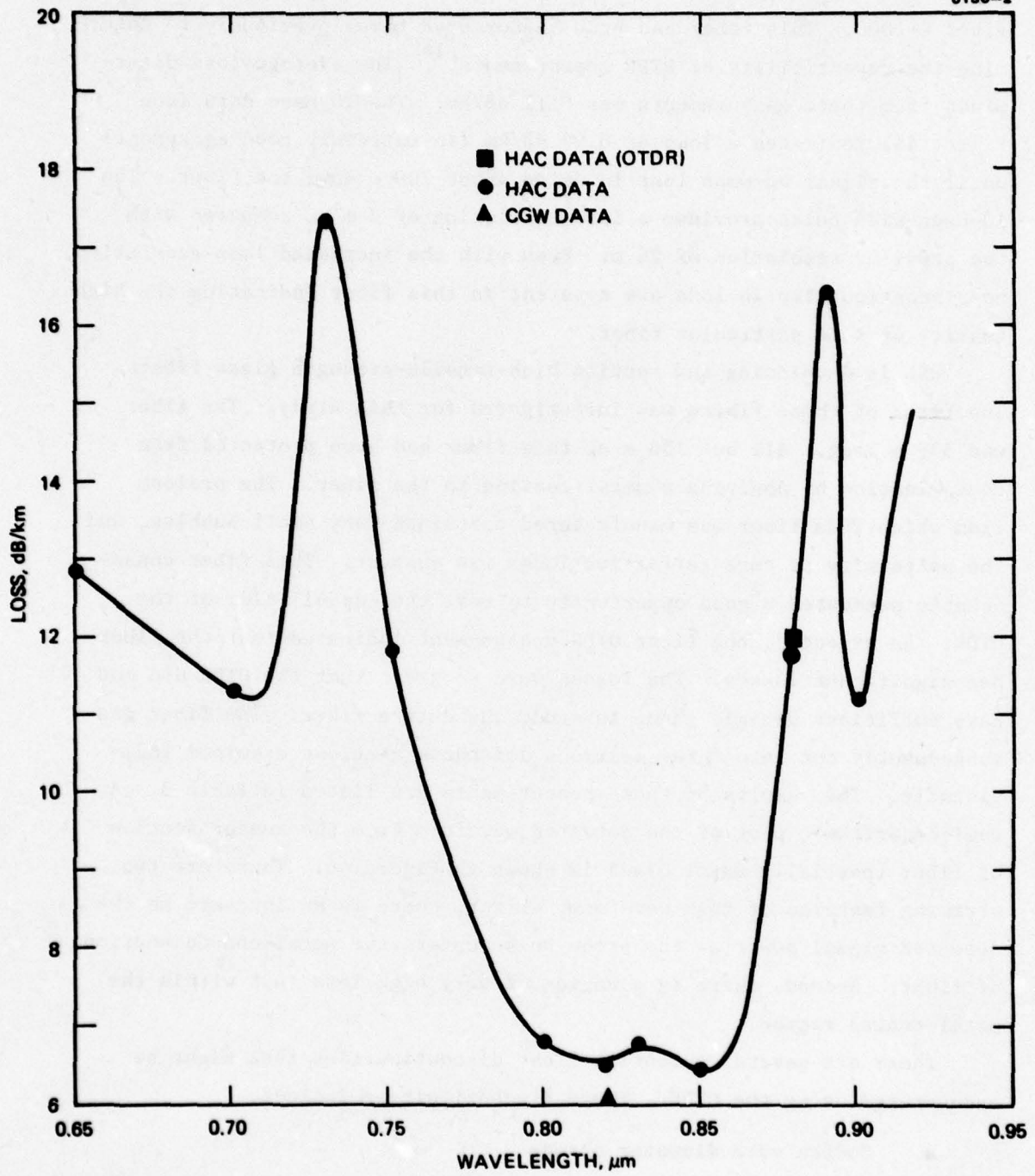


Figure 44. Spectral loss measurement data on CGW 491352.

A 10-nsec-wide pulse was used to investigate the loss in Corning fiber G-1000. This fiber had been measured 48 times previously to determine the repeatability of OTDR measurements.¹⁴ The average loss determined from these measurements was 8.11 dB/km. The 10 nsec data (see Figure 45) indicates a loss of 8.09 dB/km (in extremely good agreement) until the signal becomes lost in noise about 700 m down the fiber. The 10-nsec-wide pulse provides a loss resolution of 2 m as compared with the previous resolution of 26 m. Even with the increased loss resolution, no discontinuities in loss are apparent in this fiber indicating the high quality of this particular fiber.

HRL is developing and testing high-tensile-strength glass fibers. The first of these fibers was investigated for this study. The fiber was 539 m long. All but 156 m of this fiber had been protected from contamination by applying a metal coating to the fiber. The preform from which this fiber was manufactured contained many small bubbles, and the uniformity of core refractive index was suspect. This fiber consequently presented a good opportunity to test the capabilities of the OTDR. As expected, the first OTDR measurement indicated that the fiber had significant losses. The losses were so great that the OTDR did not have sufficient dynamic range to study the entire fiber. The fiber was subsequently cut into three sections and these sections examined individually. The results of these measurements are listed in Table 3. A semi-logarithmic plot of the detected waveform from the center section of fiber (partially metal clad) is shown in Figure 46. There are two striking features of this waveform. First, there is an increase in the detected signal power as the probe pulse enters the metal-coated section of fiber. Second, there is a region of very high loss just within the metal-coated region.

There are several potential fiber discontinuities that might be encountered using the OTDR. These discontinuities include:

- Sudden core diameter change
- Scattering coefficient change
- NA change

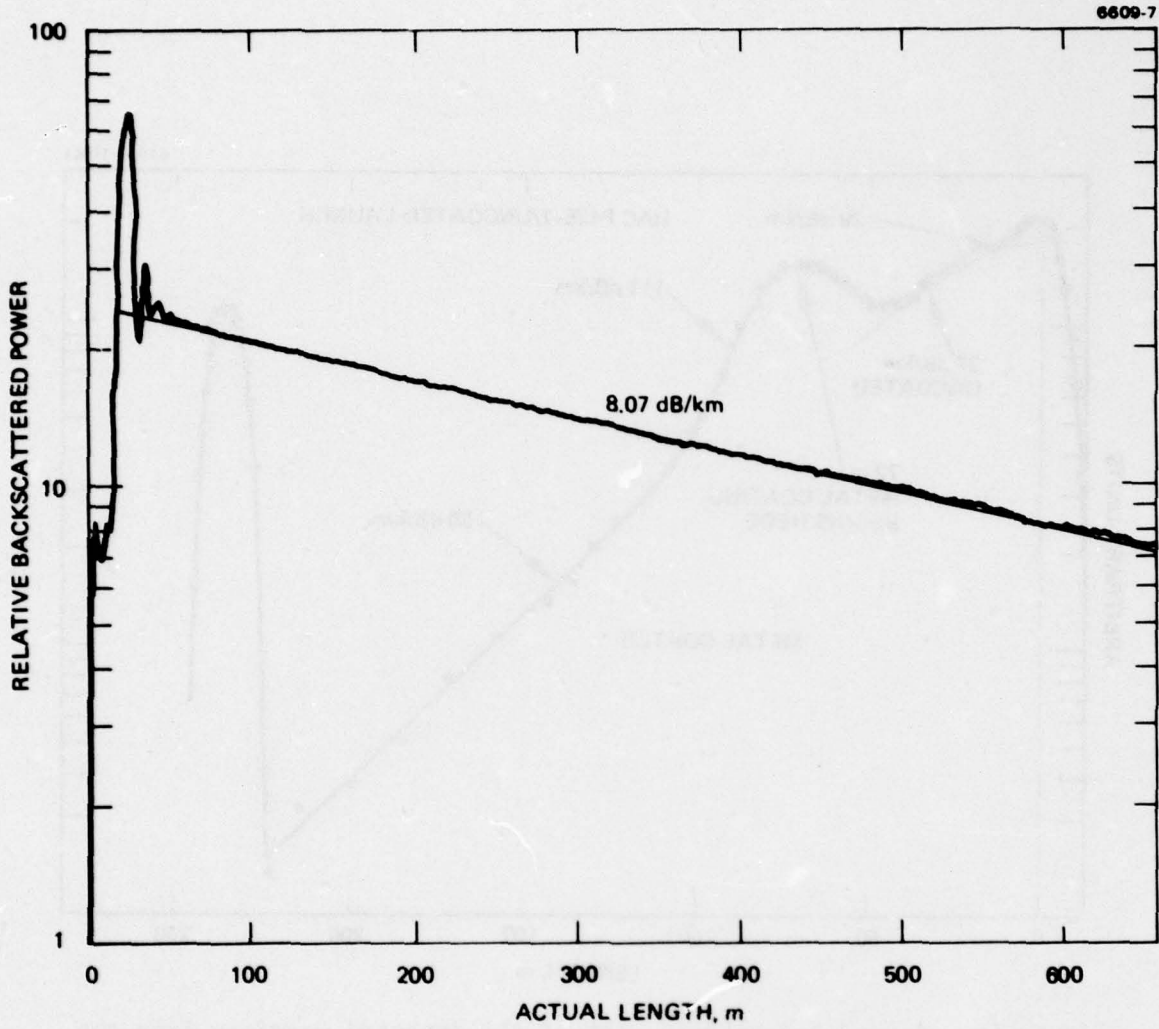


Figure 45. Backscatter data from Corning fiber G-1000 using 10-nsec-wide pulse. The loss as measured is 8.09 dB/km.

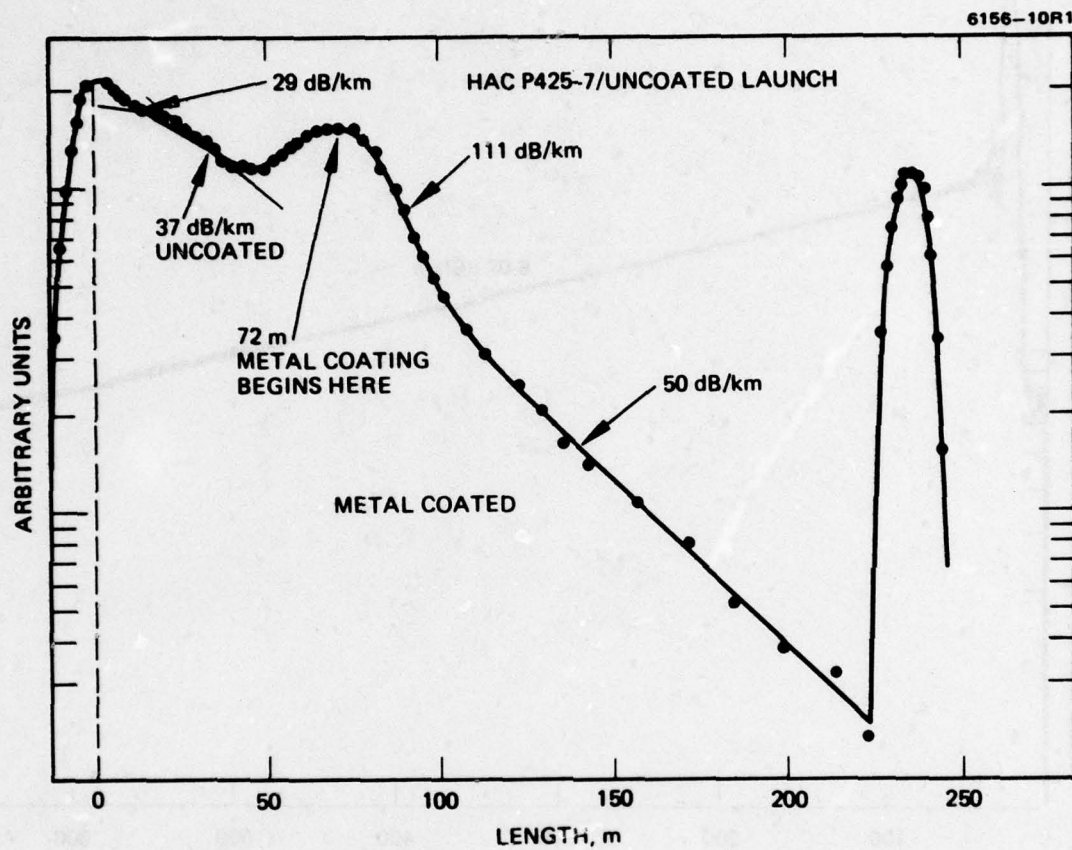


Figure 46. A semi-logarithmic plot of the detected waveform from the center section of HAC fiber (partially metal clad).

- Lossy coating introduction
- Simple dielectric discontinuity (crack or bubble).

Table 3. TDR Results on HAC P425-7

Region	Distance from Uncoated End, m	Loss, dB/km	Comments
1	0-38	39	Uncoated
2	38-84	29	Uncoated
3	84-105	29	Initially broken between 2 and 3 uncoated, Figure 46
4	105-156	37	Uncoated, Figure 46
5	156-192	111	Metal-coated, Figure 46
6	192-324	50	Metal-coated, Figure 46
7	324-409	94	Initially broken between 6 and 7
8	409-434	86	Metal-coated
9	434-539	40	Metal-coated

The detected Rayleigh scattered power is given by Eq. 32. Using this expression, we can attempt to explain the behavior of the center section of the HAC fiber. This section can be divided into four distinct regions, each of different loss characteristics. The first region of 20 m exhibits the lowest loss, 29 dB/km. Since the resolution of this system is 26 m, the loss measured in this first fiber segment is suspect. The second region is 51 m long with a characteristic loss of 37 dB/km. Toward the end of this second region, an apparent increase in the returned signal occurs, bringing us into the third loss region 36 m long exhibiting a very high loss, 111 dB/km. The fourth region is 132 m long and has loss of 50 dB/km. The discontinuity 20 m down the fiber exhibits very little excess loss. It does, however, appear to mix the probe-pulse power distribution into higher order modes, accounting for the higher loss in the second region. Since the taper coupler couples power

into high order modes and leaky modes, we expect a large portion of the power is in leaky modes following the first discontinuity. Since the size of this discontinuity appears to be about the same as the probe pulse length, we expect that this is a bubble or crack.

The apparent increase in signal at the second discontinuity is postulated to be a change in the scattering coefficient, α_s . The location of this discontinuity corresponds with the position where the metal coating begins. We know that these early experimental fibers suffered additional mode mixing caused by microbending. This observation is consistent with the present assumption of a step change in scattering coefficient. In addition, Eq. 32 suggests that the magnitude of the apparent signal gain should be the ratio of the two scattering coefficients. As the probe pulse starts into the discontinuity, the signal amplitude is 115 (arbitrary units) and as it just gets into the third region, the amplitude is 155. The ratio is 1.35. The scattering coefficient α_s (as determined by a least-square exponential curve fit of the data) in region two is $-16.92/\text{km}$ and $-23.12/\text{km}$ in region three. The ratio of these two coefficients is 1.37, in good agreement.

The extremely high loss in region three (111 dB/km) is attributed to the attenuation of leaky and higher order mode power caused by the presence of the metal jacket on the fiber. Additional evidence supporting this statement is found in the measured effective NA in the uncoated and coated sections. Following the coated section the effective NA is reduced significantly (36%) over the effective launch NA.

The effect of small radius bends on the transmission of light in metal-jacketed fiber waveguides was investigated. The experimental arrangement is shown in Figure 47. The fiber used in this experiment was high-strength step-index silica fiber with an Al jacket fabricated at HRL. This fiber was manufactured early in the development of our fiber drawing facilities and is not particularly uniform or low loss. The average loss measured on the OTDR in this particular fiber was 29.4 dB/km . The fiber was further characterized by a $117 \mu\text{m}$ o.d. and a $45 \mu\text{m}$ core diameter. Some discontinuities in the return (Figure 47) are apparent. These discontinuities were probably caused by variations in microbending

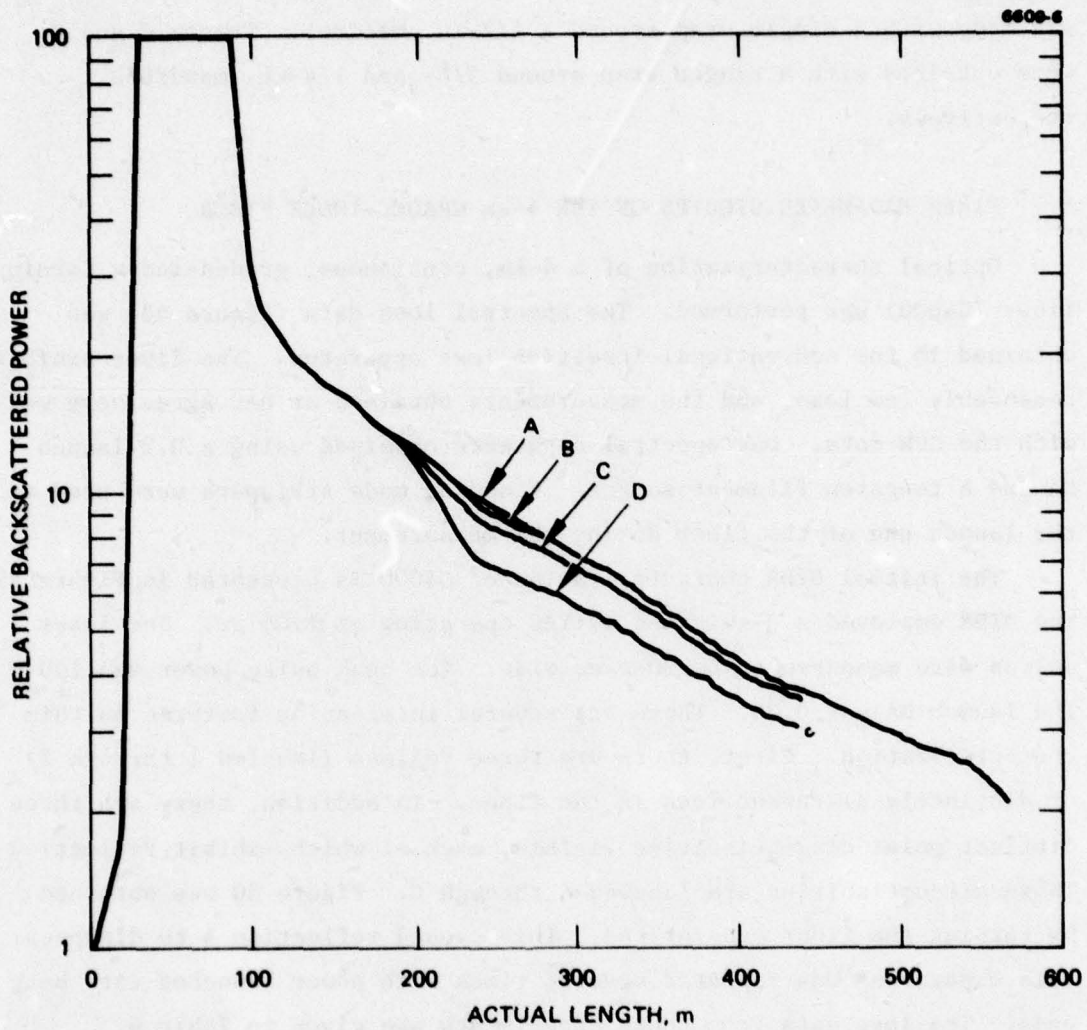


Figure 47. Backscatter data from a HRL developmental fiber showing the effect of wrapping fibers on a mandrel. Trace A is for the straight fiber. Traces B, C, and D are for the fiber wrapped on 1/2, 3/8, and 1/4 in. mandrels, respectively.

loss induced in the fiber as it is coated with metal. Variations in the uniformity of the metal coating are known to cause similar behavior in these fibers. Trace A is the OTDR return with straight fiber. Trace B was made with a single wrap around a 1/2-in. mandrel. Traces C and D were obtained with a single wrap around 3/8- and 1/4-in. mandrels, respectively.

E. FIBER PARAMETER STUDIES ON THE 4-km GRADED-INDEX FIBER

Optical characterization of a 4-km, continuous, graded-index Corning fiber (G4000) was performed. The spectral loss data (Figure 48) was obtained in the conventional insertion loss apparatus. The fiber exhibits reasonably low loss, and the measurements obtained at HAC agree very well with the CGW data. Our spectral data were obtained using a 0.2 launch NA and a tungsten filament source. Cladding mode strippers were used at the launch end of the fiber during the measurement.

The initial OTDR characterization of G4000 is presented in Figure 49. The OTDR employed a Q-switched Nd:YAG operating at 1.06 μm . The laser pulses were measured to be 20-nsec wide. The peak pulse power was 100 W. The launch NA was 0.06. There are several interesting features in this characterization. First, there are three regions (labeled 1 through 3) of distinctly different loss in the fiber. In addition, there are three distinct point discontinuities visible, each of which exhibit reflections. These discontinuities are labeled A through C. Figure 50 was obtained by turning the fiber end-for-end. This caused reflection A to disappear. This experiment was repeated several times with power launched into both ends. The loss data from these experiments are given in Table 4.

One feature seems to be missing from the above data. Olshansky had predicted,¹⁶ and observed experimentally,¹⁷ a steady-state mode-mixing length in graded index fiber. This mode mixing length is characterized theoretically by two different characteristic attenuations, the steady-state value and a different attenuation before the steady-state is achieved. For this fiber, the mode-mixing length is predicted to be just in excess of 1 km. That an approach to the steady-state was not observed may be explained in two different ways. The steady-state

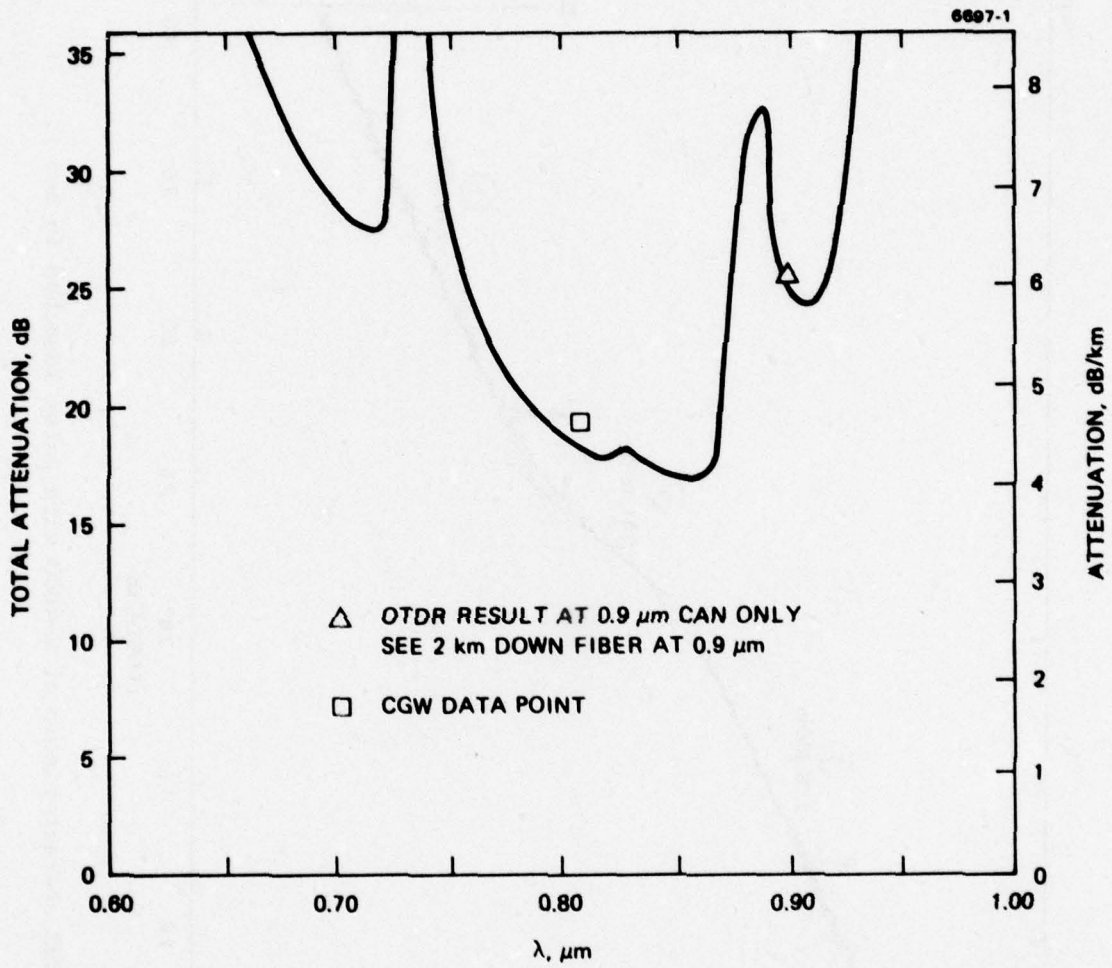


Figure 48. Spectral insertion loss measurement obtained on fiber G-4000.

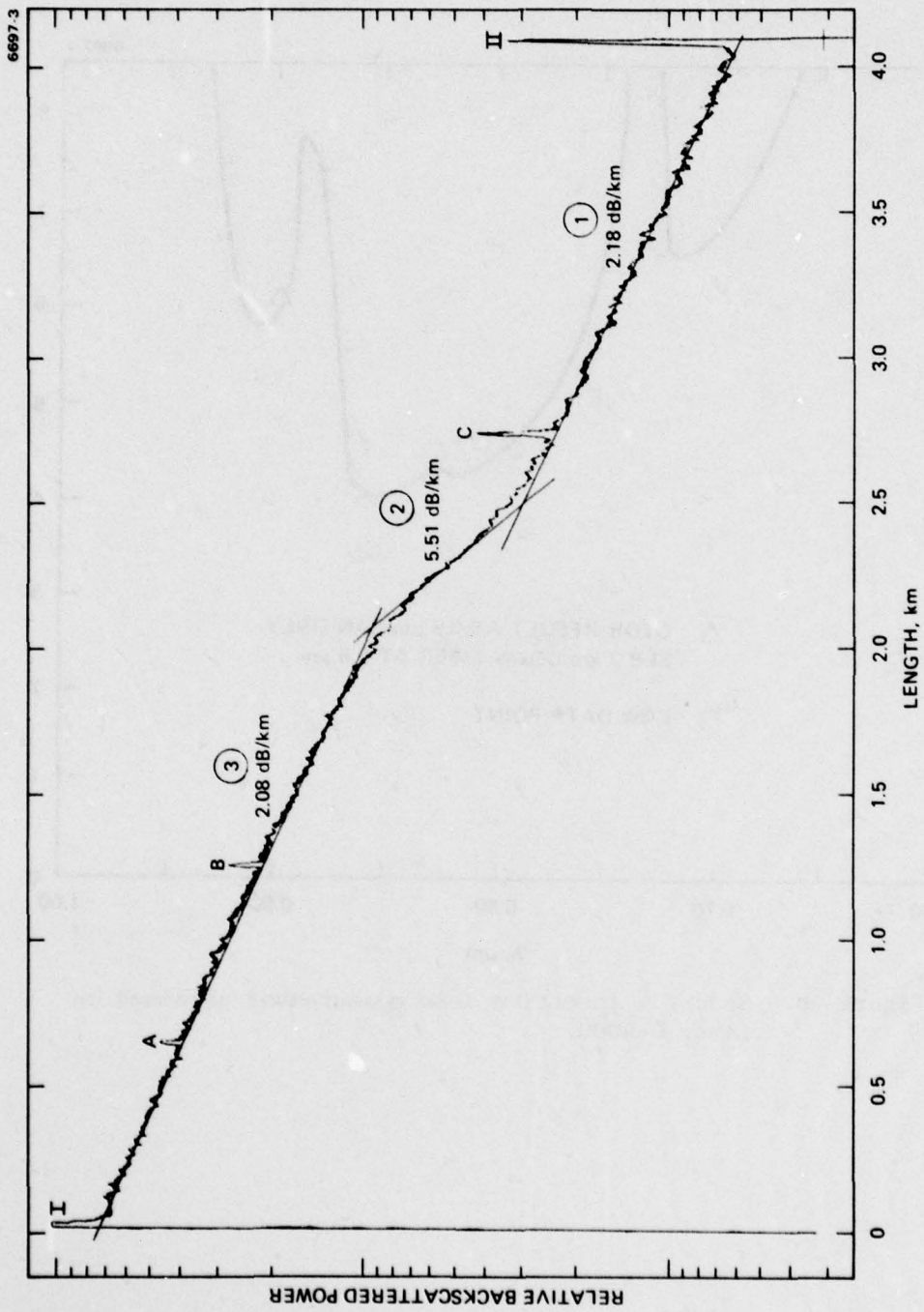


Figure 49. OTDR characteristic of C-4000 with pulse launched in end 1.

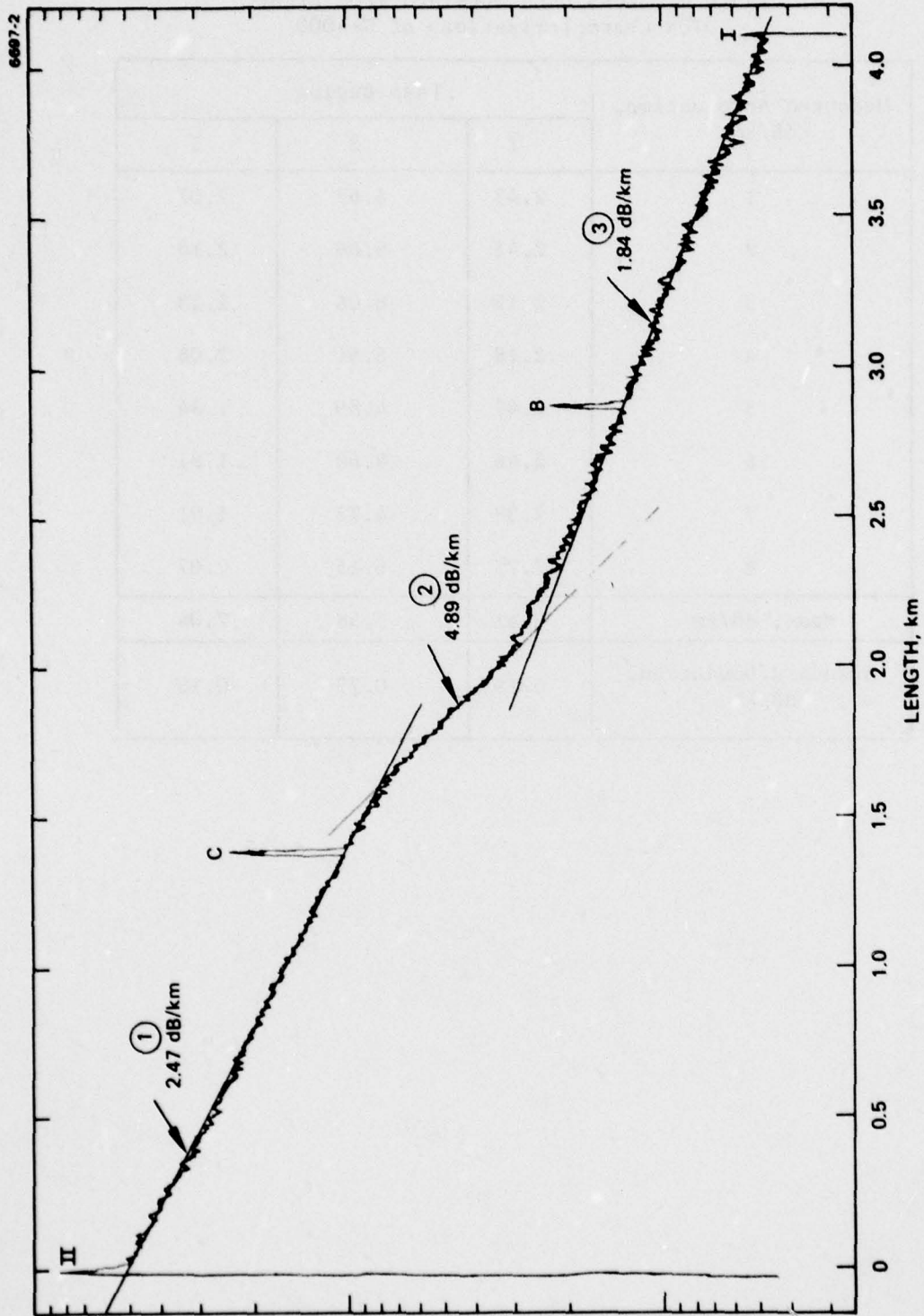


Figure 50. OTDR characteristic of G-4000 with pulse launched in end II. Notice that reflection A is missing.

Table 4. Loss Data Obtained From Eight
OTDR Characterizations of G-4000

Measured Attenuation, dB/km	Loss Region		
	1	2	3
1	2.43	6.67	2.07
2	2.43	6.06	2.18
3	2.15	6.06	2.33
4	2.18	5.51	2.08
5	2.47	4.89	1.84
6	2.46	4.60	1.81
7	2.38	4.73	1.91
8	2.75	6.15	2.07
Mean, dB/km	2.41	5.58	2.04
Standard/Deviation, dB/km	0.19	0.77	0.18

mode-mixing-length may be much shorter than predicted theoretically. If complete mode-mixing occurs within the first 5 m or so, the transition, because of a lack of spatial resolution, would not be observed. A second explanation is that the attenuation of a low NA launched beam and a high NA scattered beam just cancelled. The launch NA of our experiment was a very low 0.06. The backscattered light has an NA which effectively overfills the fiber. The attenuation measured by the OTDR is then the average attenuation of two very different excitations. Each may have its own characteristic mode-mixing behavior, but it is at least possible that they both exhibit the same mode-mixing length. If this occurs, an equal and opposite effect occurs that tends to cancel. In other words, the normal attenuation for the 0.06 NA light ($\alpha_{0.06}$) is less than the steady state (α_s). The attenuation for the overfilled fiber (α_o) is greater than the steady-state and

$$\alpha_{0.06} + \alpha_o = 2 \alpha_s .$$

To test this latter hypothesis, modifications were made to the Nd:YAG OTDR. The pulsewidth was increased to 300 nsec, corresponding to a pulse 60 m long inside the fiber. Two changes were incorporated in the optical system as compared to the previous system. A variable aperture was placed in the system. The aperture permits the NA to be varied easily. A photomultiplier tube (PMT) with S-1 surface was used as the detector instead of the avalanche photodiode (APD) previously used. The PMT eliminates a dc offset problem inherent in the APD, adds more gain, and simplifies electrical interfacing to the boxcar integrator. The first test performed with this OTDR was to check the repeatability of this new system. Figure 51 shows two OTDR characterizations of G-4000 made under identical conditions. The two traces are nearly impossible to separate until the signal level approaches the noise level, about 3.5 km down the fiber. Also, the fiber OTDR characteristic had changed since the initial characterization on this fiber (see Figure 50). There is an additional point defect ≈ 600 m from end II; the origin of this reflection was investigated by unspooling the fiber. The defect was found to be a kink in the fiber caused when one of the many layers of fiber on this spool slipped.

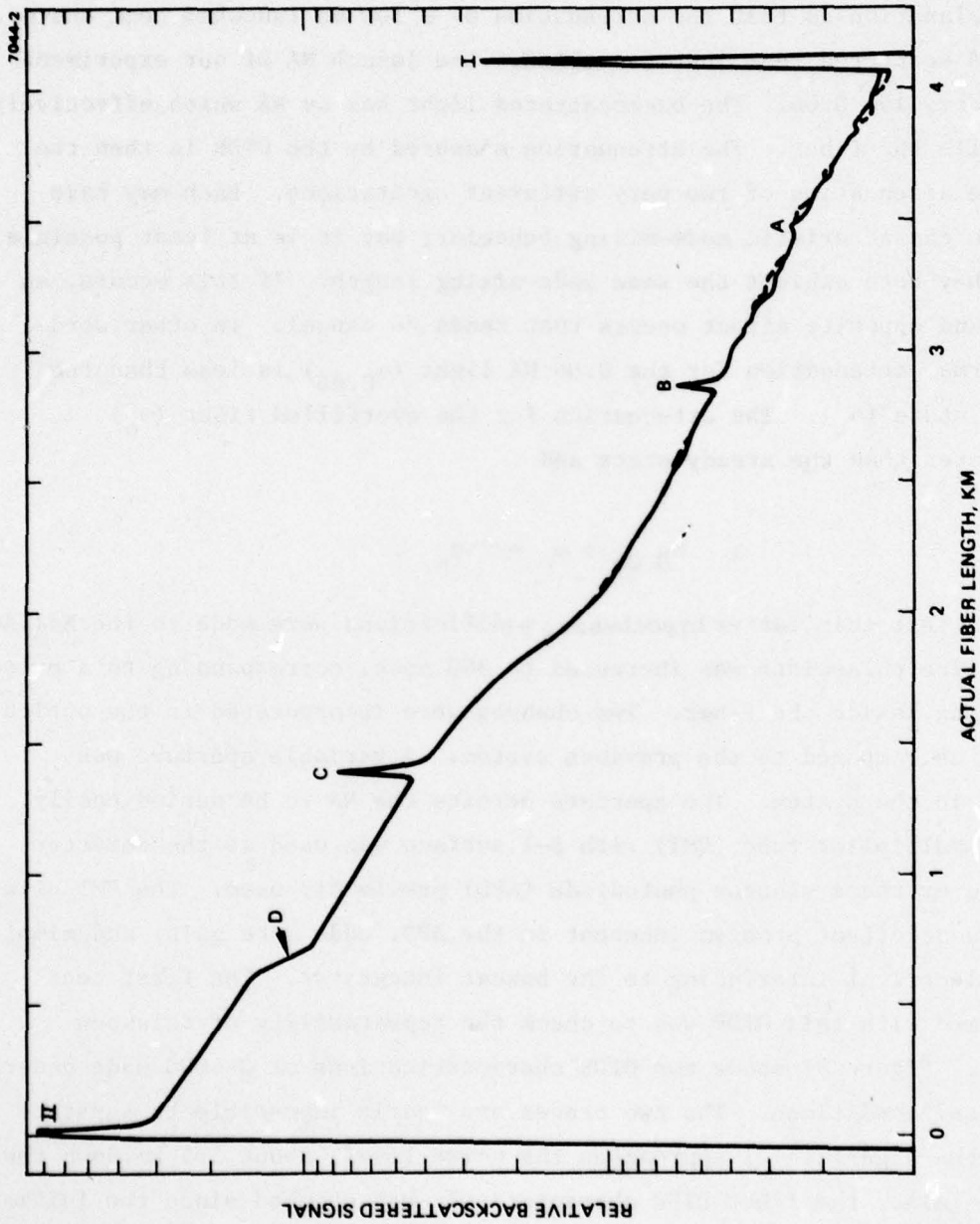


Figure 51. The OTDR characterizations of G-4000 made under identical conditions to ensure repeatability of the new system.

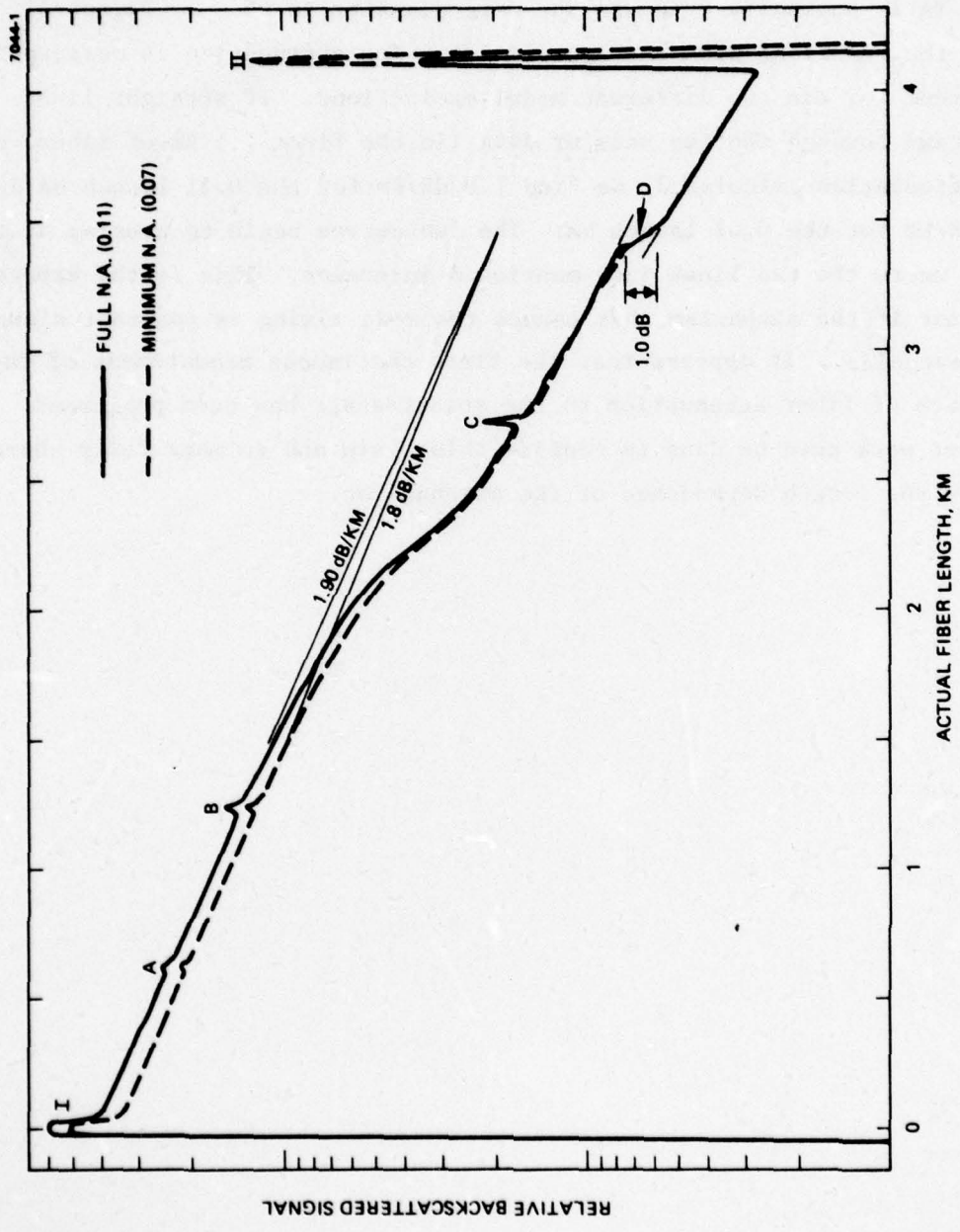


Figure 52. Two OTDR characterizations of G-4000 resulting from different launch NAs show an equal loss after approximately 3.5 km.

Convinced of the repeatability of the new system, additional experiments were performed attempting to see the approach to steady-state loss. The two launch NAs used in this experiment were 0.07 and 0.11, the fiber NA is nominally 0.16 and the core diameter is 65 μm . Figure 51 shows the resulting OTDR characteristics. The attenuation is measurably different for the two different modal excitations. If straight lines are drawn through the two sets of data (in the first 1.5 km of fiber) and the attenuation calculated, we find 1.9 dB/km for the 0.11 launch NA and 1.8 dB/km for the 0.07 launch NA. The two curves begin to overlap at the point where the two lines just mentioned intersect. This is the expected behavior if the mechanism that causes the mode mixing is constant along the waveguide. It appears that the first continuous measurement of the approach of fiber attenuation to the steady-state has been performed. Further work need be done to confirm this claim and to more fully characterize the length dependence of the attenuation.

REFERENCES

1. H.M. Presby, J. Opt. Soc. Am. 64, 200 (1974).
2. J.W.Y. Lit, J. Opt. Soc. Am. 65, 1311 (1975).
3. D. Marcuse, Appl. Opt. 14, 1528 (1975).
4. D. Marcuse, H.M. Presby, Paper PD2-1, Optical Fiber Transmission II, Mtg., Williamsburg, VA, February 1977.
5. B.S. Kawasaki and K.O. Hill, Appl. Opt. 16, 1794 (1977).
6. W.A. Gambling, D.N. Payne, and H. Matsumura, Appl. Opt. 14, 1538 (1975).
7. M.K. Barnoski, Fundamentals of Optical Fiber Communications, Academic Press, Inc. (1976).
8. F.P. Kapron, R.D. Maurer, and M.P. Jeter, Appl. Opt. 11, 1352 (1972).
9. M.K. Barnoski and R.J. Morrison, Appl. Opt. 15, 253 (1976).
10. A. Papp and H. Harms, Appl. Opt. 16, 1315 (1977).
11. F.P. Kapron, N.F. Borelli, and D.B. Keck, J. Quant. Electr. QE-8, 222 (1972).
12. Millman and Taub, Pulse, Digital, and Switching Waveforms, McGraw Hill (1965), pp. 510-572.
13. D. Schiskentanz, Siemens Forsch, -u, Entwickl.-Ber. Bd. 6, 92 (1977).
14. M.K. Barnoski and S.M. Jensen, Appl. Opt. 15, 2112 (1976)
M.K. Barnoski, M.D. Rourke, and S.M. Jensen, Proc. 2nd European Conference on Fiber Communication, Sept. 27-30, 1976, Paris, France.
M.K. Barnoski et al., to be published Appl. Opt. Sept. 1977.
15. S.D. Personick, BSTJ 56, 355 (1977).
16. R. Olshansky, Appl. Opt. 14, 935 (1975).
17. R. Olshansky, M.G. Blankenship, D.B. Keck, "Length Dependent Attenuation Measurements in Graded-Index Fibers," presented at 2nd European Conference on Optical Fiber Communication, Paris, France (1976).